Study of Plasma Behavior Based on Particle and Heat Flux Measurements and Numerical Simulation in the GAMMA 10/PDX End-Cell

ISLAM MD SHAHINUL

February 2018

Study of Plasma Behavior Based on Particle and Heat Flux Measurements and Numerical Simulation in the GAMMA 10/PDX End-Cell

ISLAM MD SHAHINUL

Doctoral Program in Physics

Submitted to the Graduate School of
Pure and Applied Sciences
in Partial Fulfillment of the Requirements
for the Degree of Doctor of Philosophy in
Science

at the
University of Tsukuba

Contents

Chapter 1 Introduction

1.1 Nuclear Fusion

The demand for electricity in the world increases day by day. World energy resources (Coal, Uranium) also reduce drastically because of its intensive use. As a result, generation of energy from the conventional energy sources diminishes day by day. In addition, the population density boosts up with time. Especially, the rate of rising population density is very high in the developing countries. Therefore, it is very much important to consider new sources of energy that can fulfill energy demand in the near future. The solar-cell is one of the possible ways to solve the energy crisis in the world. However, the major drawback of the solar-cell is low power conversion efficiency (PCE). Furthermore, solar cell is suitable only for the warm countries. Thus, nuclear fusion power generation is the best way to solve the above problems. The energy production using fusion reactor is considered as a viable, safe and secured source of energy that could solve the energy crisis across the globe. The advantages of nuclear fusion reactors over the fission reactors are: no dangerous chain reactions, abundant energy, sustainability, no CO_2 emission (mainly helium, hydrogen and inert gas), less radioactive waste, no risk of meltdown, deuterium is available in nature, etc. However, some problems do need to solve to get fusion power in the world.

In the nuclear fusion reactions, two or more atomic nuclei interact and produce one or more different atomic nuclei and subatomic particles (neutrons and/or protons). The nuclear reactions release large amounts of energy due to the difference in mass between the products and the reactants, which comes from the difference in binding energy between the atomic nuclei before and after the reaction. Typical nuclear reactions that produce the huge amount of power are listed in Equations 1.1-1.4. The rate coefficients of these reactions are shown as a function of energy in Fig 1.1.

$$D + D \rightarrow p + T + 4.032\ \text{MeV} \tag{1.1}$$

$$D + D \rightarrow {}^{3}He + n + 3.2\ \text{MeV} \tag{1.2}$$

$$D + T \rightarrow n + {}^{4}He + 17.586\ \text{MeV} \tag{1.3}$$

$$D + {}^{3}He \rightarrow p + {}^{4}He + 18.341\ \text{MeV} \tag{1.4}$$

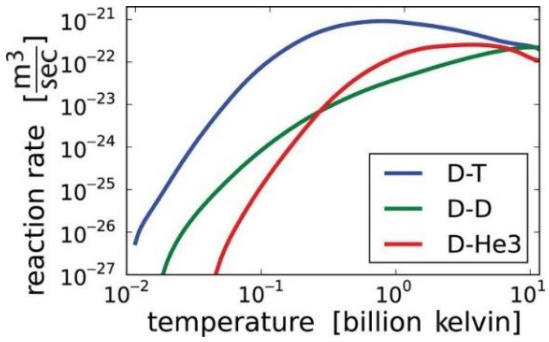

Fig. 1.1 The rate coefficient of nuclear fusion reactions [70].

Where, D and T represent hydrogen isotopes deuterium and tritium, respectively. The neutron and proton are indicated by n and p, respectively.

The D-D and D-D reactions release energy. However, the D-^{3}He reaction has advantages for releasing the largest amount of energy. In addition, this reaction does not produce any neutron. However, the drawback of this reaction is low reaction rate. The D-T reaction also releases the huge amount of energy. In addition, the D-T reaction rate coefficient is very high compared to D-D and D-^{3}He as shown in Fig. 1.1. Therefore, D-T reaction has been chosen as the most promising candidate for the first-generation nuclear fusion reactors. The D is commonly available in the nature. However, T is not a commonly available hydrogen isotope in nature because it has a short half-life, it is difficult to find, store and produce. It is also an important task to handle radioisotope tritium. Tritium may leak from the fusion reactors which releases radioactivity in the environment. Tritium can be extracted from the Li reaction. The method of extracting Li from the sea has been developed [1-3], which solves the crisis of tritium for the nuclear fusion reactors.

The final goal of fusion community is to construct an artificial sun in the earth. In the sun, nuclear fusion reactions are controlled and confined by the strong gravitation force. The enormous size of the sun is also an important factor for the sustainment of nuclear fusion reactions. In the earth, nuclear fusion reactions are planned to be controlled and confined by the magnetic field. However, many problems need to be solved to get a nuclear fusion reactor in the earth. Control of the enormous heat load in a limited chamber is one of the main obstacles for the development of future nuclear fusion reactors.

Fusion community is going to build the nuclear fusion device the “ITER” in France. The ITER (International Thermonuclear Experimental Reactor) organization is planning to produce first plasma in 2025. Figure 1.2 shows the schematic view of the world’s largest project ITER.

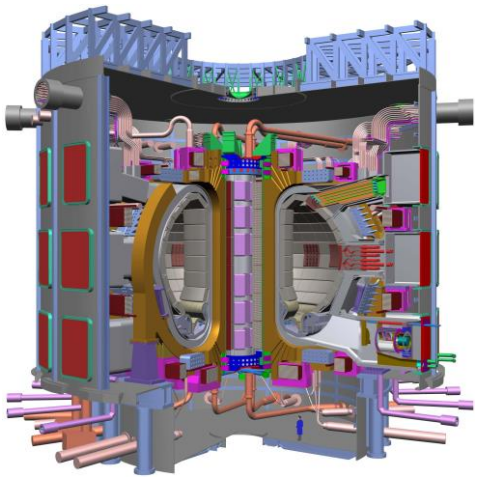

Fig 1.2　The schematic of the nuclear fusion reactor ITER [83].

The energy balance equation for fusion plasma is written as follow,

$$\frac{d}{dt}(3n_iT) = P_\alpha + P_H - P_L = \frac{n_i^2}{4} < \sigma v > E_\alpha + P_H - \frac{3n_iT}{\tau_E}, \quad (1.5)$$

where,

$3n_iT$: The sum of electron and ion thermal energy per unit volume.

P_α : Alpha particle heating power.

P_H : Input plasma heating power

P_L : Energy loss power from plasma.

In the steady state operation, equation (1.5) can be written as follow,

$$n_i\tau_E = \frac{3n_i^2T}{P_\alpha + P_H} = \frac{12T}{< \sigma v > E_\alpha(\frac{1+A}{Q})}. \quad (1.6)$$

The following notations are used:

Q is the fusion energy gain factor. Q is the ratio of the generated power to the input heating power, usually expressed with Q = P_F / P_H. P_F represents generated power in a reactor and P_H represents the power required to maintain the plasma in steady state.

A : The ratio of alpha particle heating power to all power output by nuclear fusion reaction. "A" is defined as A = P_F / P_α.

The condition of " Q = 1 " is referred to as critical plasma condition or breakeven condition while the condition of Q = ∞ is referred to as self-ignition condition. Nuclear fusion reactor runs and sustains without any external heating when the self-ignition condition is achieved. In the nuclear fusion research, the Lawson criterion [4] is a very much important general measure of a fusion device or reactor that defines the conditions to be needed to reach ignition, which implies that, the heating of the plasma by the fusion reactions (such as D-T, D-D, D-^{3}He) is enough to sustain the plasma energy against all power losses without any external heating power. The Lawson criterion provides a minimum standard value for the product of the electron density (n_e), electron temperature (T_e) and the energy confinement time (τ_e). The Lawson diagram is shown in Fig. 1.3.

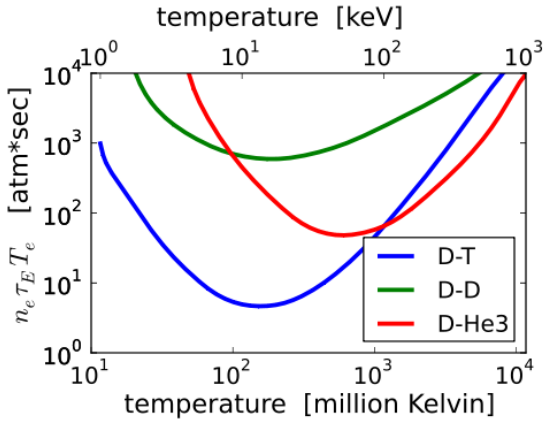

Fig. 1.3 The fusion triple product condition for D-T, D-D and D-^{3}He fusion reactions. [70]

1.2 Divertor studies

Figure 1.4 shows the poloidal cross-sectional view of the tokamak device. In the magnetic confinement fusion reactor such as tokamak, high temperature and density plasma are confined in the core region. Plasma diffuses and strikes the wall. The distance from the core hot plasma to the vessel wall is about few meters. Most of the temperature drop occurs over the last few centimeters, which means that, in this region the temperature may decrease by several tens of million degrees per centimeter. This region is called the plasma edge as shown in Fig 1.4. Plasma wall interactions is a complex system. The impurities are generated due to the plasma-wall interactions may transport into the core plasma and contaminate it and consequently, the core plasma quality degrades by interactions between core plasma and impurities. This processes strongly affect the nuclear fusion reactions. Therefore, the divertor concept has been developed in order to suppress the direct plasma-wall interaction and to reduce the transportation of impurities into the core plasma [5-6]. The divertor magnetic configuration has a separatrix, which separates magnetic field into two different regions. One is closed magnetic surface in the core region while the other is opened magnetic surface at the edge region. In the tokamak devices, Scrape-Off Layer (SOL) separates the magnetic field lines from the closed flux surface region by the last closed flux surface (LCFS). The SOL is the most widely used fusion facilities to confine hot plasmas in the tokamak devices. In the SOL region, the heat flows through the devices are separated (scraped off) from the plasma edge and then the heat flux enters into the region which is called divertor. In the divertor region, the two target plates are installed (W has been considered so far). The divertor magnetic field configuration significantly improves the plasma confinement in the core. However, the reduction of the high heat-flux onto the target plates of the divertor plates is one of the most important challenging issues to protect the divertor plates. The high heat-flux enters into the divertor region and strikes on the target plates of divertor. The heat-load on the target plates of divertor in the ITER discharge is estimated to be 5-20 MW/m^2 in steady state whereas it is more at the transition phase [7-8]. Erosion and sputtering are produced on the target plate due to the high heat-load. Tungsten (W) has been considered as a power handling material for the divertor plate in the future fusion devices so far [9]. However, the plasma-material interactions at such the power range significantly diminish the life time of the tungsten material [7]. Thus, it is necessary to minimize the power load on the divertor target plates. The following crucial tasks need to be solved for the future divertor:

(1) The reduction of the high upstream heat flux.
(2) Exhaust the helium gas.
(3) The elimination of impurities in the plasma core region (generated at the plasma boundary due to the interactions, or intentionally added to increase radiation loss).

The detached plasma formation in the divertor region has been considered as one of the most

efficient solutions for the removal of high heat flux on the divertor target plates and consequently, it is necessary to reveal the physical mechanism of divertor plasma physics. The physical mechanism related to the divertor plasma is extensively studied experimentally and numerically in order to reveal detailed divertor physics related to the plasma detachment, impurity transport. Therefore, evaluation of a plasma cooling process and generation of a detached plasma in the divertor region is necessary. The plasma detachment state can be obtained via the following processes: Plasma loses the energy during interactions with neutral particles (impurity and hydrogen) such as; ionization, excitation, charge-exchange (CX), radiation cooling. The schematic drawing of the plasmas and neutral characteristics in the cases of detached and attached plasma is shown in Fig. 1.5. Figure 1.6 shows the physical mechanism of plasma detachment. Radiator gas injection into the divertor region (such as Ne, Ar, Kr, Xe) significantly reduces the plasma energy on the target plate [10-21] by enhancing the radiation power loss. Radiator gas injection in the divertor region significantly enhances the radiation losses [10]. In addition, the hydrogen atomic and molecular processes also play a very important role to generate the detached plasma [53]. Recycling hydrogen neutrals also play a role to decrease the plasma ion energy. The recycling neutrals are re-ionized by the plasma and then transport again toward the divertor region. Hydrogen molecules are recycled on the divertor target plate and then interact with the plasmas and consequently vibrationally excited, which significantly increase the MAR (Molecular activated recombination) processes. Furthermore, neutral hydrogen seeding into the divertor region may also enhance the momentum loss by enhancing the CX loss. Moreover, the volume recombination processes (Molecular Activated Recombination (MAR) [23-24] and Electron-Ion Recombination (EIR) [25]) may also further decrease the heat load on the target plate at the low temperature plasma. The MAR and EIR reactions rate coefficient are increased as T_e is reduced [22].

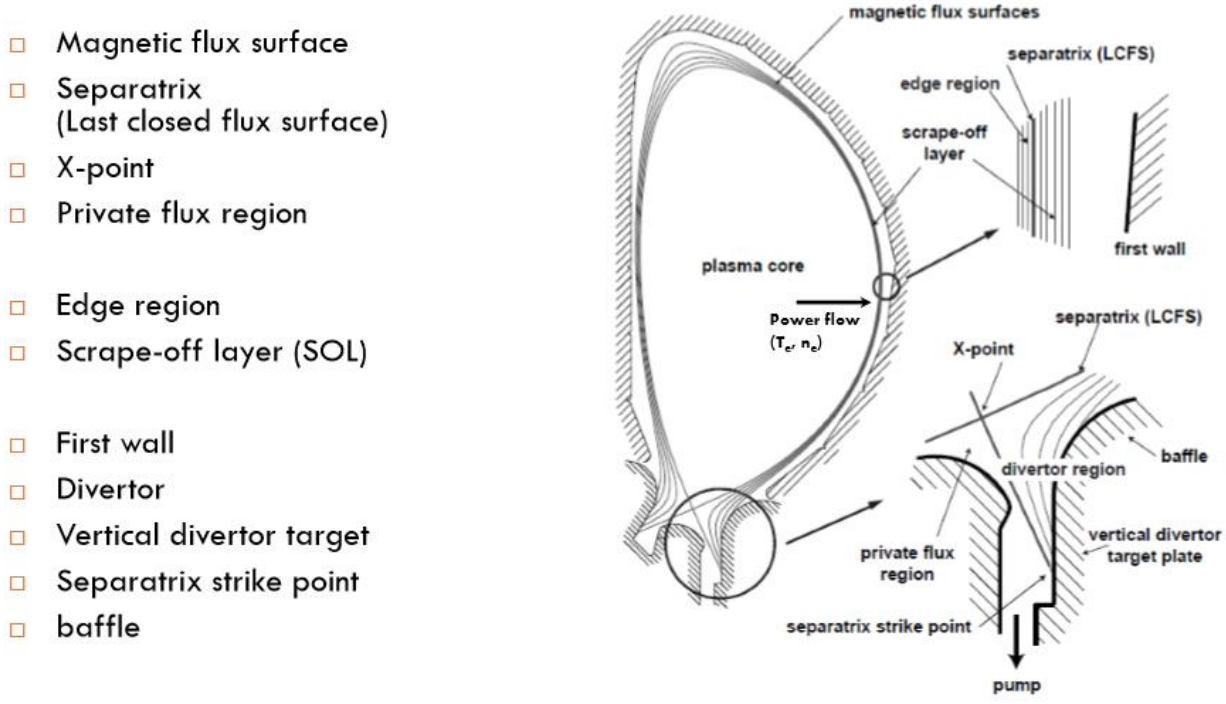

Fig. 1.4 Poloidal cross-section of the tokamak device [82].

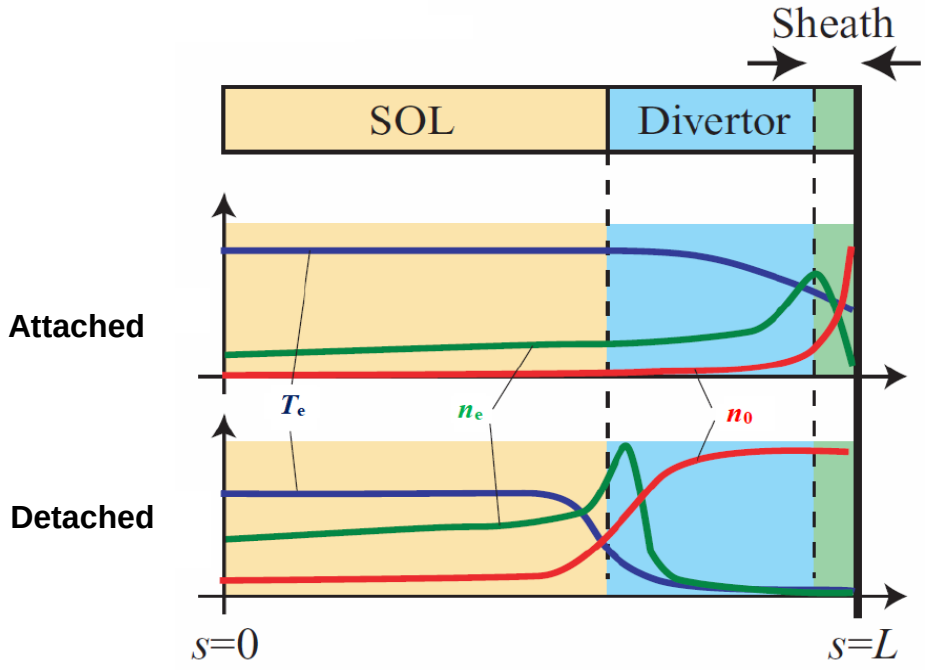

Fig. 1.5 Schematic drawing of the plasma and neutral characteristics in the attached and detached state [91] (where, T_e: electron temperature, n_e: electron density, n_0: neutral particle density, s = 0: stagnation point, s = L: divertor plates).

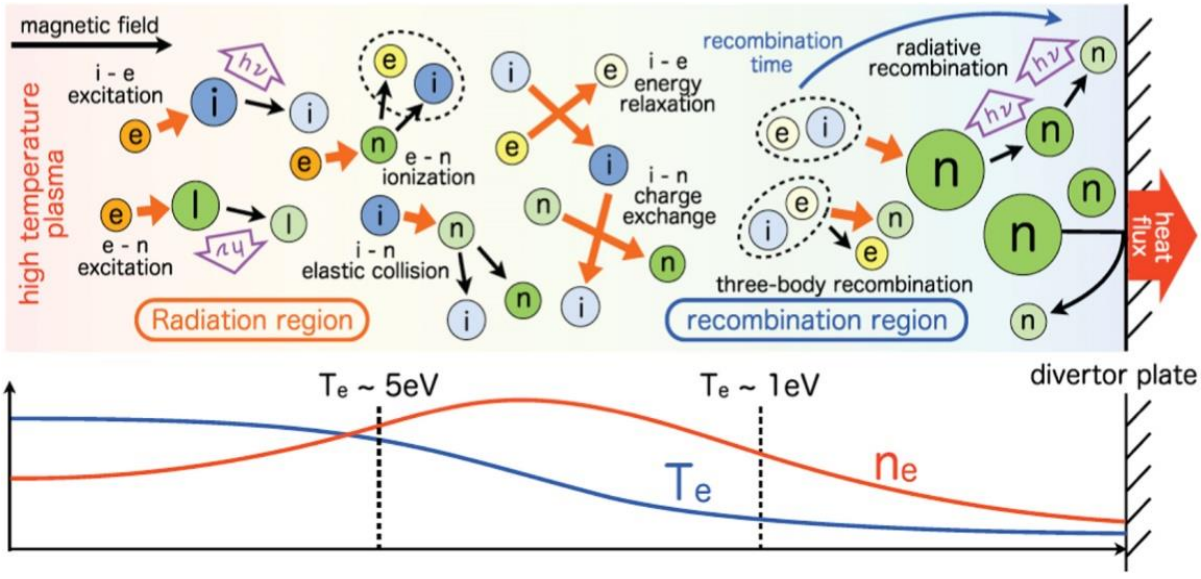

Fig. 1.6 Schematic drawing of the physical mechanism of plasma detachment [63].

1.2.1 Experimental study in the divertor

The divertor simulation study has been extensive performed in the world by using the Linear and Tokamak plasma confinement devices. The Tokamak geometry has been adopted by the ITER

organization. The tokamak geometry is much more complex than that of the linear devices. However, the magnetic field in the divertor region of the tokamak device is open. Therefore, a simple configuration of the open magnetic field devices may effectively simulate the detailed physical mechanism related to the divertor physics such as radiation cooling, plasma detachment, impurity transport, recombination processes, etc. The divertor research has been done by using many tokamak devices such as JET [10], JT 60 U [20], ASDEX Upgrade [17], DIII-D [21], C-Mod [15], etc. On the other hand, divertor simulation research has also effectively conducted by using the linear plasma confinement devices such as Pilot-PSI [26], Magnum-PSI [27], NAGDIS-II [22], GAMMA 10/PDX [28]. In the JET, nitrogen seeding shows a promising result on the reduction of ion flux [59]. The impurity injection experiments have also been done in the JT 60 U. In the JT 60 U experiment, with Ne seeding the detached plasma has been generated [60]. ASDEX-Upgrade experiment results also show a plasma detachment state with combined Kr and N_2 seeding [61]. The plasma detachment state has also observed by gas puffing in the tokamak device DIII-D and C-Mod [15]. The linear plasma devices NAGDIS-II and Pilot-PSI also show a clear plasma detachment regime by puffing hydrogen neutral particles [62-63]. Figures 1.7-1.10 show the plasma detachment by seeding neutral gas into the divertor region.

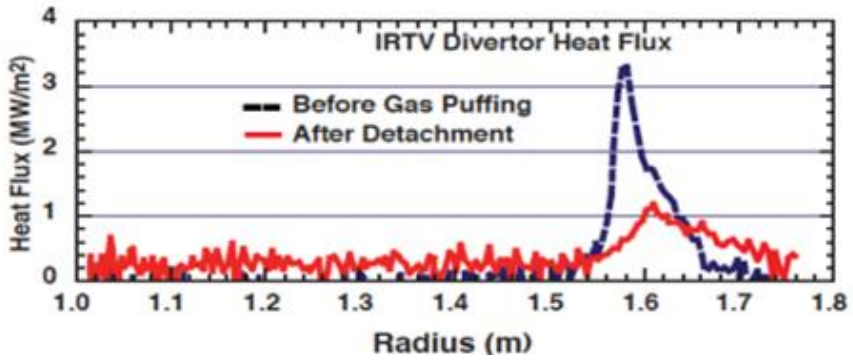

Fig. 1.7 Divertor power loading in DIII-D tokamak in attached and detached regimes [12].

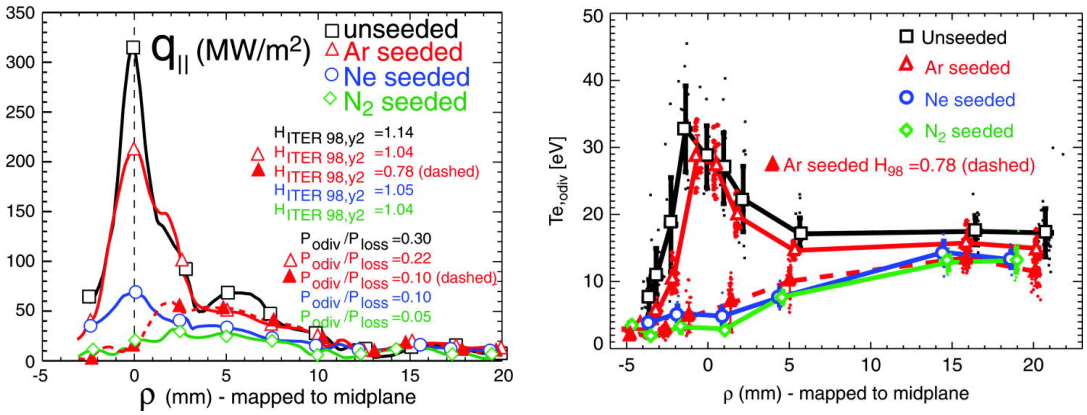

Fig. 1.8 Reduction in heat flux and electron temperature in Alcator C-Mod by impurity seeding [90].

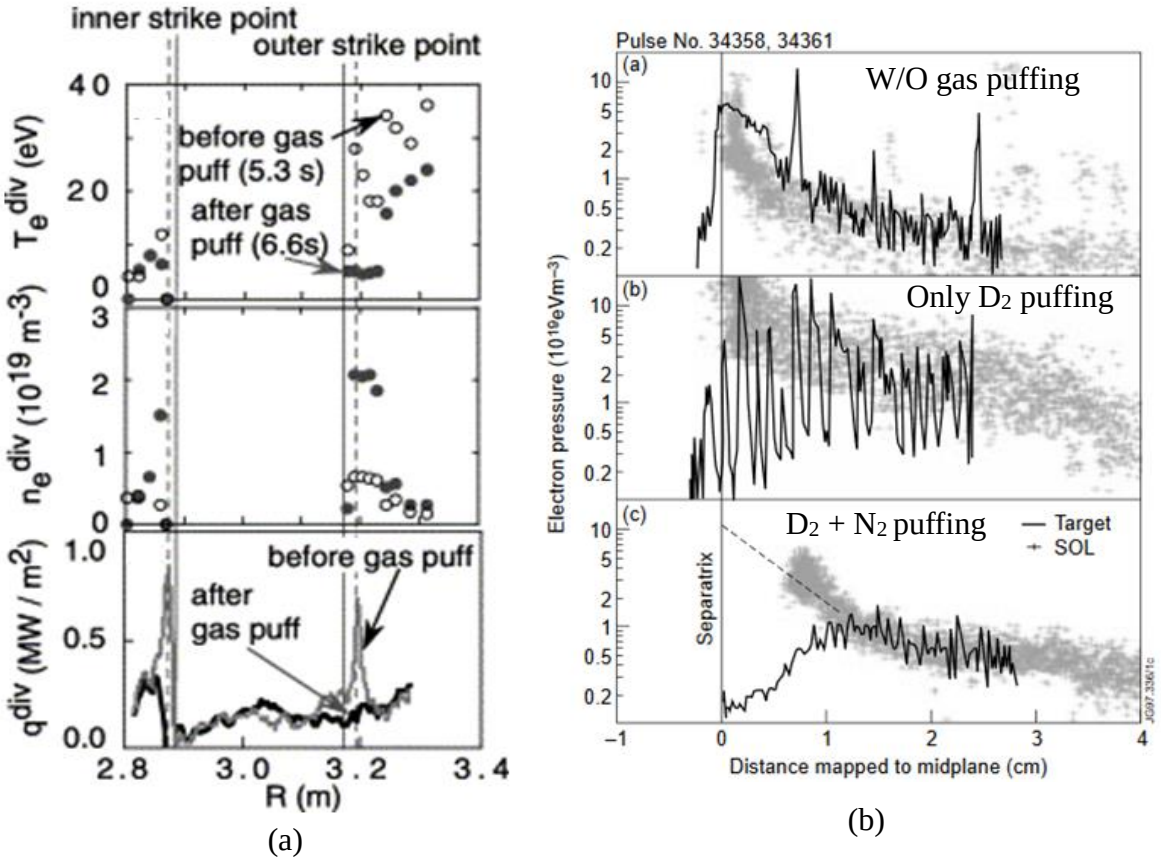

Fig. 1.9 Plasma detachment in (a) the JT-60 U by Ne seeding [60] (b) the JET by N_2 and D_2 seeding [59].

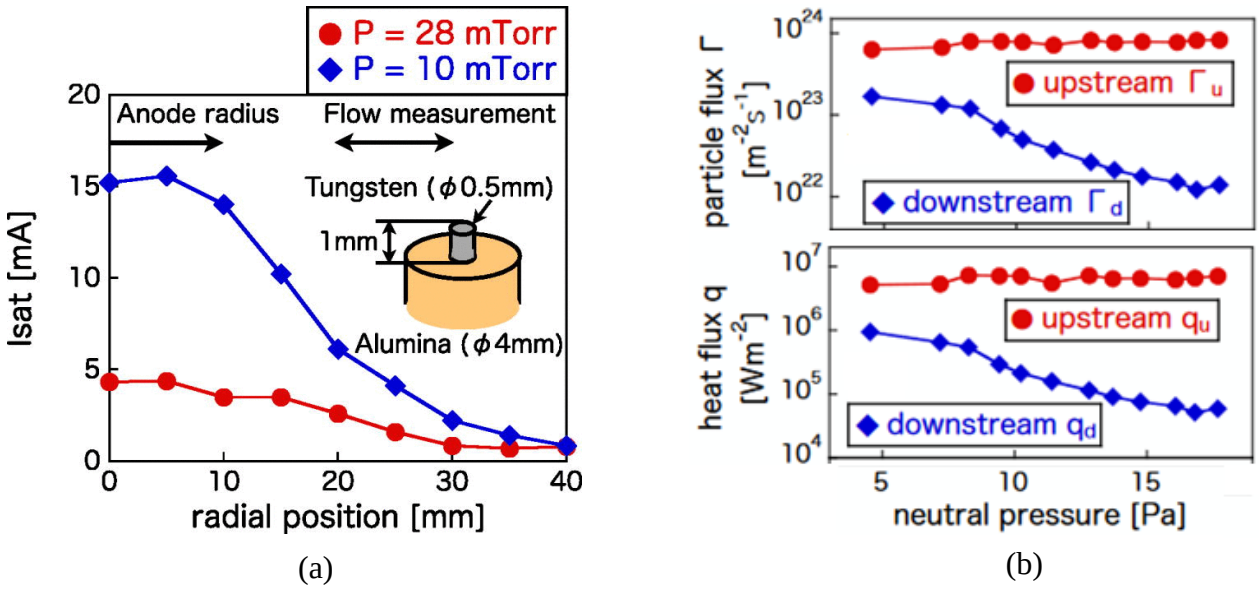

Fig. 1.10 Plasma detachment in (a) the NAGDiS-II [62] (b) the Pilot-PSI [63].

1.2.2 GAMMA 10/PDX for the divertor simulation study

Linear plasma fusion devices may contribute significantly to explore the physical mechanism of plasma detachment, since the tokamak geometry is too much complex than that of linear devices. The divertor simulation research has been performed in the few linear fusion devices, however, the ion temperature most of the devices is much lower than that of the SOL plasmas as shown in Fig. 1.11.

The GAMMA 10/PDX ("GAMMA 10" and "Potential-control and Divertor-simulation eXperiments") tandem mirror is the world's largest linear plasma confinement device. The GAMMA 10/PDX tandem mirror device consists of a central-cell, anchor-cells, plug/barrier-cells and end-cells. The open magnetic system plasma confinement device has several advantages over the closed magnetic plasma confinement devices such as plasma controllability, convenience of experimental measurements due to the simple geometry for studying the physical mechanism of divertor plasma physics. Therefore, linear machine GAMMA 10/PDX can be utilized to address tokamak physics such as physical mechanism of plasma detachment, plasma surface interaction (PSI) and plasma transport in the SOL (Scrape-Off-Layer) or divertor region. The typical ICRF heated and gas puffing plasma parameters in the central-cell of GAMMA 10/PDX are $n_e \sim 10^{18} m^{-3}, T_e \sim 50 eV, T_{i\parallel} \sim 200 - 400$ eV, $T_{i\perp} \sim 10$ keV. The unique features of GAMMA 10/PDX for the divertor simulation studies are (1) high ion energy, (2) high magnetic field (3) robust plasma heating system (4) simple geometry to install plasma diagnostics tools. Furthermore, GAMMA 10/PDX team is going to develop a high power ECH system in order to produce several MW level heat flux plasmas. The schematic view of the ion energy versus ion flux is plotted in Fig. 1.11. The ion energy of GAMAA 10/PDX is comparable to the SOL parameters of the ITER. Therefore, GAMMA 10/PDX may explore detailed physical mechanism related to the divertor physics such as plasma detachment, impurity transport, and radiation cooling.

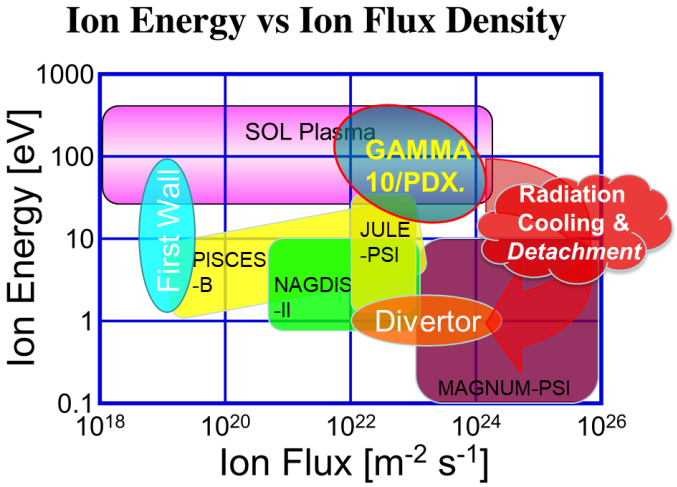

Fig. 1.11 The ion energy versus ion flux for the many plasma devices [28].

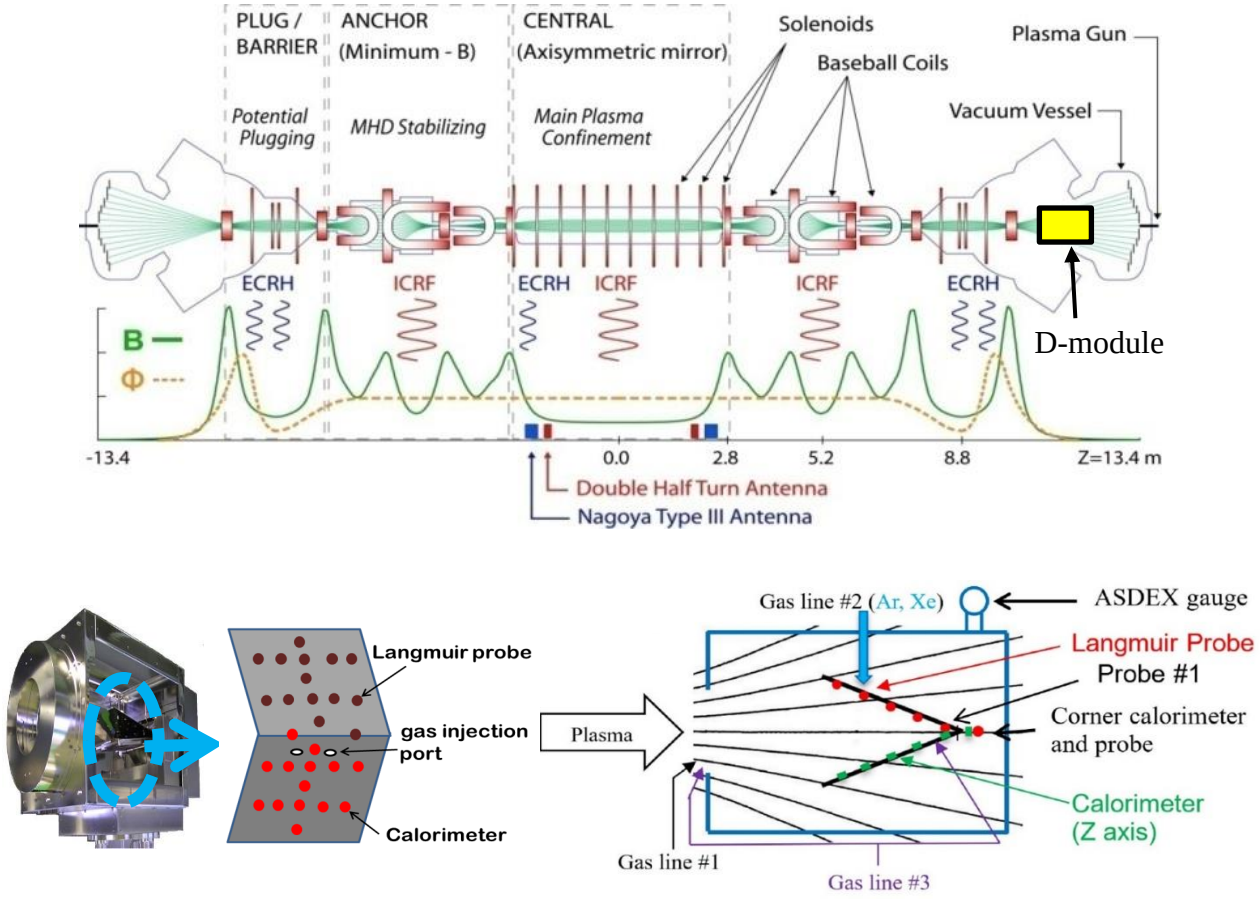

Fig. 1.12 Schematic view of the GAMMA 10/PDX and D-module.

1.2.3 Numerical simulation in the divertor

The simulation study in the divertor region is very important for the following reasons:

(1) To explore the physical mechanism of radiator gases injection into the divertor region.

(2) To study impurity transport toward the core region.

(3) To understand the detailed physical mechanism related to the divertor and SOL physics.

The numerical simulation code such as B2 [35], B2.5 [41], UEDGE [42], SONIC [43], SOLPS [44], EMC3 [45], COREDIV [46], EDGE2D [47] have been developed for simulating divertor plasma physics. These codes have already used to simulate many tokamak devices and play a driving role to understand the physics of plasma detachment, impurity transport, and radiation cooling. The LINDA code [39-40] has been developed for the linear divertor simulator. The plasma transport in the plasma edge region is defined by a set of fluid equations. The source terms of the fluid equations represent the atomic and molecular interactions among plasma and neutral (hydrogen, Impurities). The neutral models can be defined either by a fluid equation or by solving Boltzmann equation such as DEGAS [49], EIRENE [48], NEUT2D [50]. The fluid neutral model is computationally faster but less accurate compared to the Monte-Carlo code. However, the Monte-Carlo neutral model introduces statistical

noise in the calculation. The fluid neutral model may works well for the simple geometry linear fusion device GAMMA 10/PDX.

The divertor plasma physics has been studied by using the above numerical codes. With the SONIC code, a comparison among Ar, Kr and Ne shows that Kr seeding significantly reduces the ion temperature, electron temperature on the target plate [64]. The SONIC simulation for the DEMO has shown that the partial detachment has been achieved by the Ar, Kr impurity seeding [64]. The numerical simulation for the ITER by using the SOLPS4.3 code package also shows a plasma detachment due to Ne seeding [65]. The Ar and Ne seeding simulation study has also been performed for the ITER and the TPX by the B2.5 code [71].

1.3 Motivation and nobility of the study

The divertor simulation research has been done in the many tokamak and linear devices [10-22, 59-60, 90]. These devices have been performed experiments by seeding a few neutral species into the divertor region. However, the effects of impurity species on the plasma detachment have not yet clarified since the fusion devices have shown plasma detachment results for only a few species so far. A comparison of the neutral gas injection into the divertor region of the fusion devices is shown in Table 1.1. The radiation cooling rate of the radiator gases is different. Therefore, it is very much important to explore the detailed comparison of the radiator gases for the formation of detached plasma. The main motivation of the study is to make a detailed comparison of the radiator gases in order to clarify the radiation cooling effect of the gas by using the best use of simple configuration linear fusion device GAMMA 10/PDX. The effects of Ar, Kr and Xe injection into the divertor region of GAMMA 10/PDX have been done in the study. Impurity injection experiments have been done in order to understand the radiation cooling effect of the impurity particles on the plasma detachment and make an extrapolatable database for the future fusion devices.

Table 1.1 A rough survey for the neutral gas injection experiment into the divertor region [10-21, 59-63, 90].

Name of the fusion device	Neutral gas species injection into the divertor region						
	D_2	H_2	N_2	Ne	Ar	Kr	Xe
JET	○	×	○	○	○	×	×
JT-60 U	×	○	○	○	○	×	×
DIII-D	○	×	×	○	○	×	×
C-Mod	○	×	○	○	○	×	×
ASDEX-U	×	×	○	○	○	○	×
NAGDiS-II	○	○	×	×	×	×	×
Pilot-PSI	○	○	×	×	×	×	×
GAMMA 10	×	○	○	○	○	○	○

The behavior of detached plasma during transient heat-flux has not yet clarified in the fusion devices. However, it is a very much important research subject to understand the physical mechanism of detached plasma during high heat-flux (ELM in the case of tokamak). This study is also motivated to reveal the behavior of the detached plasma during high heat-flux condition. The behavior of the detached plasma during the heat-flux case has been studied in the study.

The numerical simulation study in the divertor region has been performed in order to understand the physics of plasma detachment. A numerical study by using a multi-fluid code has also been started in GAMMA 10/PDX to understand the energy loss processes in the divertor simulation research of GAMMA 10/PDX. In the study, the physical model of the numerical code has been improved to understand the energy loss processes during radiator gases seeding. The following numerical code improvement has been done in the study:

1. Neutral models have been improved in the study. The neutral models for both the hydrogen and impurity (Ne, Ar, Kr and Xe) have been solved iteratively together with the fluid equation in the self-consistence manner.
2. Impurity neutral database has been improved in the study. The radiation cooling effect, ionization and radiative recombination of the impurity neutral species (N, Ne, Kr, Xe) have been included in the code.
3. Development of a kinetic neutral code. In the study, a kinetic neutral code has been developed in order to study the transport of hydrogen molecules and atoms precisely. The transport of hydrogen molecules and atoms has been studied in the study.

1.4 Purpose and Outline of the thesis

The purpose of the thesis is to understand the effects of radiator gases (Ar, Kr and Xe) seeding on the plasma parameters toward the plasma detachment in the end-cell of GAMMA 10/PDX based on the experimental and numerical simulation study.

In the paper, chapter 2 describes the experimental setup for the divertor simulation experiment of GAMMA 10/PDX. Experimental results with the discussion is presented in chapter 3. The numerical simulation study by using the multi-fluid code LINDA is given in chapter 4. Chapter 5 gives a brief description of the hydrogen neutral transport by using the kinetic code. A summary of the experimental and numerical simulation outcomes together with the future plans is given in chapter 6.

Chapter 2 Experimental Apparatus

The GAMMA 10/PDX tandem mirror device is the world's largest linear plasma confinement device which is 27 m in length and consists of multiple-cells. The central-cell of GAMMA 10/PDX is the main plasma confinement and heating region. The GAMMA 10/PDX is designed with many plasma heating devices, such as Electron Cyclotron Heating (ECH), Ion Cyclotron Range of Frequency (ICRF), and Neutral Beam Injection (NBI) system [72-76]. The loss-cone region plasmas escape from the central-cell and then transport towards the end-cells. Study of the end-loss flux of the GAMMA 10/PDX is one of the important research subjects for studying plasma-divertor interaction simulation experiments [29-31]. The typical ICRF heated plasmas in the central-cell are $n_{\mathrm{e}} \sim 4 \times 10^{18}\ \mathrm{m}^{-3}, T_{i\parallel} \sim 400\ \mathrm{eV}, T_{\mathrm{i}\perp} \sim 10\ \mathrm{keV}, T_e \sim 50\ \mathrm{eV}$. The unique features of the GAMMA 10/PDX among the all linear devices are high ions temperature. However, plasma density is slightly lower than that of the others linear devices. The GAMMA 10/PDX team is trying to produce high-density plasma in the central-cell. The detailed comparison of the GAMMA 10/PDX among the other linear devices can be found in the reference [22]. Therefore, simple configuration GAMMA 10/PDX could address the detailed physical mechanism of plasma detachment. Because of this, the divertor simulation experiments are conducted by installing a module (D-module) in the west end-region of GAMMA 10/PDX [28, 32-34].

In this chapter, section 2.1 describes the experimental setup of GAMMA 10/PDX. Experimental setup for the D-module is given in section 2.2.

2.1 GAMMA 10/PDX

The schematic view of the GAMMA 10/PDX is shown in Fig. 2.1. GAMMA 10/PDX consists of multiple-cells to confine the plasma. Initial hydrogen plasma is injected by the plasma guns which are located both ends of the GAMMA 10/PDX [72]. In the central-cell, the main plasma is confined and heated by the gas puffing and ICRF heating and which has a mirror ratio of 5 ($B_{\max} \sim$ 2 Tesla at the mirror throat region while $B_0 \sim$ 0.4 Tesla at the middle of the central-cell). In the central-cell, the axial distance between the mirror throats is about 5.8 m. The central-cell is attached to the two anchor-cells. The anchor-cells are designed with minimum-B configuration. In the anchor-cell, the minimum-B configuration of the magnetic field has been generated by specially designed magnetic coils such as baseball-coils or in-yang-coils. If the minimum-B configuration has not maintained in the anchor-cell, a strong magneto hydrodynamic (MHD) instability occurs and the plasmas become unstable. The anchor-cells are attached to the two plug/barrier-cells. The east plug/barrier-cell and the west plug/barrier-cell are located close to the anchor-cells. In the plug/barrier-cells, simple mirror field is used, the mirror ratio is about 6 ($B_{\max}$ =3 Tesla, B_0 = 0.5 Tesla). The electron heating by electron cyclotron resonance heating (ECH) is applied in the plug/barrier-cell in order to form the plasma confinement potentials. Finally, the end-cells are located at the most west and east outer end.

The microwave interferometers have been installed in each cell of GAMMA 10/PDX to measure the line integrated electron density [84,87]. In addition, the diamagnetism of the plasma (plasma stored energy) has been measured by the diamagnetic loop. Three diamagnetic loops have been installed in the central-cell to measure the plasma stored energy [85]. The electron temperature and the electron density in the central-cell have been measured by the Thomson laser scattering system of yttrium-aluminum-garnet (YAG) [86]. Recently, the Thomson scattering and the microwave interferometer system have been installed in the D-module to measure the electron density and temperature in the D-module [87-88]. The end-loss ion energy analyzer (ELIEA) and the loss electron diagnostic (LED) are installed at the back of the end-plate to study the end-loss plasmas [79-80].

The study of end-cell plasma has been focused of attention because of the divertor simulation study. The divertor simulation experiments have been effectively progressed in the end-cell of GAMMA 10/PDX to realize the radiation cooling, impurity transport, MAR, plasma detachment, etc. In GAMMA 10/PDX, high heat flux can be produced by applying ECH at both plug/barrier-cells [28]. The high particle flux can also be generated by applying ICRF3 at the anchor-cells [28]. The more detailed explanation of each cell, mirror confinement, heating, plasma diagnostic and gas puffing can be found in the references [29-30, 73-76, 84-88].

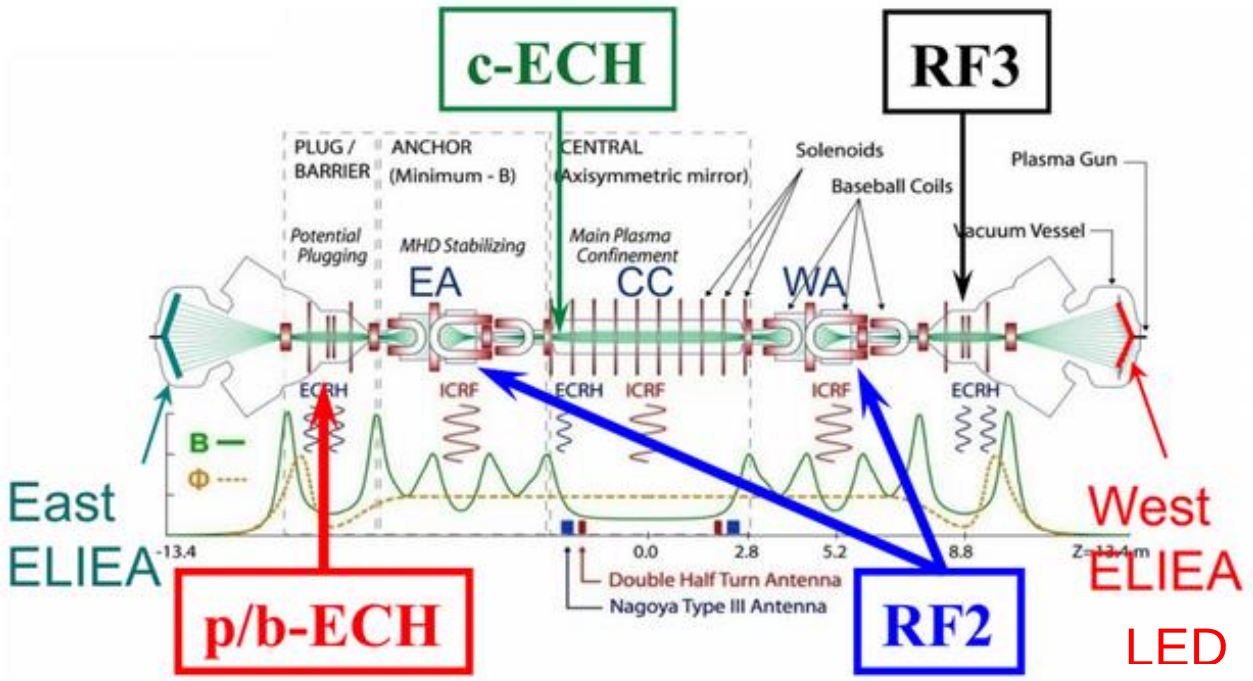

Fig. 2.1 Schematic view of the GAMMA 10/PDX tandem mirror device.

2.2 D-module

The D-module (Divertor simulation experimental module) consists of (1) a rectangular chamber, (2) a V-shaped target and (3) a gas injection system. The cross-section area and length of the D-module are about 50 × 50 cm and 100 cm, respectively. An elevation system has been installed in the west end-region to conduct both the conventional mirror experiments and the D-module experiments. As shown in Fig. 2.2, the D-module can be moved up and adjusted at the end-mirror exit to study the plasma-divertor interaction. The schematic view of the V-shaped target and diagnostics tools is shown in Fig. 2.3. Two tungsten target plates (350 ×300 mm) are mounted in V-shaped inside the D-module. The angle of the tungsten target plates can be adjusted from 15 to 80 degrees. Three types of gas injection systems have been installed in the D-module (hydrogen, He and radiator gases) to investigate the physical mechanism of plasma-neutral interactions towards the plasma detachment.

Thirteen Langmuir probes and calorimeters are installed at the upper and lower sides of the V-shape target, respectively in order to measure the distribution of heat flux in the D-module. In addition, a calorimeter and a probe are also installed in the corner of the V-shape target (Z ~ 1,091 cm) to examine degree of plasma detachment.

The heat flux is measured by the calorimeters which have been installed on the lower side of the V-shape target. The heat flux has been evaluated from the temperature difference (ΔT) of the metal substrate between before and after plasma discharge. The temperature difference (ΔT) has been measured by the thermocouple. The heat flux is represented by the following formula,

Heat flux, $\boldsymbol{P = \frac{m \times c \times \Delta T}{S \times t} \times 10^{-6}}$ [MW/m^2].

Where,

ΔT: The difference of temperature,

m: The mass of substrate,

c: The calorific capacity of substrate,

t: The plasma exposure time,

S: The collection area of the heat.

In GAMMA 10/PDX, two types of spectrometers (USB2000+ and SR500i) have been installed in the plug/barrier-cell and end-cell [89]. Figure 2.5 shows the measuring position of the spectroscopic system in GAMMA 10/PDX. In the paper, spectroscopic data for the end-cell (Z = 1073.5 cm) is given in chapter 3.

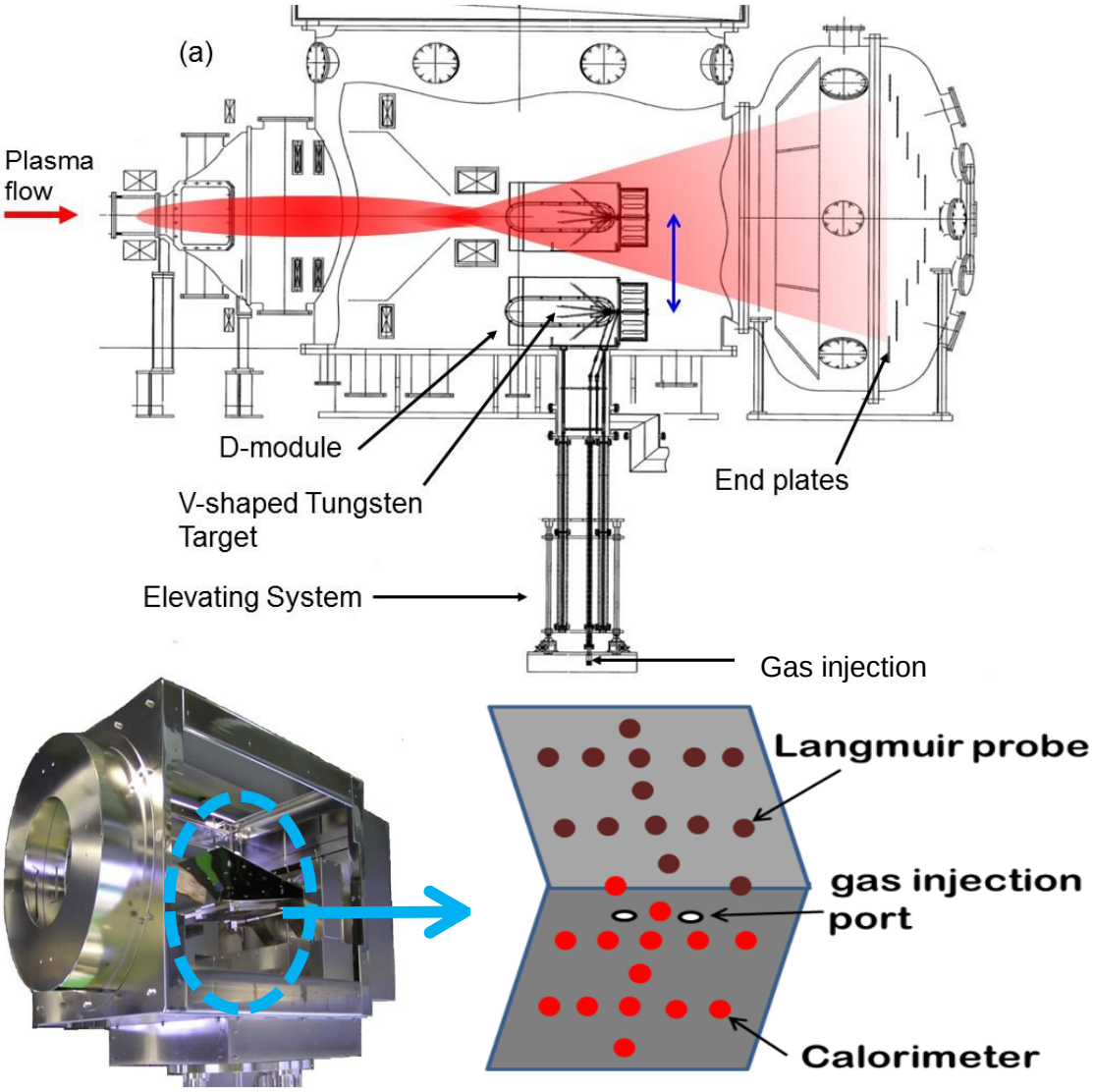

Fig. 2.2 Schematic view of the west end-cell of GAMMA 10/PDX and the D-module.

In the experiment, the distribution of heat on the V-shaped target plate was measured under the target angle of 45 degree. The schematic view of calorimeters array which has been installed on the lower side of the V-shaped target has been appeared in Fig. 2.4. The calorimeters on the Line (a) and the Line (b) measure the heat flux distribution along the ±Y directions while calorimeters on the Line (Z) measure the heat flux distribution along the Z direction. As shown in Fig 2.3, three gas injection line have been installed in the D-module. In the present experiment, Ar, Kr and Xe gases injection were injected into the D-module through gas line #3. The ASDEX gauge has been installed in the D-module in order to measure the neutral pressure inside the D-module, which is under calibration and preparation [78].

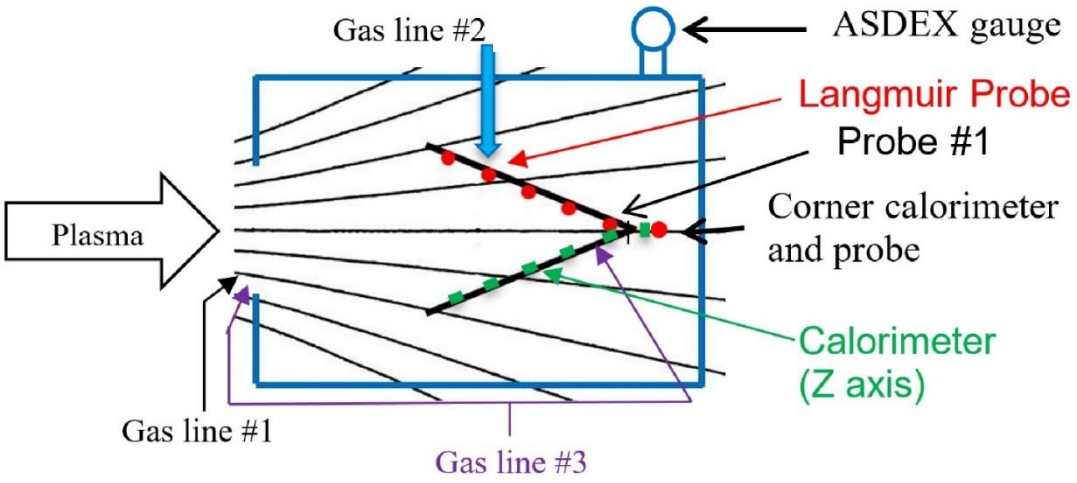

Fig. 2.3 Schematic view of the D-module, diagnostics tools and gas injection line.

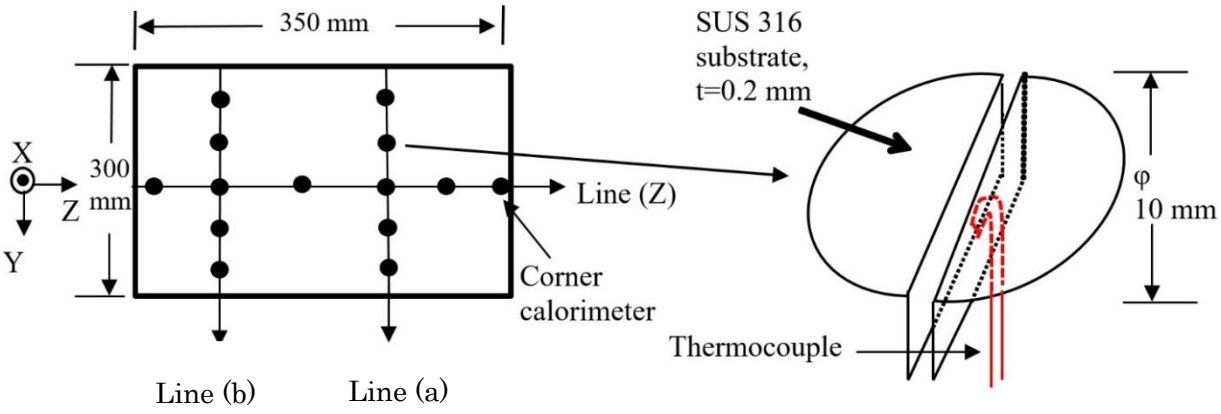

Fig. 2.4 Schematic view of the calorimeter array in the lower side of V-shape target.

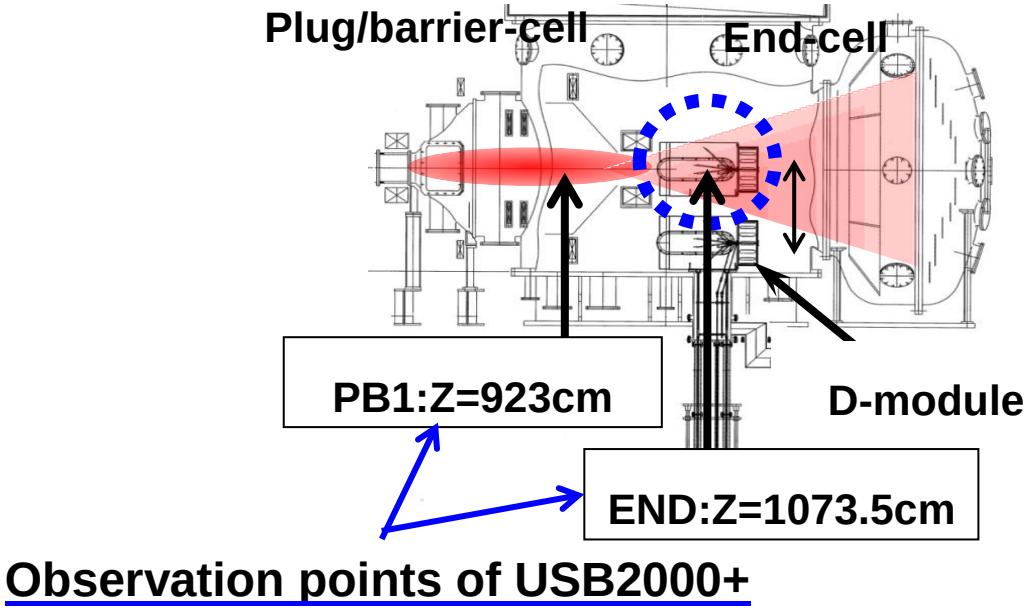

Fig. 2.5 Schematic view of the observation points of spectrometer at the west plug/barrier-cell and end-cell.

Chapter 3 Experimental Results

In fusion devices, the divertor concept has been developed in order to suppress the direct plasma-surface interactions and to decrease the transportation of impurities into the core plasma region. However, the high flux strikes into the divertor region. Thus, it is a critical task to protect the divertor target plate from the high upstream heat flux. Physical and chemical erosion are produced on the target plate because of the high heat-load. Therefore, evaluation of a plasma cooling mechanism is an important research subject to operate the future fusion devices. Since the radiator gas injection increases the radiation power loss, radiator gas injection into the divertor is one of the promising concepts to minimize the heat-load on the divertor plates. However, the radiation power loss of the gases is different. As a result, radiator gasses injection experiments have been effectively done by making the best use of GAMMA 10/PDX to explore the effects of the radiator gases on the plasma detachment. Sustainment of detached plasmas in case of high heat flux is also an important research subjects to understand the divertor physics. Hence, the transition of detached and attached plasma has also been focused in this study.

In this chapter, section 3.1 describes results and discussion for radiator gases injection into the D-module. Section 3.2 describes the transition of detached to attached experiments. Discussion is presented in section 3.3.

3.1 Radiator gases injection

In the present experimental condition, gases injection (Ar, Kr and Xe) were carried out under the plenum pressure of 100 mbar to 500 mbar. It is speculated that the real gas pressure inside the D-module is about 0.1 to few Pa. In the future, the real pressure inside the D-module will be measured by the ASDEX-gauge [93]. The timing chart for the impurity injection is tabulated in Table 3.1. The gases were injected into the D-module 0.8 s before than that of the plasma discharge and the gas valve was open to flow the gas into the D-module for 1.0 s. The schematic drawing of the impurity pressure inside the D-module is plotted in Fig. 3.1. The D-module is located in the west end-region and has a closed box condition. The neutral impurity gases were injected into the D-module before the plasma enters into the D-module and consequently, the neutral density remains uniform in the D-module during the plasma discharge. As for the hydrogen neutral model, the recycling flux increases the neutral density near the target.

Figures 3.2-3.4 show the time behavior of the electron line-density (NLcc,) and the diamagnetism (DMcc) measured in the central-cell by the multi-channel microwave interferometer system. DMcc depends on the perpendicular ion temperature and density. Increase in the NLcc and decrease in the DMcc is observed for Ar, Kr and Xe seeding. However, the NLcc and DMcc remain almost stable

during Ar, Kr and Xe gasses puffing, which indicates that reproducibility of the central-cell plasmas did not affect significantly due to the Ar, Kr and Xe seeding. The time behavior of electron line density in the west anchor-cell is shown in Fig. 3.5. The electron line density remains also constant in the anchor-cell during impurity gases injection into the D-module, which indicates the plasma parameters in the anchor-cell did not affect remarkably due to the impurity injection into the D-module.

Table 3.1. Timing chart of impurity injection.

Gas	Delay (s)	Pulse Width (s)	Shot number
Ar	-0.8	1.0	237737-41
Kr	-0.8	1.0	237722-28
Xe	-0.8	1.0	237731-35

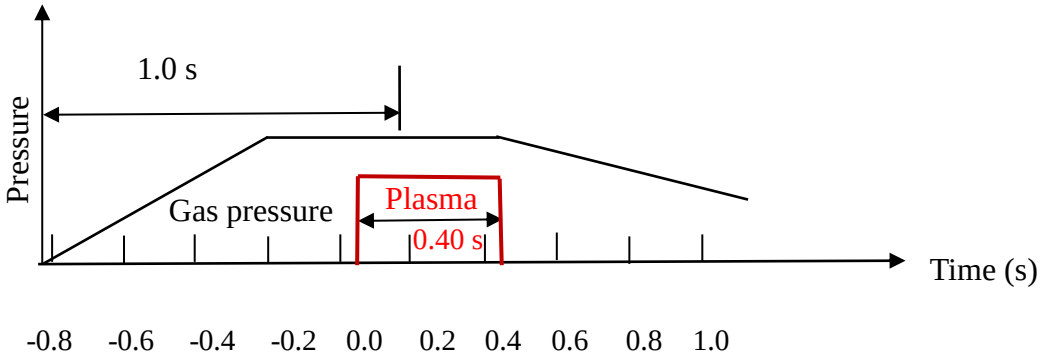

Fig. 3.1 Schematic drawing of the gas timing.

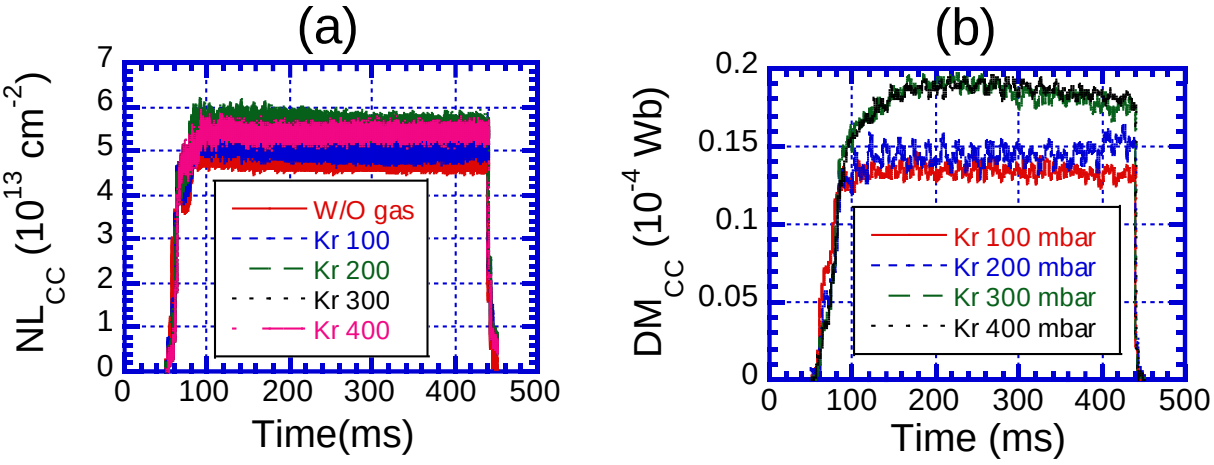

Fig. 3.2 Time behavior of the NLcc (a) and DMcc (b) in the central-cell for Kr injection.

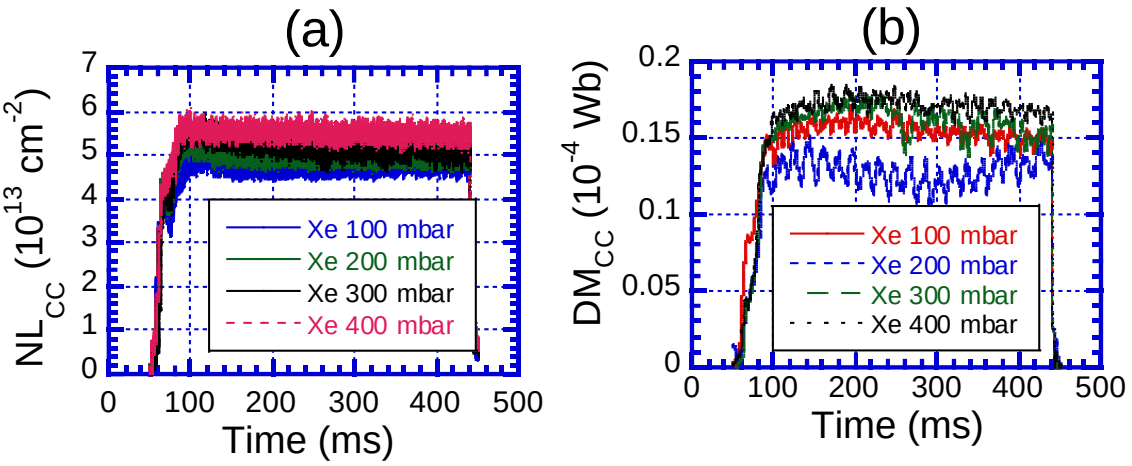

Fig. 3.3 Time behavior of the NLcc (a) and DMcc (b) in the central-cell for Xe injection.

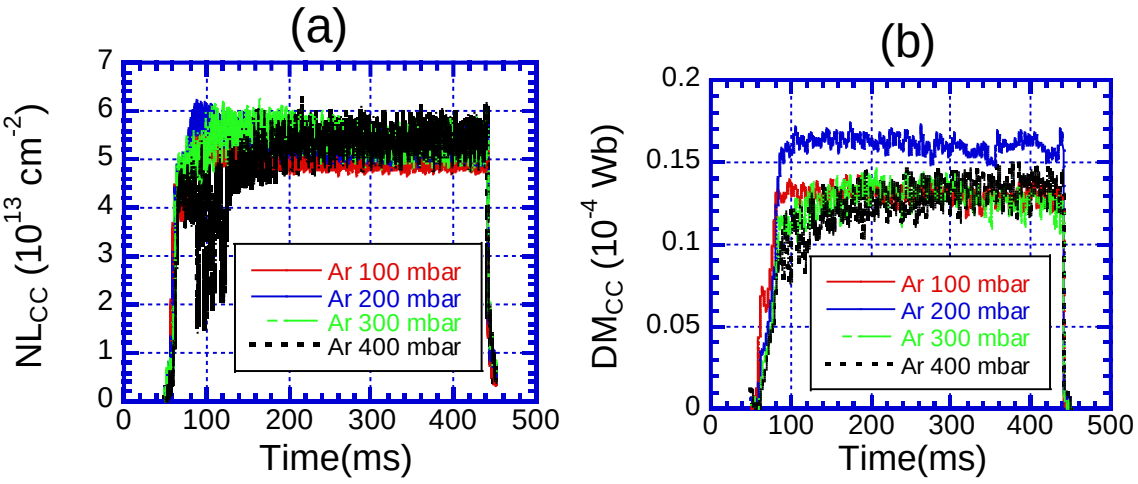

Fig. 3.4 Time behavior of the NLcc (a) and DMcc (b) in the central-cell for Ar injection.

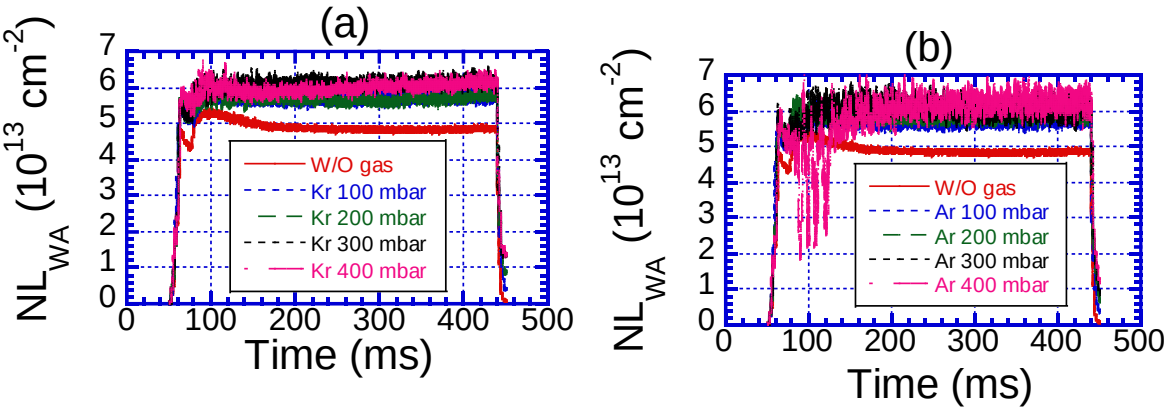

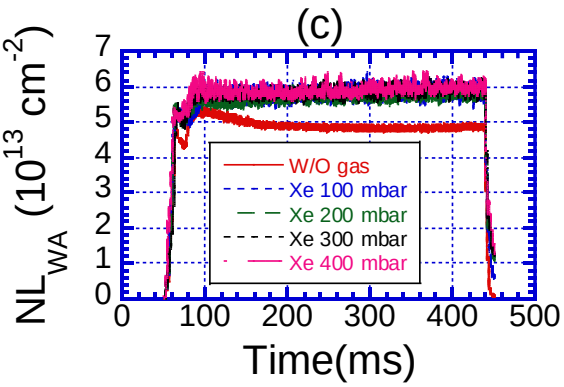

Fig. 3.5 Time behavior of the electron line density in the west anchor-cell (a) Kr (b) Ar and (c) Xe injection.

3.1.1 Ar Injection

The plasma parameters in the D-module have been investigated during Ar injection. The distribution of heat flux along the Z and Y-axis is plotted in Fig 3.6 (a) and (b), respectively. The heat flux profile on the Z-axis is almost uniform for without gas injection experiment. However, the heat flux reduces along the Z-axis during Ar injection. The plasma-neutral interactions take place near the inlet of the V-shape target. Figure 3.6(a) shows the distribution of the heat flux on the Z-axis. The heat flux reduces toward the plasma downstream. The heat flux also reduces with the increasing Ar injection. From these results, it seems that strong interactions between radiator gas and plasmas take place near the inlet of the D-module. It is speculated that the ionization-front creates near the inlet of the D-module. Therefore, the heat flux reduces monotonically towards the plasma downstream. On the other hand, the distribution of the heat flux along the $\pm$Y directions is shown in Fig. 3.6 (b). Distribution of plasma depends on the magnetic field structure. The line of magnetic field in GAMMA 10/PDX end-cell spreads toward the radial direction, i.e. magnetic flux density is lower in the radial direction. As a result, the heat flux distribution has a peak at Y=0 [cm] and the heat flux decreases toward the $\pm$Y directions. Calorimeters near to the Z-axis are exposed to high heat-flux. On the other hand, the calorimeters are located far from the center-axis of the target plate exposed to low heat flux. Therefore, the heat flux reduces toward the $\pm$Y directions. The distribution of the heat flux without gas injection is steeper than that of gas injection experiments. According to the increment of Ar gas puffing into the D-module, the heat flux distributions become uniform. For Ar injection at the plenum pressure of 500 mbar, the distribution of heat flux is almost uniform. These outcomes indicate that the reduction in the heat flux on the target plate is due to Ar injection. The heat flux can be expressed by the following formula,

$$P_{\text{heat}} = \alpha_e n_e u_e T_e + \alpha_i n_i u_i T_i. \quad (3.1)$$

Where, α_e and α_i represent the heat transmission coefficient through the sheath entrance for the electron and ion, respectively, n_e and n_i are the electron and ion density, T_e and T_i are the electron and ion temperature, u_e and u_i are the parallel velocity for the electron and ion.

In GAMMA 10/PDX, the heat flux is dominated by the ion temperature because of high ion temperature. Reduction in the heat flux indicates the reduction in the ion temperature. These results indicate that Ar gas injection into the divertor region reduces both the electron and ion temperature. Bolometric measurement and Ion sensitive probe measurement are very much important to clarify the energy loss processes in GAMMA 10/PDX. In GAMMA 10/PDX, electron gains energy during interactions with ions. As a result, reduction in the heat flux strongly indicates the reduction in the ion temperature.

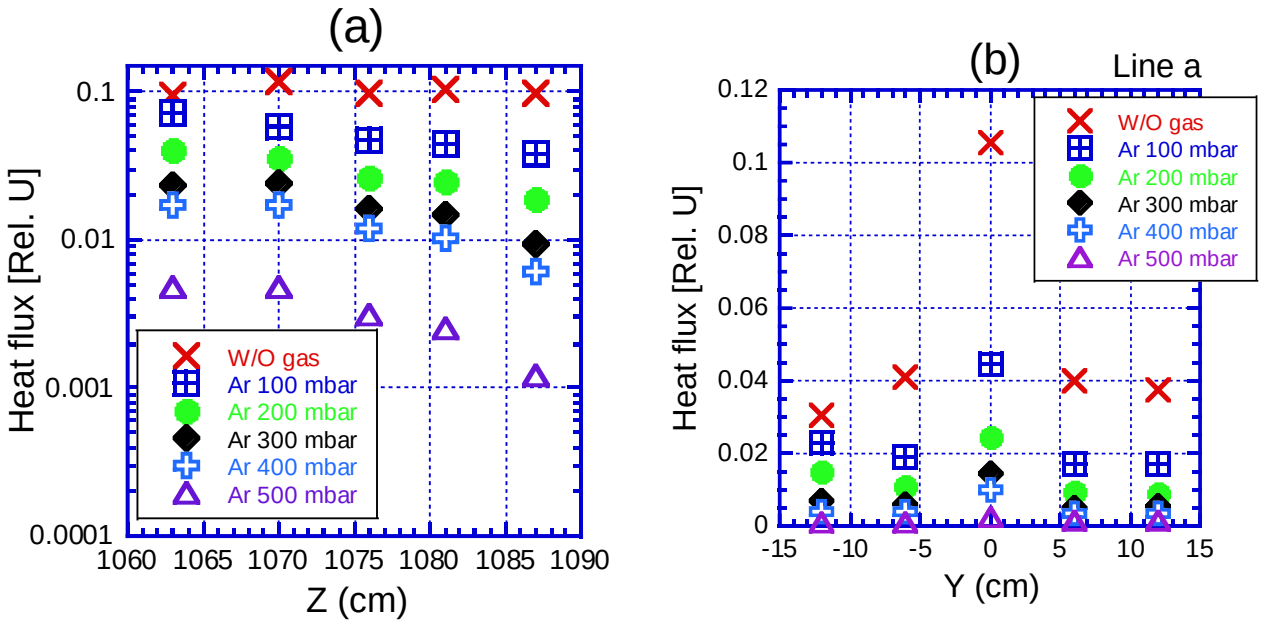

Fig. 3.6 Distribution of heat flux (a) Z-axis and (b) Y-axis.

The time behavior of the ion flux is shown in Fig 3.7. The ion flux increases slightly with time in case of without gas injection experiments. However, the time behavior has been changed during Ar injection experiment. The ion flux on the target plate can be written by the following formula,

$$\Gamma_{\text{target}} = \Gamma_{source} - \Gamma_{sink}. \quad (3.2)$$

The ion flux depends on the sources and sinks terms in the divertor regions. Thus, the ion flux can be decreased by the following channels,

(1) decrease in the source terms such as ionization, excitation, etc.,

(2) increase in the sink terms such as volume recombination, momentum losses, radiation power losses, etc.

Ar injection increases significantly the electron power loss channels by increasing the radiation power loss. Ionization effects of Ar particles also play a key role to reduce the electron temperature. The recombination processes (MAR and EIR) become active at the low temperature. Reduction in the ion flux indicates that the recombination processes become active with the increasing Ar injection into the D-module.

Figure 3.8 (b) shows the dependence of the heat and ion fluxes (measured by the corner calorimeter and probe) on the Ar plenum pressure which has been measured in the corner of the V-shaped target (~Z=1,091 cm). As plotted in Fig. 3.8 (b), it is shown that the heat flux reduces according to the increasing Ar injection into the D-module. The ion flux also reduces with the increasing Ar injection. The dependence of T_e and n_e is also plotted in Fig 3.8 (a). Here, increase in the electron density firstly occurs due to Ar injection and then the electron density reduces according to the increment of Ar injection. The electron density shows a so-called roll-over phenomenon during Ar seeding. The T_e in the corner of the target plate decreases to nearly 2 eV by only Ar injection. These outcomes indicate that the end-loss plasmas of GAMMA 10/PDX become detached in the D-module due to the Ar seeding.

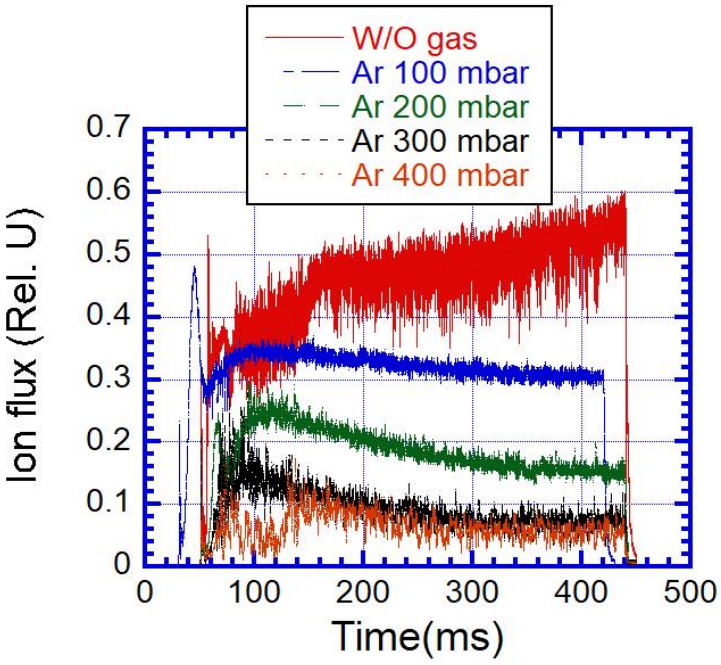

Fig. 3.7 Time behavior of ion flux measured in the corner of the target plate.

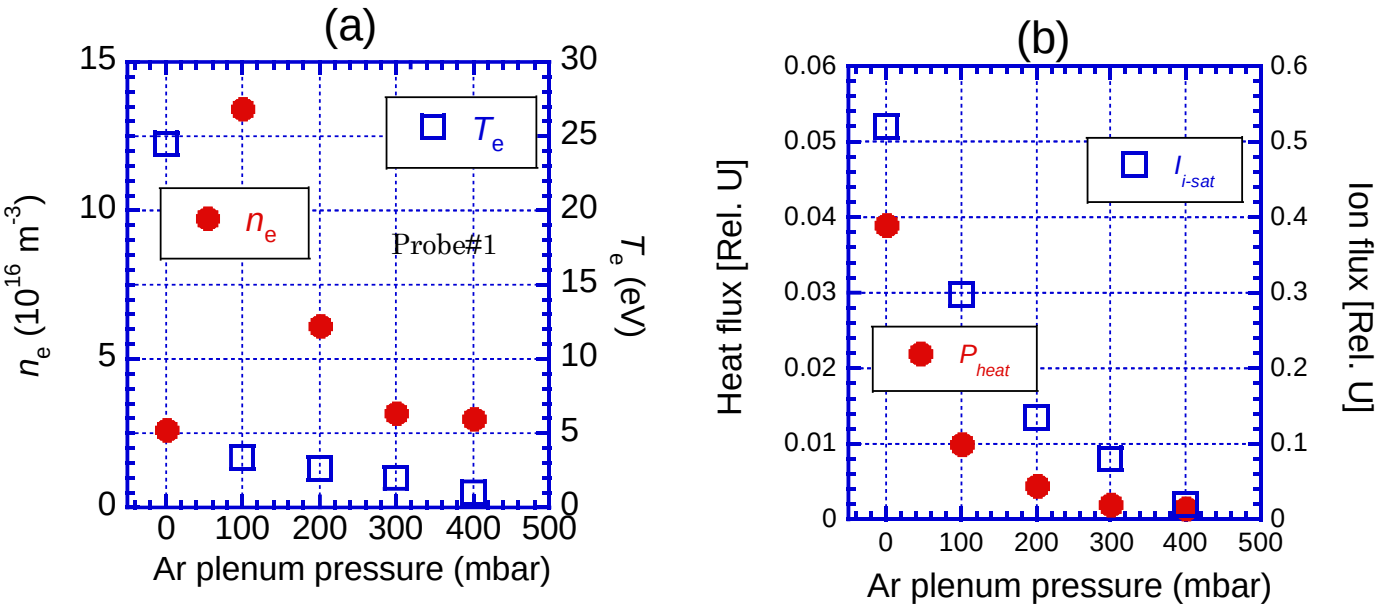

Fig. 3.8 Dependence of the (a) electron temperature, T_e and electron density n_e and (b) heat and ion fluxes as a function of Ar plenum pressure.

3.1.2 Kr Injection

The plasma parameters in the D-module have also been investigated during Kr injection to explore the effects of Kr on the plasma detachment. The distribution of heat flux along the Z and Y-axis is shown in Fig 3.9 (a) and (b), respectively. The heat flux profile on the Z-axis is almost uniform for without gas injection experiment. However, the heat flux reduces along the Z-axis during Kr injection. The heat flux reduces toward the plasma downstream. The heat flux also reduces with the increasing Kr injection. From these results, it seems that strong interaction between radiator gas and plasmas take place near the entrance of the D-module. It is speculated that the ionization-front creates near the entrance of the D-module. Therefore, the heat flux reduces monotonically towards the plasma downstream. On the other hand, the distribution of the heat flux on the $\pm$Y directions is shown in Fig. 3.9 (b). Distribution of plasma depends on the magnetic field structure. The line of magnetic field in GAMMA 10/PDX end-cell spreads toward the radial direction, i.e. magnetic flux density is lower in the radial direction. So, the heat flux distribution has a peak at Y=0 [cm] and heat flux decreases toward the $\pm$Y directions. Calorimeters near to the Z-axis are exposed to high heat-flux. On the other hand, the calorimeters are located at a distance from the center axis of the target plate exposed to low heat flux. Therefore, the heat flux reduces toward the $\pm$Y directions. The distribution of the heat flux without gas injection is steeper than that of gas injection experiments. According to the increment of Kr gas seeding, the heat flux distribution becomes uniform. For Kr injection at the plenum pressure

of 500 mbar, the distribution of heat flux is almost uniform. These outcomes indicate that the reduction in the heat flux.

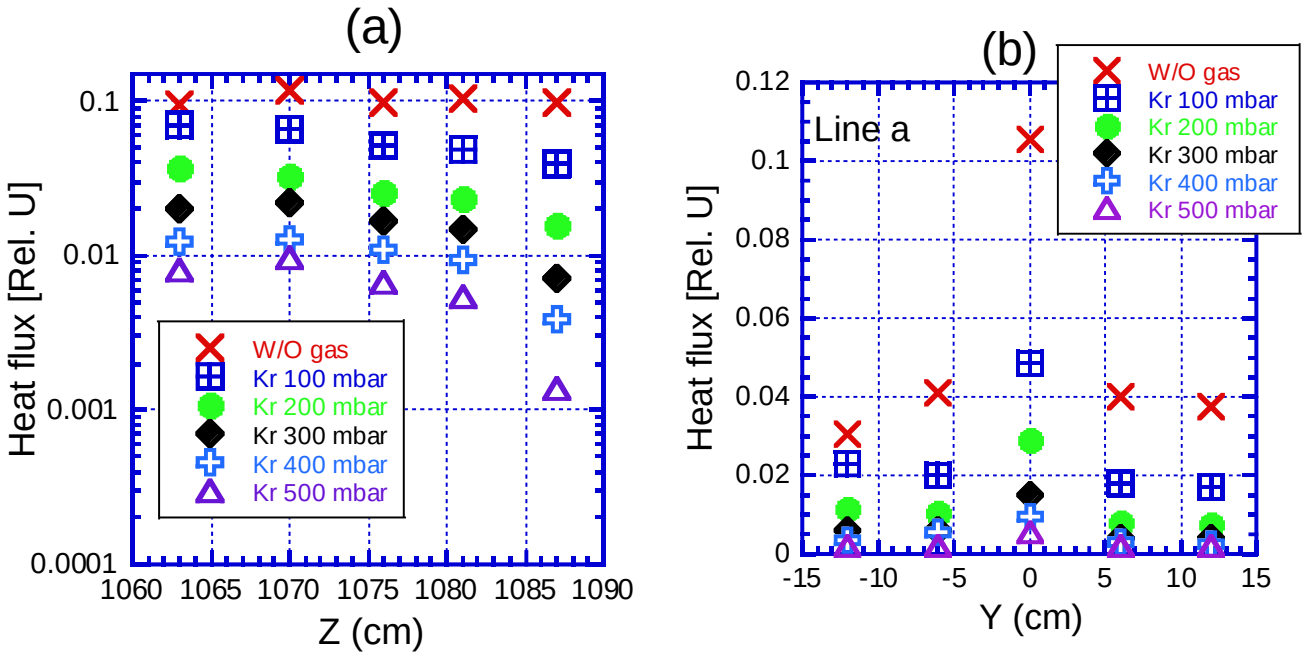

Fig. 3.9 Distribution of heat flux (a) Z-axis and (b) Y-axis.

The time behavior of the ion flux is plotted in Fig. 3.10. The ion flux reduces significantly during Kr injection comparing to the Ar injection. The ion flux also reduces with the increasing Kr plenum pressure. For the Kr injection under the plenum pressure of 400 mbar, the ion flux reduces significantly.

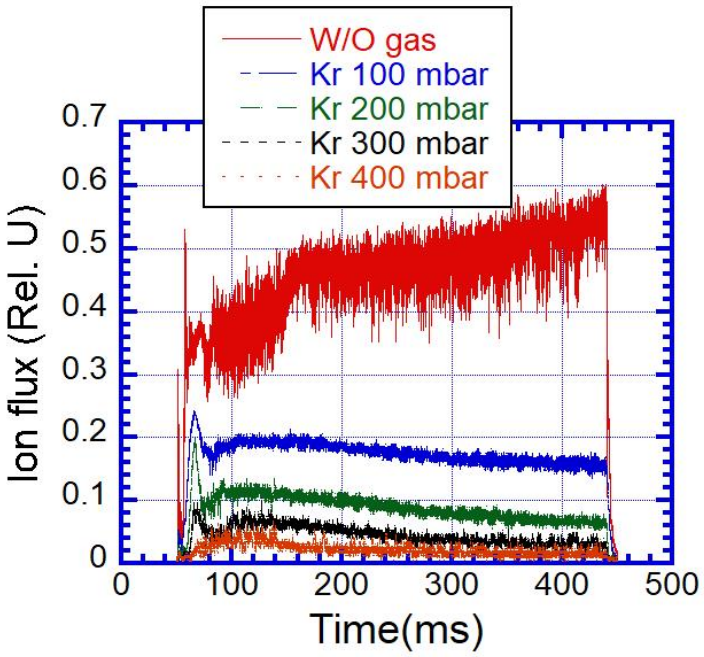

Fig. 3.10 Time behavior of ion flux measured in the corner of the target plate.

The dependence of the parameters against the Kr plenum pressure is shown in Fig. 3.11. At the lower Kr injection, the electron density increases due to the ionization effects of Kr injection. However, at the higher Kr injection, the electron density reduces. The electron density shows a roll-over phenomenon for Kr injection. In Fig. 3.11 (a), the electron temperature is also plotted as a function of the Kr plenum pressure. It is shown that the electron temperature reduces drastically for Kr injection. For only Kr 100 mbar injection, the electron temperature near the target plate reduces to about 2.7 eV. The electron temperature becomes saturated with the increasing Kr injection. The heat flux (measured by the corner calorimeter) is also plotted in Fig. 3.11 (b). The heat flux reduces monotonically with the increasing Kr injection. For the strongest Kr injection, the heat flux reduces significantly. The ion flux (measured by the corner probe) also reduces monotonically according to the Kr injection. These results indicate that the detached plasma has been generated due to the Kr injection. It is also found that the reduction in the ion flux, heat flux and electron temperature for Kr seeding is higher than that of Ar seeding.

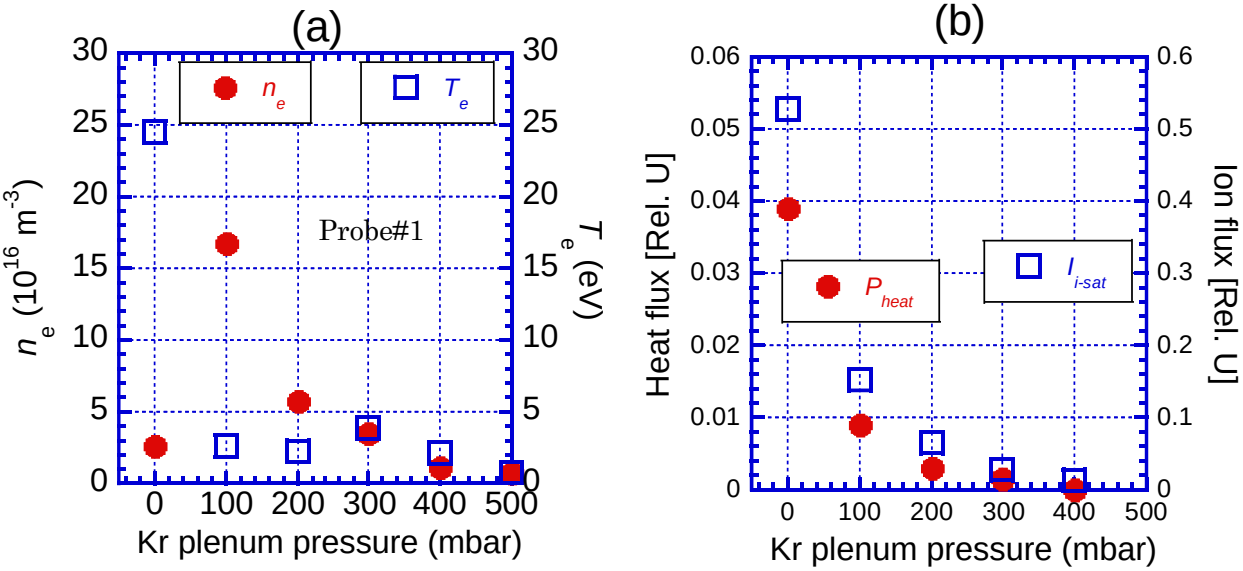

Fig. 3.11 Dependence of the (a) electron temperature, T_e and electron density n_e and (b) heat and ion fluxes as a function of Kr plenum pressure.

3.1.3 Xe Injection

The heat flux distribution during Xe injection along the Z-axis of D-module is shown in Fig. 3.12(a). The heat flux reduces toward the plasma downstream. Here, reduction in the heat flux has also been observed with the increasing of gas seeding. The distribution of heat flux along the ±Y directions is shown in Fig. 3.12(b). In this case, the heat flux distribution has a peak at Y=0 cm and reduces towards the ±Y directions. The heat flux distribution becomes uniform with the increasing gas throughput. For Xe injection at the plenum pressure of 400 mbar, the heat flux distribution is almost uniform. The dependence of T_e and n_e is plotted in Fig 3.13(a). At the Xe injection of 100 mbar plenum pressure, it is observed that electron density rises from 2.6 $\times 10^{16}$ m^{-3} to 39 $\times 10^{16}$ m^{-3} which indicates that Xe interacts strongly with plasmas in front of the V-shaped target. Therefore, the electron density rises and electron temperature reduces to about 2.4 eV by only Xe injection at the plenum pressure of 100 mbar. Reduction in the electron density is also observed with the increasing Xe injection. The T_e on the target plate decreases to about 1 eV for Xe seeding at the plenum pressure of 400 mbar. Figure 3.13 (b) shows the dependence of the heat and ion fluxes on the Xe plenum pressure which has been measured in the corner of the V-shaped target (~Z= 1,091 cm). From the figure, it is shown that the heat flux reduces with the increasing Xe seeding into the D-module.

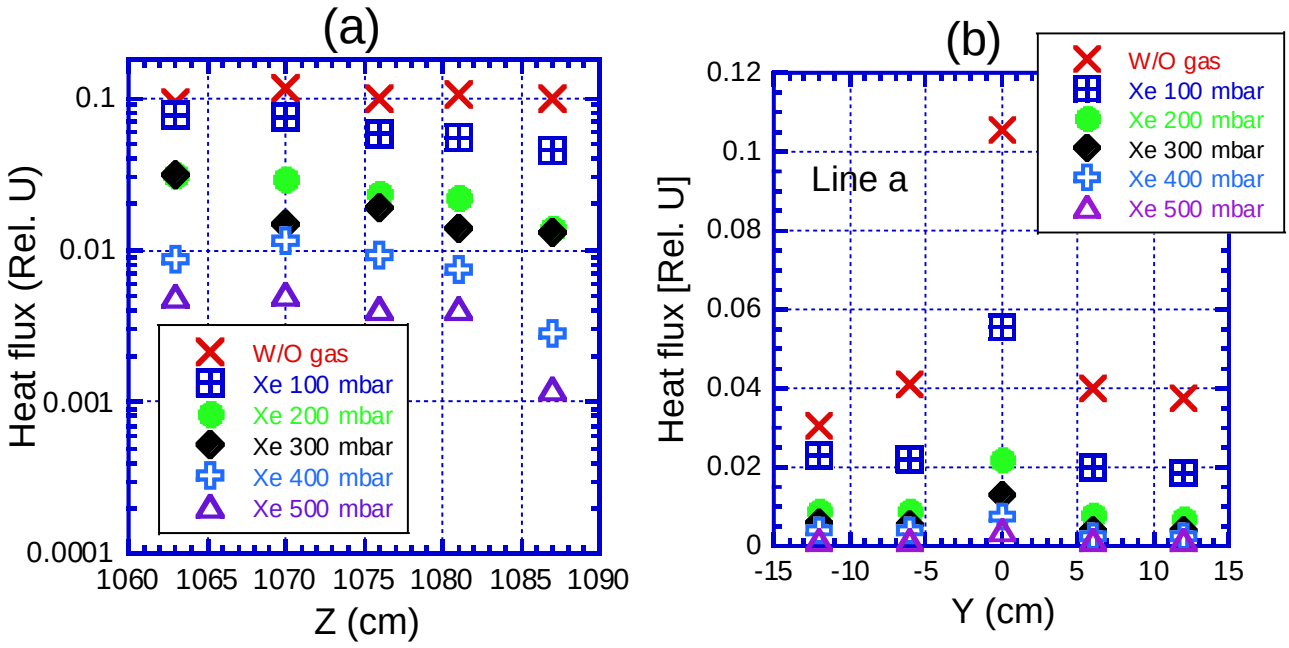

Fig. 3.12 Distribution of heat flux (a) Z-axis and (b) Y-axis.

The ion flux reduces drastically during Xe injection. These results indicate that Xe is the most effective radiative gas on the radiation cooling than that of Ar and Kr.

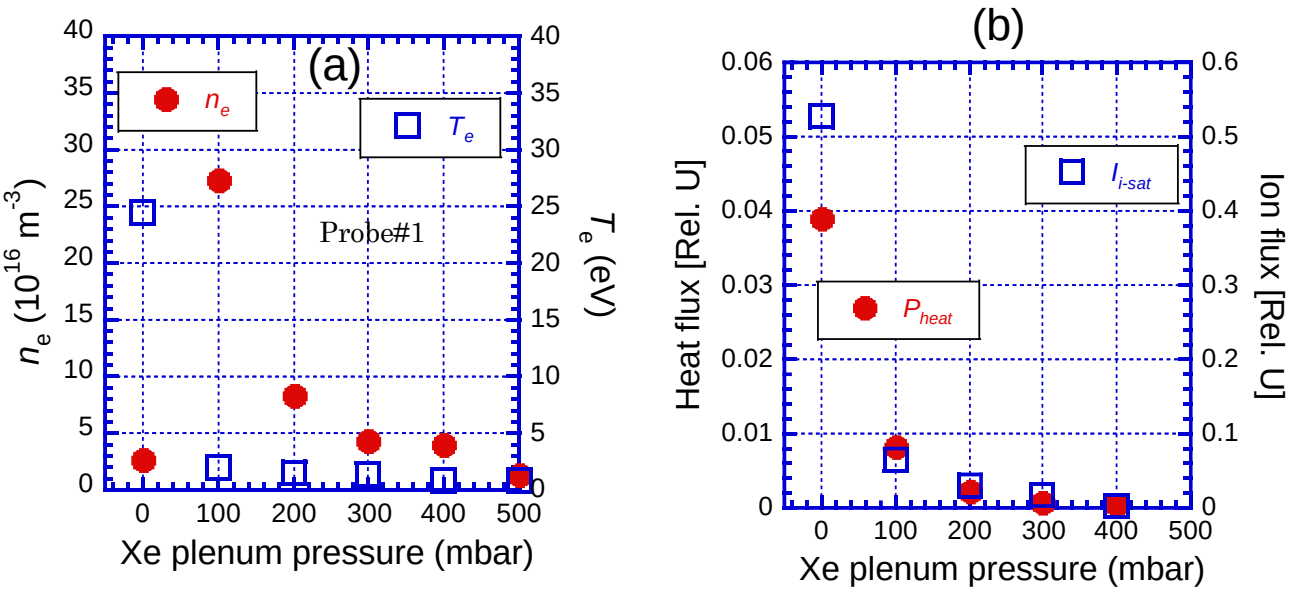

Fig. 3.13 Dependence of the (a) and electron temperature T_e, and density n_e measured by the probe #1 (b) heat and particle fluxes as a function of Xe plenum pressure.

The time behavior of the ion flux in case of Xe injection is plotted in Fig. 3.14. The ion flux reduces drastically for Xe seeding compared with the Kr and Ar seeding. The ion flux also reduces with the increasing Xe plenum pressure. For the Xe injection under the plenum pressure of 200 mbar, the ion flux reduces significantly.

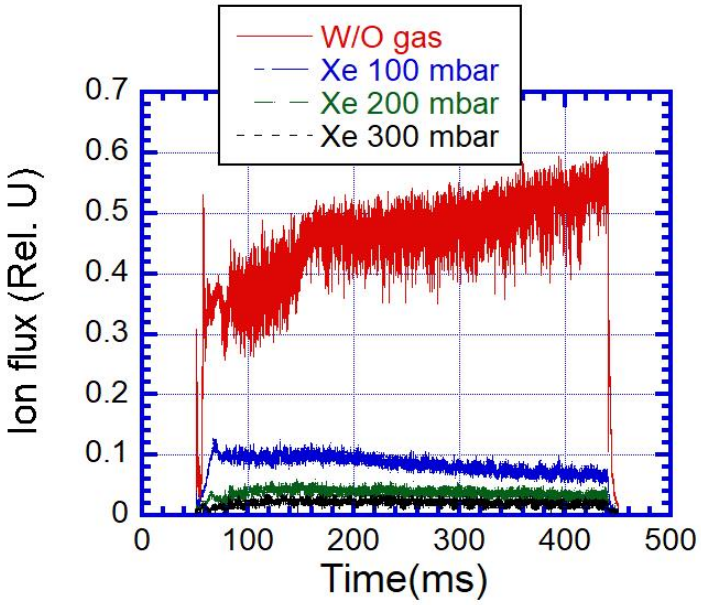

Fig. 3.14 Time behavior of ion flux measured in the corner of the target plate.

3.2 Transition of detached to attached state

The behavior of detached plasma in case of high heat flux condition is an important research subjects for studying the sustainment of detached plasma physics. GAMMA 10/PDX is designed with many plasma heating systems. Figure 3.15 shows schematic view of GAMMA 10/PDX. As shown in Fig. 3.15, a short pulse of ECH was applied at the east plug/barrier-cell to examine the effects of ECH on the sustainment of plasma detachment. The end-loss plasmas parameters have been measured by the LED (Loss Electron Diagnostic) and ELIEA (End-loss Ion Energy Analyzer) before starting the D-module experiment. During the end-loss plasmas measurement by the LED and ELIEA, the D-module was moved-down. The electron temperature has been measured by the LED diagnostics system at the west end-cell [80].

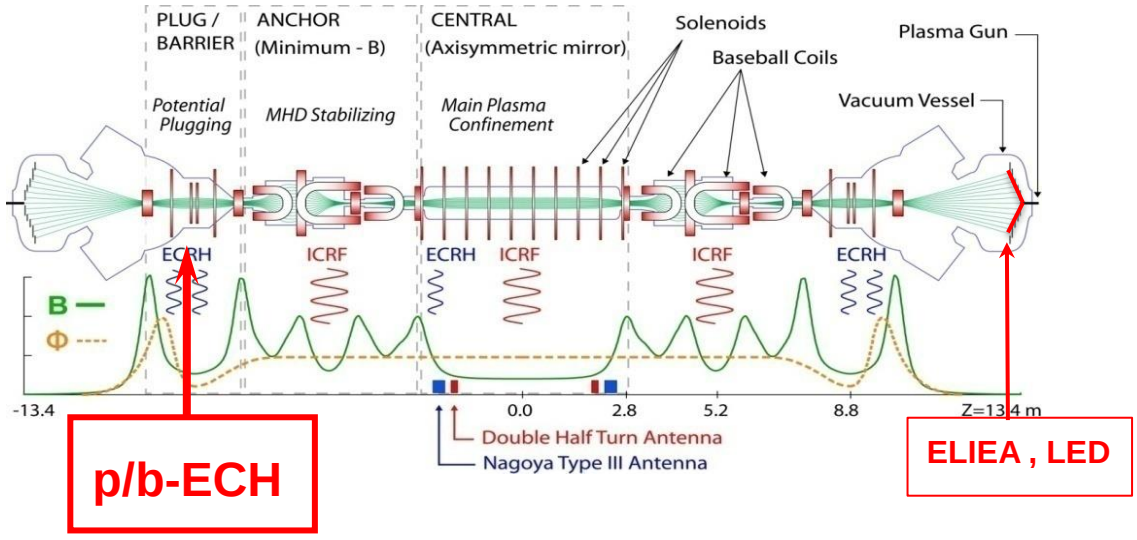

Fig. 3.15 Schematic view of the GAMMA 10/PDX.

Figure 3.16 shows the dependence of electron temperature, ion temperature and ion current density on the ECH power. It is shown that a short pulse (25 ms) of ECH injection in the east plug/barrier-cell significantly increases the electron temperature at the west end-cell. As shown in Fig. 3.16, a clear dependence of ECH power on the electron temperature has also been observed. The electron temperature increases with the increasing ECH power. ECH heating effects in the east plug/barrier-cell increase the hot electron flow toward the central-cell and consequently toward the end-cell. As a result, the electron temperature increases when ECH was applied in the east plug/barrier-cell. The ion temperature and ion current density have also been measured by the west ELIEA system [79]. ECH injection has no direct impact on the ion temperature. However, a slight increase in the ion temperature has been observed for ECH injection. The ion current density remains almost constant with the increasing ECH power. A slight reduction in the ion current density has been observed at the higher ECH power.

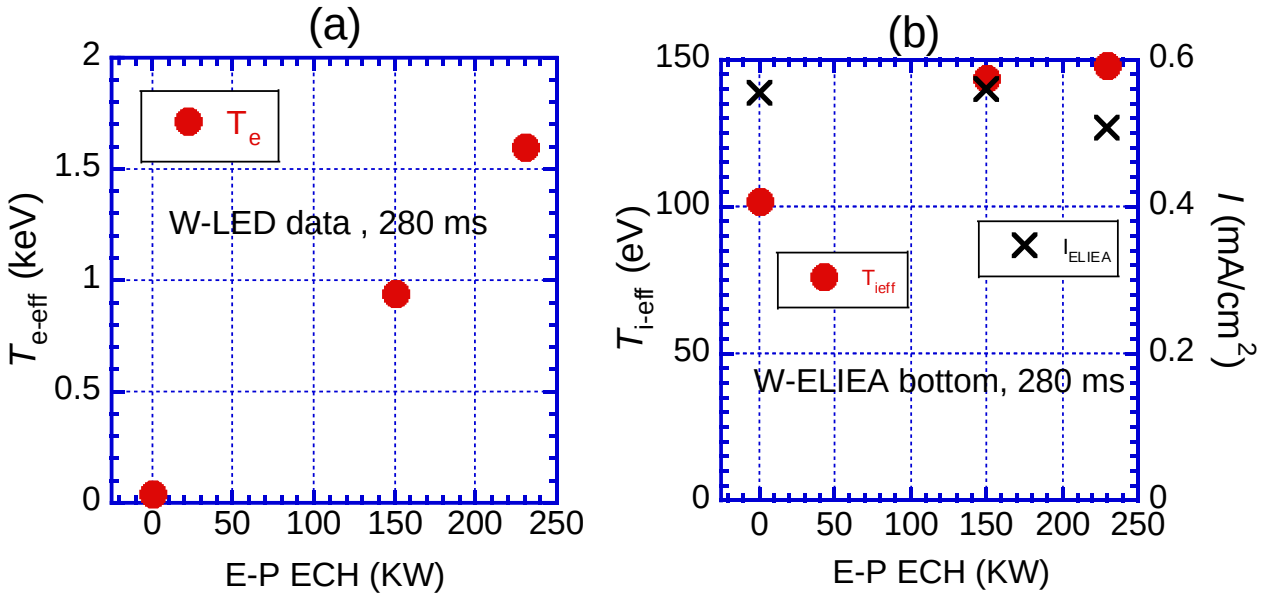

Fig. 3.16 Dependence of (a) electron temperature, and (b) ion temperature and current density as a function of the ECH power.

During plasma detachment experiments by Xe seeding, an additional heating pulse of ECH was applied at the east plug cell to examine behavior of the radiator gases on the formation of detached plasma in case of high heat flux condition (such as ELM). The central-cell electron line density (NLcc) is plotted in Fig. 3.17. It is shown that the NLcc increases during ECH injection (time 275-300ms, power: 150 kW). ECH heating effects in the east plug-cell increase the hot electron flow towards the central-cell, which increases ionization of neutral particles. NLcc also increases during impurity gas injection into the D-module. Xe injection into the D-module also shows a little influence on the NLcc. A slight increase in the NLcc is observed due to the Xe injection into the D-module. The NLcc remains almost constant for Xe injection. ECH injection at the plug/barrier-cell generates the plug potential for ions which significantly enhances the plasma confinement as shown in Fig 3.15. Thus, the NLcc increases during ECH application period due to the improvement of plasma confinement and enhancement of ionization. The ion flux at the corner of the V-shape target is also plotted in Fig. 3.17. A slight increase in the ion flux is observed for ECH injection. Once Xe is injected into the D-module, the ion flux reduces drastically. On the contrary, the ion flux increases drastically during ECH injection period. The increase in the ion flux mainly comes from the Xe ions. The application of ECH increases the electron temperature, which strongly interacts with the cold Xe neutral in the D-module. As a result, ionization of Xe particles plays a driving role in the case of ECH heating effects on the detached plasma in the D-module. More detailed spectroscopic measurement will be conducted in the near future.

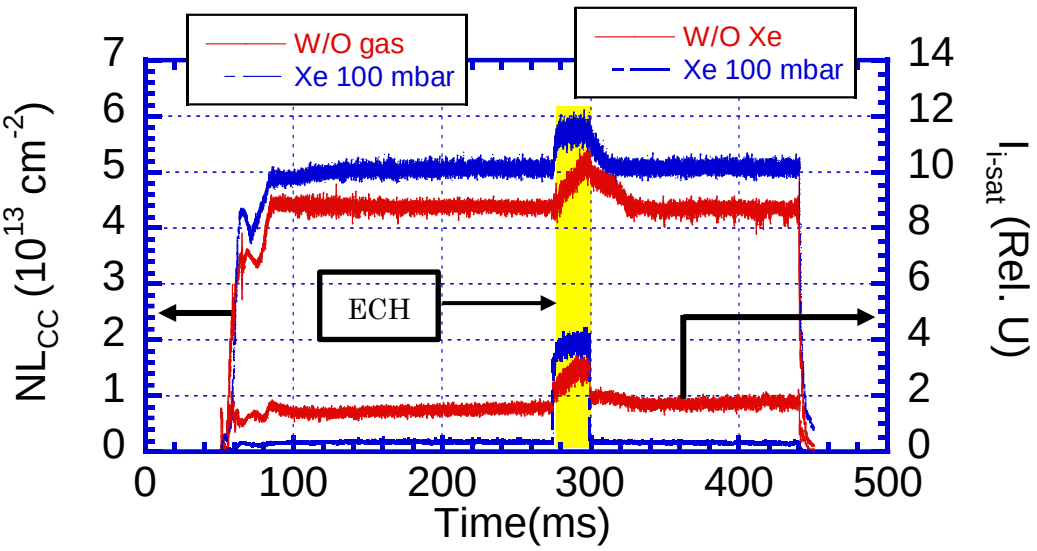

Fig. 3.17 Time behavior of the central-cell electron line density and the ion flux at the corner of the V-shape target.

The dependence of the ECH power on the heat flux has also been investigated in the study. Figure 3.18 shows the dependence of the heat flux on ECH power. The heat flux reduces drastically with the increment of Xe plenum pressure in case of without ECH application. The heat flux is a time averaging value for the 400 ms plasma discharge. A short pulse (~25 ms) of ECH strongly increases the heat flux. The heat flux also increases with the increasing ECH power except for the ECH 100 kW in case of without gas injection. The heat flux reduces with the increasing Xe plenum pressure but the reduction rate is lower than that of only ICRF heated plasmas.

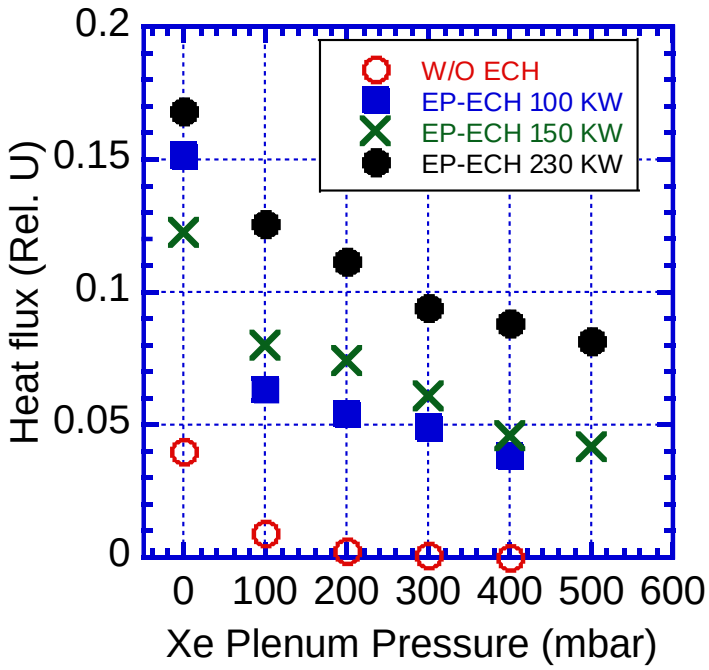

Fig. 3.18 Dependence of the heat flux as a function of ECH power.

The distribution of the heat flux on the Z-axis has also been measured. The distribution of the heat flux on the Z axis is shown in Fig. 3.19. The distribution of heat flux in case of ECH injection is different than that of only ICRF heated plasmas. In the case of ECH injection with the ICRF plasmas, the peak of the heat flux appears at Z 1070 cm. On the other hand, the peak of the heat flux appears near the inlet of the target for only ICRF heated plasmas. It is speculated that ECH injection changes the ionization-font in the D-module. The heat flux reduces with the increasing Xe injection. For Xe injection under the plenum pressure of 500 mbar, the heat flux reduces below the typical ICRF heated plasmas. It seems that the attached plasma approaches toward the plasma detachment state. The generation of plasma detachment by Xe seeding has not yet observed for the ECH heated plasmas so far. The time behavior of the ion flux is plotted in Fig. 3.20. During ECH injection period, the ion flux increases with the increasing Xe injection, however, the electron line density in the central-cell remains almost constant. The ion flux also increases with the increasing ECH power.

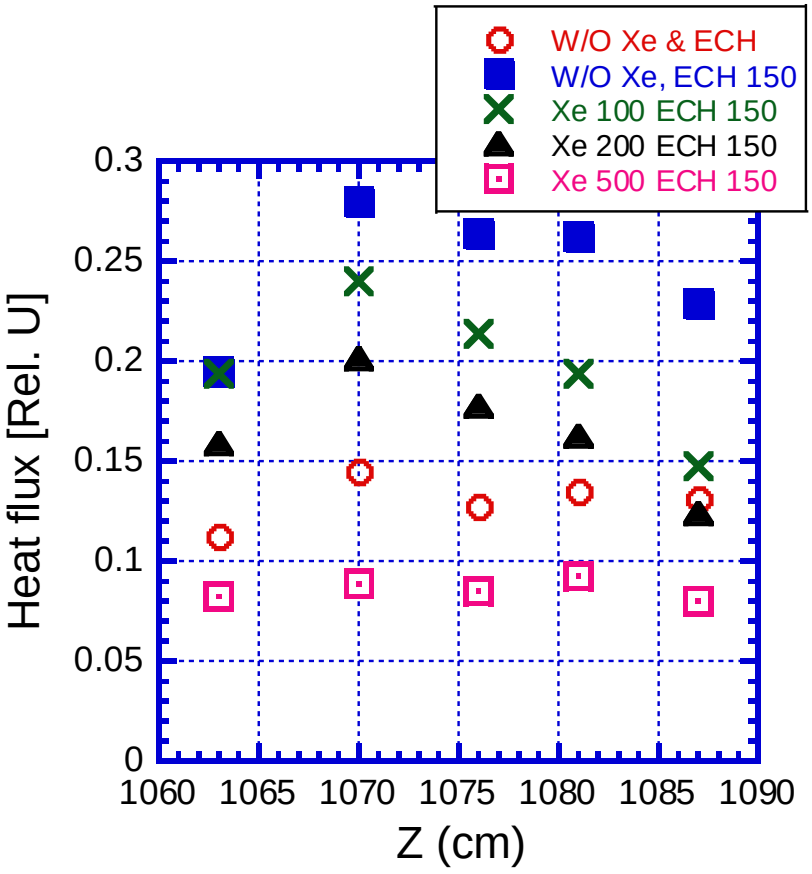

Fig. 3.19 Distribution of heat flux on the Z-axis.

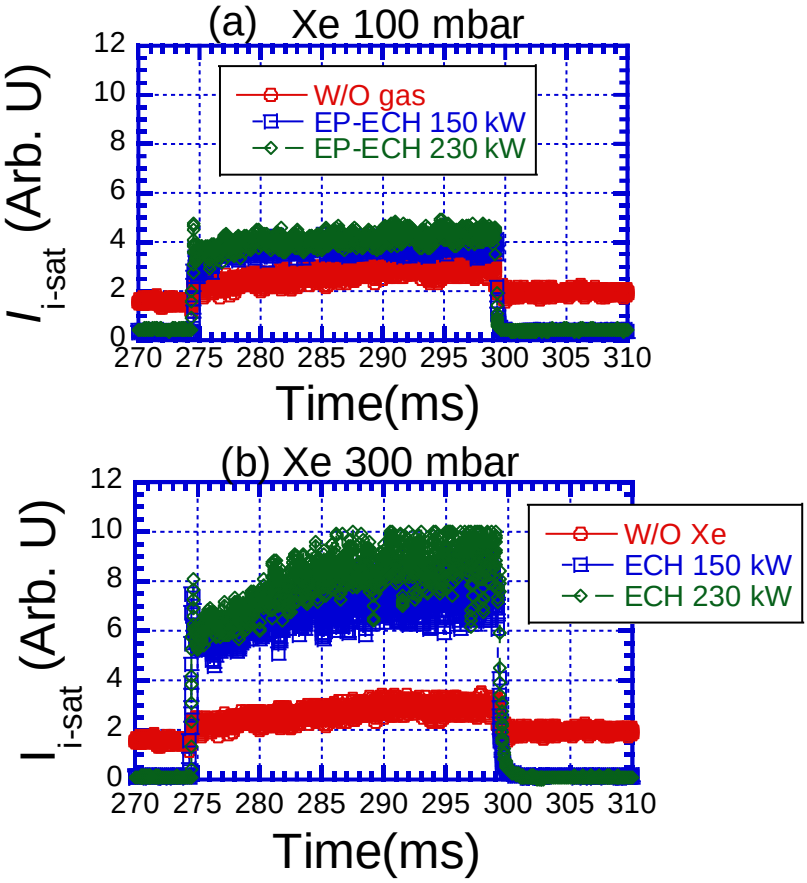

Fig. 3.20 Time behavior of the ion flux (a) Xe 100 mbar and (b) Xe 300 mbar in the corner of the V-shape target.

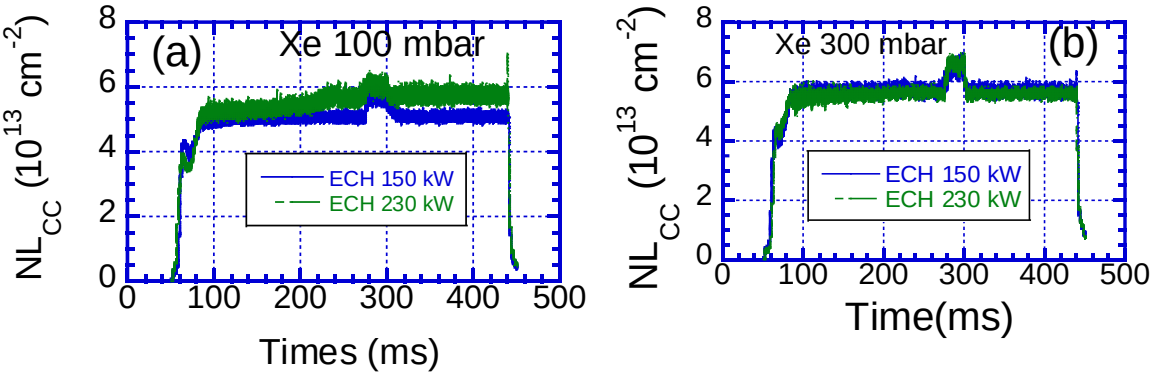

Fig. 3.21 Time behavior of NL_{CC} in the central-cell during (a) Xe 100 mbar and (b) Xe 300 mbar injection into the D-module.

The time behavior of ion flux during ECH injection period for Ar, Kr and Xe seeding is plotted in Fig 3.22. The ion flux shows a clear dependence on the gas species during ECH injection period. The increase ratio of ion flux during ECH injection period is also plotted in Fig. 3.23. The highest enhancement in the ion flux has been recognized during Xe seeding, which indicates the ionization effect of Xe neutral particle.

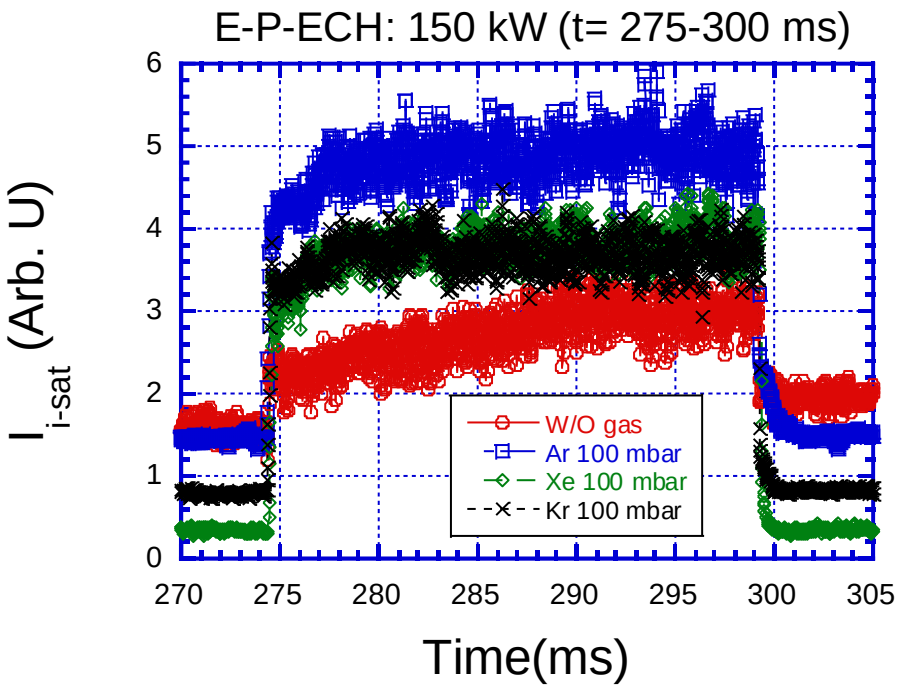

Fig. 3.22. Time behavior of ion flux during Ar, Kr and Xe injection.

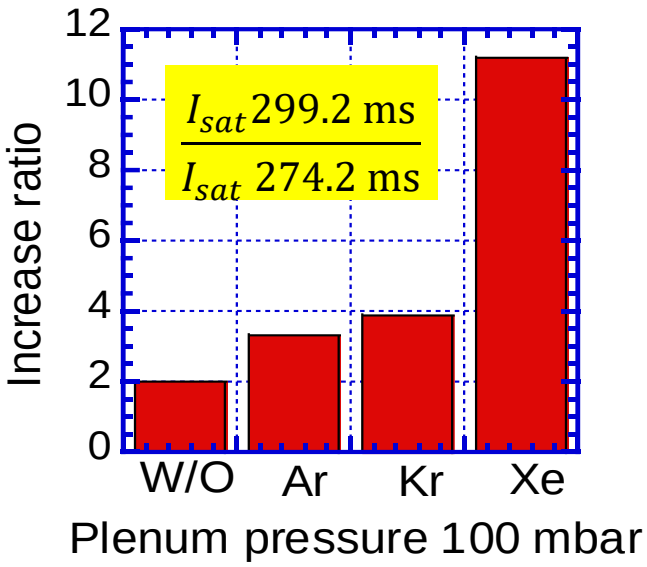

Fig. 3.23. Increase ratio in the ion flux measured in the corner of the target due to the application of ECH 150 kW at the east plug/barrier-cell.

The spectrometer data is shown in Fig. 3.24. The measuring position (Z~ 1073.5 cm) of the spectrometer (USB2000+) in the D-module is shown in Fig 2.5. As shown in Fig 3.24, The Xe II emission increases during ECH injection (time 275-300 ms, power: 150 kW), which indicates that ionization of Xe neutral particles enhances for ECH injection. On the other hand, a slight increase in the Ar ion components has been observed for Ar seeding. Kr ion component has been measured between Ar and Xe. These results indicate that a short pulse of ECH injection can break the plasma

detachment state.

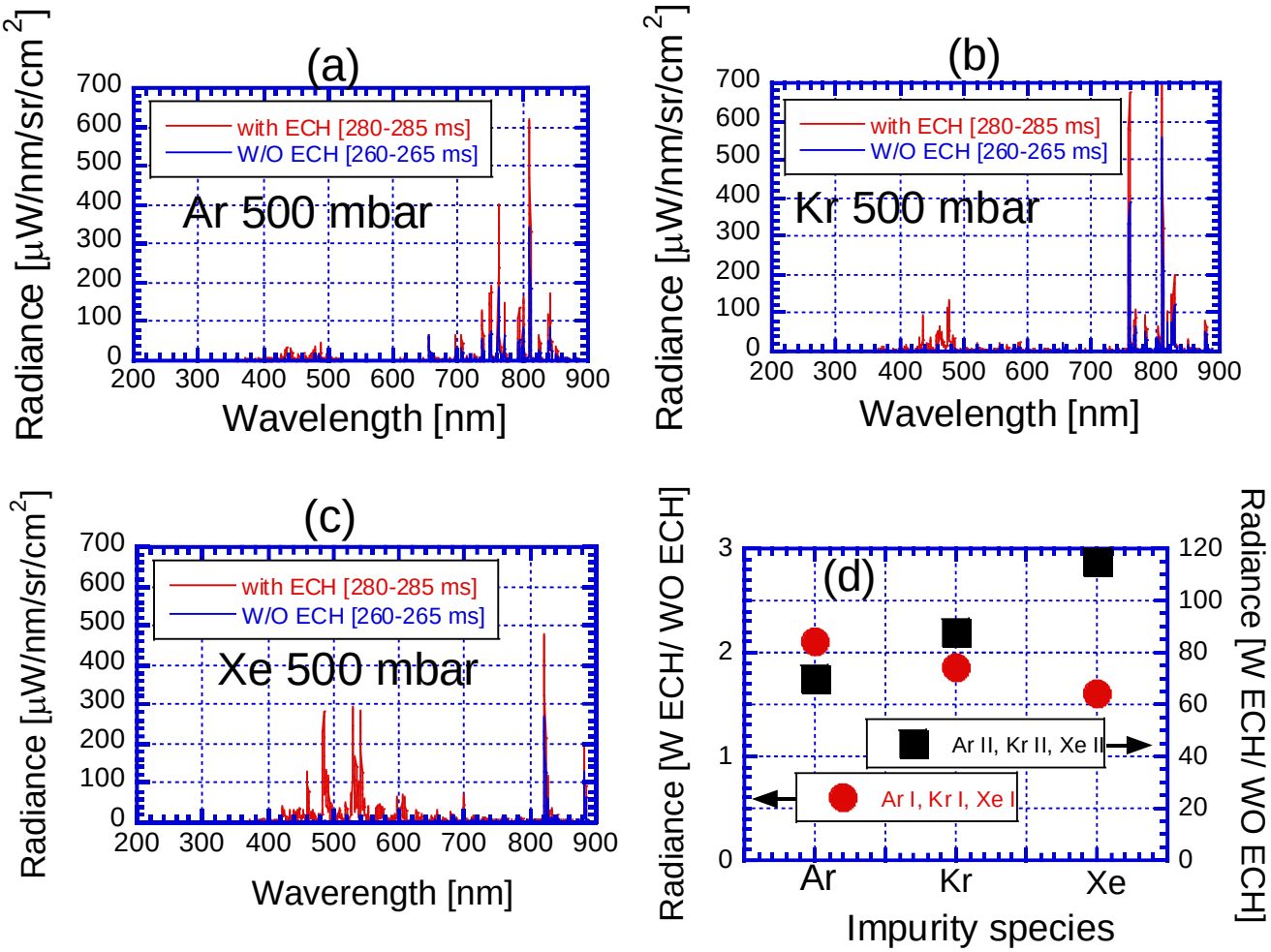

Fig. 3.24 Radiative power measured in the D-module (Z =1073.5 cm) during (a) Ar (b) Kr and (c) Xe injection (d) ratio of radiance between With ECH and Without ECH.

3.1.3 Discussion

In this study, the effects of three radiator gases (Ar, Kr, Xe) on the plasma detachment has been investigated based on the Langmuir probes and calorimeters measurements. It is found that Xe is the most efficient gas than that of Ar and Kr for generating the detached plasma. The distribution of heat flux in the $\pm$Y directions in case of Ar and Kr injection is slightly steeper than that of Xe injection. A remarkable reduction in the ion flux has been observed for Xe injection. The dependence of plasma parameters as a function of the three gas species is shown in Figs. 3.25-3.27. As shown in Fig 3.26 (b), a remarkable increase in the electron density is shown for Xe seeding at the plenum pressure of 100 mbar compared with the Ar and Kr injection, which indicates the ionization effects of Xe. Therefore, T_e reduces to 1.94 eV in case of plenum pressure of Xe 100 mbar injection as shown in

Fig 3.26 (a). On the other hand, reduction of T_e for Ar and Kr 100 mbar injection is 3.41 eV and 2.66 eV, respectively. At present, we do not have any diagnostic tools to measure the ion temperature. The heat flux relies on both the electron and ion temperature. Since the ion temperature is significantly higher than that of the electron temperature, the ion temperature is the main contributors in the heat flux. Hence, reduction in the heat flux strongly indicates the reduction in the ion temperature. The time behavior of the ion flux is plotted in Fig. 3.25. Without impurity injection, the ion flux slightly increases with time. However, a slight reduction in the ion flux is observed at plenum pressure of 100 mbar Ar injection, which indicates radiation cooling effect of Ar particles. In contrast to this, for Xe injection, the ion flux reduces drastically, which indicates stronger radiation cooling effect of the Xe particles. Reduction in the ion flux for Xe 100 injection is much higher than that of the Ar and Kr seeding. These outcomes indicate that Xe is the most effective for generating detached plasma than that of Ar and Kr.

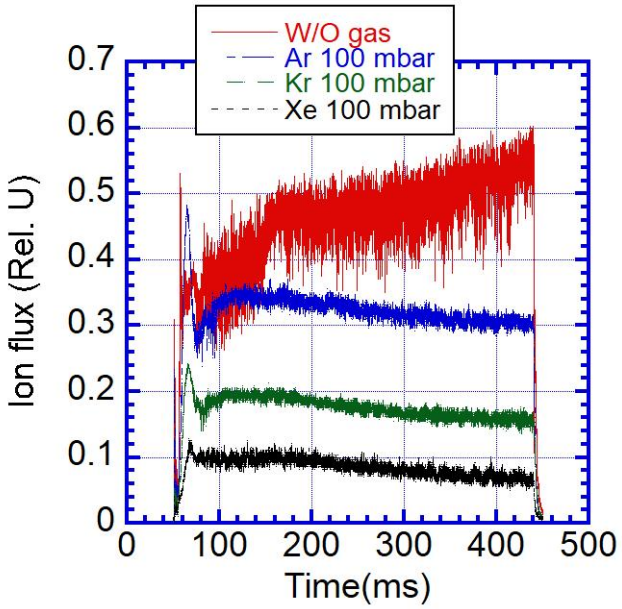

Fig. 3.25 Time behavior of ion flux measured in the corner of the V-shaped target.

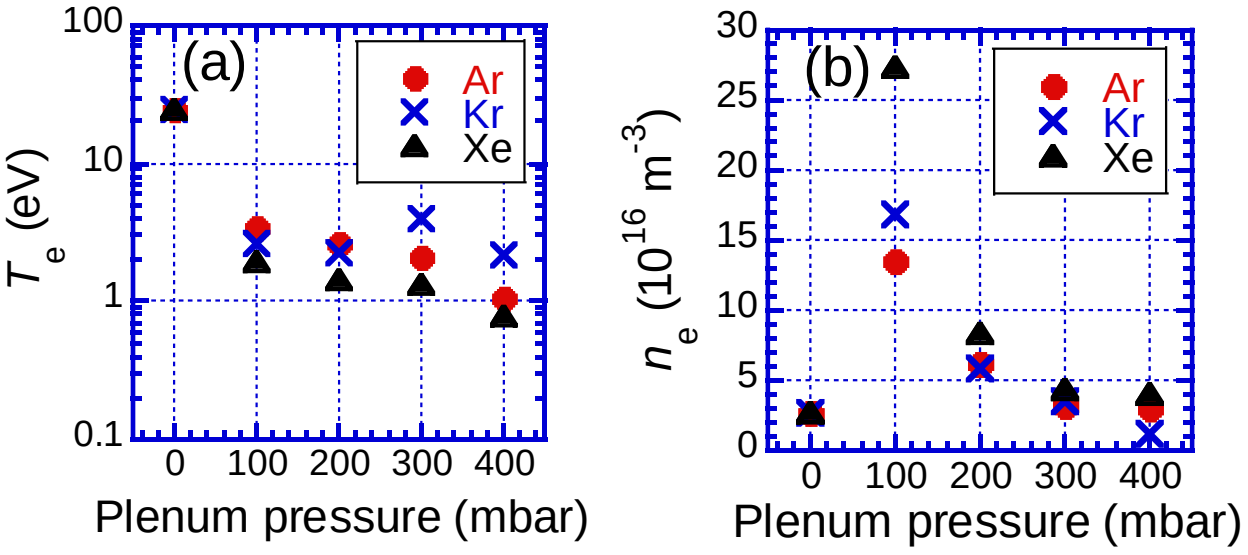

Fig. 3.26 Dependence of (a) T_e and (b) n_e as a function of gas plenum pressure.

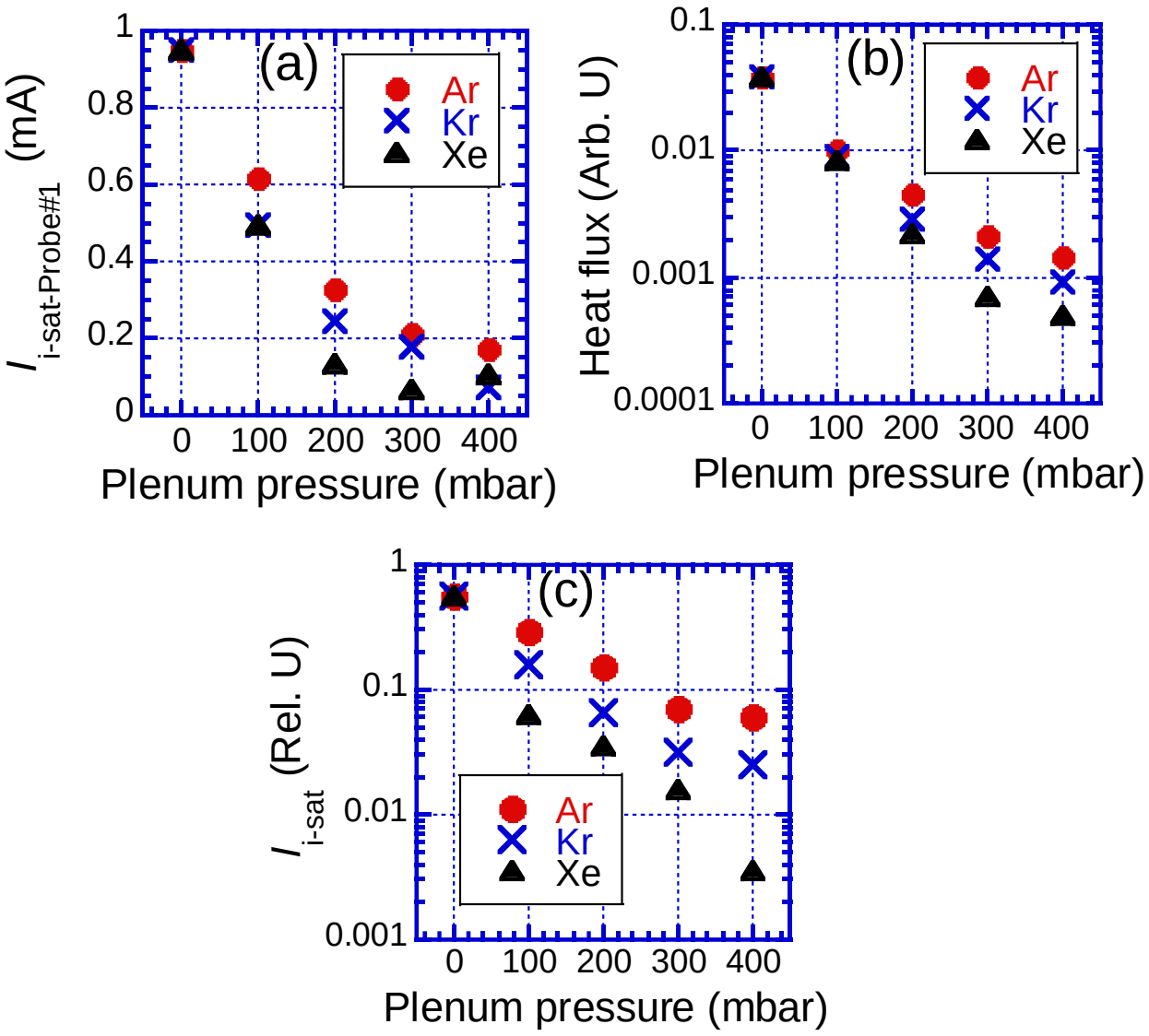

Fig. 3.27 Dependence of (a) Ion flux measured by probe#1 (b) heat flux and (c) ion flux measured in the corner of the V-shape target.

Plasmas energy can be reduced by the ionization, radiative power loss and Charge-exchange (CX) loss, etc. The radiative power loss and ionization loss might be the dominant energy loss channel for electrons. On the other hand, the CX loss is the dominant energy loss channel for ion. The plasma detachment state can be obtained through MAR and EIR. The ionization potential of Xe is lower than that of Ar and Kr while Kr ionization is placed between Ar and Xe. Hence, Xe can be easily ionized comparing to Kr and Ar. Therefore, electron density increases but electron energy reduces due to the ionization. Ionization begins to reduce according to the reduction of electron temperature, which induces a decrease in the electron density at lower electron temperature. The radiative power loss of Xe is also higher than that of the Kr and Ar. It is speculated that the momentum loss is also high for

Xe seeding. The radiative power loss was measured by the spectrometer (USB2000+) in the D-module of GAMMA 10/PDX as shown in Fig. 2.5. Figure 3.28 (a) shows the radiative power loss in case of 100 mbar impurity plenum pressure. The right-hand side figure represents radiative power loss for the impurity injection under the plenum pressure of 300 mbar. From the Fig. 3.28 (a), the Xe II lines emission are much higher than that of the Ar II and Kr II, which indicate the production of the Xe ion components is remarkably high. As a result, Xe injection increases the ionization as well as radiation loss and consequently reduces the plasma energy. The line emission from the ion components reduces significantly for the impurity injection under the plenum pressure of 300 mbar. In this case, the neutral line emission also reduces drastically. It is speculated that the ionization font changes with the changing impurity pressure in the D-module. The ionization-font may move to the upstream region with the increasing impurity neutral pressure. As a result, the line emission from both the ions and neutrals reduce remarkably for the impurity injection under the plenum pressure 300 mbar. From the above discussion, it is confirmed that the plasma near the corner of the target plate goes to the plasma detachment state. The dependence of the ionization and recombination font with the neutral pressure is a remaining task for the future work.

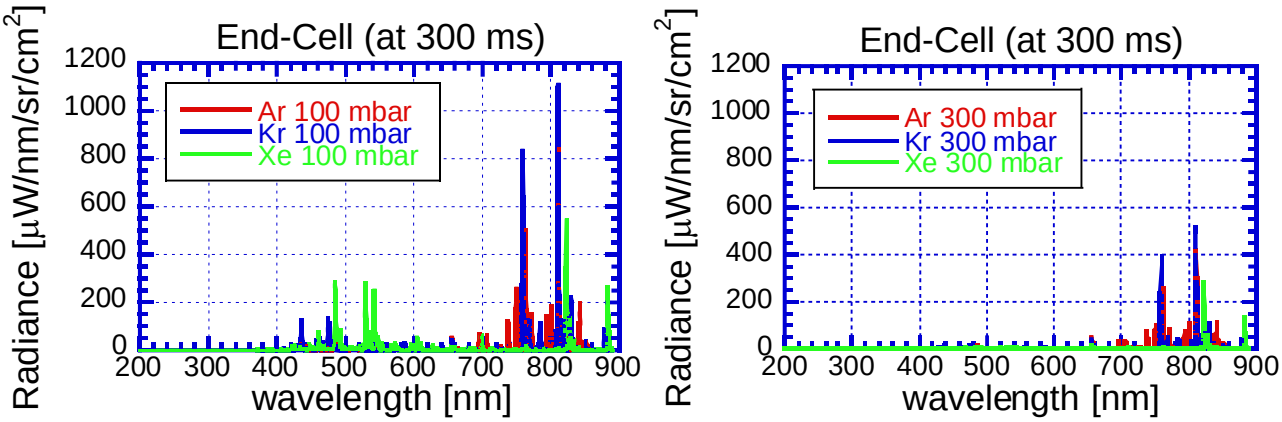

Fig. 3.28 Radiative power at 300 ms (a) 100 mbar injection (b) 300 mbar.

The typical 2D images of visible emission (without any filter: plasma and neutral) were captured by high-speed camera in front of the V-shape target are shown in Fig 3.29. The fast camera has been installed on the horizontal port aimed to capture the visible emission of plasma, neutral. The right-hand side images show the plasma emission for the Xe 100 mbar (top), Xe 200 mbar (middle) and Xe 300 mbar (bottom). These images were captured after ECH injection period, which indicates that the emission only for the ICRF plasmas. It is shown that the emission intensity reduces with the increasing Xe plenum pressure. For the higher Xe injection (300 mbar), the emission intensity is noticeably reduced near the corner of the V-shaped target, which strongly indicates the generation of a detached plasma by Xe seeding. However, during east p/b-ECH injection period (100 kW, 275-300

ms), the emission intensity increases significantly neat the corner of the target plate. In the low temperature plasma, neutral particles concentrate near the corner of the target. A short pulse of ECH abruptly changes the upstream plasma flux which strongly ionizes the neutral particles near the corner. As a result, a bright region appears near the corner.

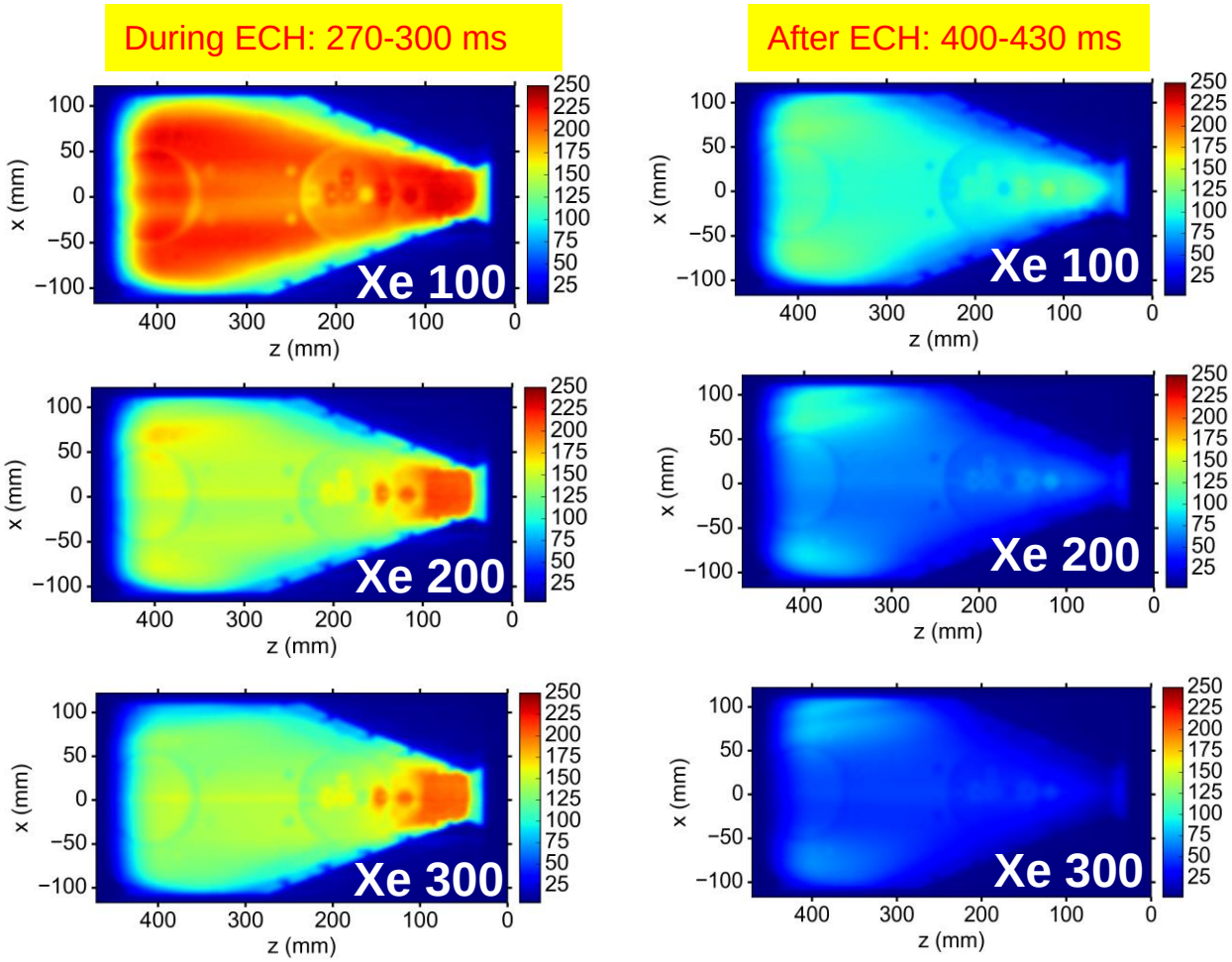

Fig. 3.29 2D image of visible emission from the plasma in front of the D-module was captured by the first camera (Without any filter and 20000 fps).

Chapter 4 Numerical Simulation Study

Numerical simulation study is a very useful tool to understand the detailed physical mechanism related to divertor plasma physics such as plasma detachment, impurity transport and energy loss processes. The main motivation to develop the LINDA (Linear Divertor Analysis with fluid model) code is to provide a platform to understand the physics of energy loss in the divertor region of the linear plasma devices. The LINDA code emphasizes on the simulation of divertor region to reveal the energy loss processes during neutral seeding in the divertor simulation experiments for the linear device GAMMA 10/PDX. The brief physical model of LINDA code is written as follows:

1) Simulation model and the fluid equations are similar with the B2 fluid code [35].
2) Standard finite volume method (implicit) [36] are applied to solve the basic equations.
3) 2D numerical grids have been generated under the axial symmetry.

In this chapter, section 4.1 describes physical model of the LINDA code. Section 4.2 describes simulation results and discussion.

4.1 Simulation model

4.1.1 Mesh structure

The numerical mesh is designed in the LINDA code based on the magnetic field configuration of GAMMA10/PDX by applying similar technique as the B2 code. Figure 4.1 (a) and (b) show the schematic view of the linear fusion device GAMMA 10/PDX and the mesh structure of the simulation region, respectively. In the LINDA code, the numerical mesh is designed under the assumption of the axial symmetry and 2D model in the x and y directions. The parallel and radial direction to the magnetic field is represented by the x and y direction. The plasma parameters have been considered to be uniform in the θ direction. The LINDA code can simulate plasma behavior in the axial direction from 7.50 m to 10.705 m while 0.0 m to 0.15 m in the perpendicular direction. As plotted in Fig.4.1 (b), a tungsten target plate is designed at the end of the mesh. Neutral particles have been injected from the mesh end and allow to flow toward the upstream region. On the contrary, hydrogen plasmas flow out plug/barrier-region to the end-cell. In the LINDA code, the neutral species (impurity and hydrogen) have been injected along the axial-direction by using the one-dimensional fluid equations.

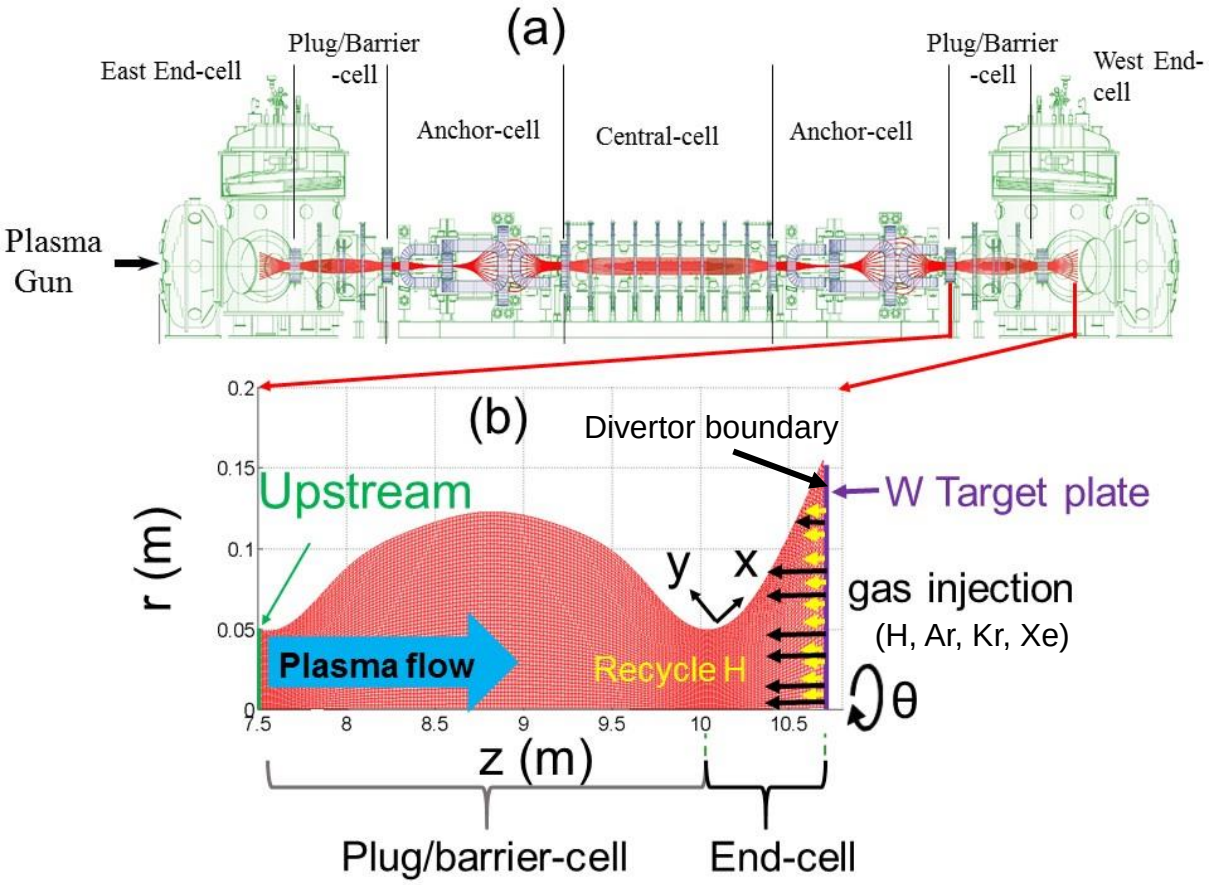

Fig. 4. 1. Schematic view of the (a) linear devices GAMMA 10/PDX and, (b) mesh of the simulation space.

4.1.2 Fluid equations

The multi-fluid code LINDA (Linear Divertor Analysis with fluid model) is written according to the fluid equations [35]: continuity equation (to solve the plasma density), momentum equation (to solve the parallel velocity), ion energy balance equation (the ion temperature) and electron energy-balance equation (the electron temperature). The diffusion equation is used to calculate perpendicular velocity. The effects of drifts have ignored in the LINDA code.

The main assumptions of the code are as follow:

(1) Quasineutral and ambipolar flow is considered.

(2) Ion velocity in diamagnetic direction has been neglected.

(3) Radial transport is anomalous while classical transport is used in the parallel direction.

(4) Simplified viscosity tensor is considered.

(5) Only the momentum balance equation has been solved for the ion species.

The fluid equations have been discretized and numerically solved in the similar fashion with the B2 code [35]. The convergence of the fluid equations has been checked by observing the residual error of the fluid equations. The residual error of the equations has been observed nearly 10^{-7}. The lower value of the residual error implies that the code has been properly converged.

The fluid equations of the code are written below:

Continuity equation of ion species α is:

$$\frac{\partial n_\alpha}{\partial t} + \frac{1}{\sqrt{g}}\frac{\partial}{\partial x}\left(\frac{\sqrt{g}}{h_x} n_\alpha u_\alpha\right) + \frac{1}{\sqrt{g}}\frac{\partial}{\partial y}\left(\frac{\sqrt{g}}{h_y} n_\alpha v_\alpha\right) = S_n^\alpha. \tag{4.1}$$

Continuity equation has been solved only for the ion species while the electron density (n_e) has been assumed to satisfy the relation $n_e = \Sigma$ (i = 1, ... , Nα) $Z_\alpha \times n_\alpha$, where n_α is the ion density for the charge state of Zα, Nα is the number of charge state. The ion density is written by the formula,

$n_i = \Sigma$ (i = 1, ... , Nα) n_α.

In the present numerical simulation, the inertia term for the electron momentum balance equation has been considered to be zero. Therefore, the resultant electron momentum balance equation together with the assumption of quasi-neutrality has been considered to ignore the Lorentz force terms and the Coulomb collision terms in the ion momentum equation and consequently, only the ion momentum equation has been solved in the LINDA code.

Momentum balance equation of ion species α is:

$$\begin{aligned}&\frac{\partial}{\partial t}\left(m_\alpha n_\alpha u_{||\alpha}\right) + \frac{1}{\sqrt{g}}\frac{\partial}{\partial x}\left(\frac{\sqrt{g}}{h_x} m_\alpha n_\alpha u_\alpha u_{||\alpha} - \eta_x^\alpha \frac{\sqrt{g}}{h_x^2}\frac{\partial u_{||\alpha}}{\partial x}\right) + \frac{1}{\sqrt{g}}\frac{\partial}{\partial y}\left(\frac{\sqrt{g}}{h_y} m_\alpha n_\alpha v_\alpha u_{||\alpha} - \eta_y^\alpha \frac{\sqrt{g}}{h_y^2}\frac{\partial u_{||\alpha}}{\partial y}\right) = \\ &\frac{1}{h_x}\frac{B_\theta}{B}\left[-\frac{\partial p_\alpha}{\partial x} - \frac{Z_\alpha n_\alpha}{n_e}\frac{\partial p_e}{\partial x} + c_e\left(\frac{Z_\alpha}{Z_{eff}} - 1\right) Z_\alpha n_e \frac{\partial T_e}{\partial x} + c_i\left(\frac{Z_\alpha}{Z_{eff}} - 1\right) Z_\alpha n_\alpha \frac{\partial T_i}{\partial x}\right] + \sum_{\beta=1}^{N} F_{\alpha\beta} + S_{mu||}^\alpha.\end{aligned} \tag{4.2}$$

On the right-hand side, the 1st and the 2nd terms express the pressure gradient force. The 3rd and the 4th part correspond to the thermal force for electron and ion, respectively. The 5th term is the friction force. The friction force plays a key role to transport impurity in the plasma upstream direction. The last term on the right-hand side of equation (4.2) is the source and sink terms for the plasma.

Diffusion approximation of species α in the radial direction is:

$$v_\alpha = -\frac{1}{h_y} D_n^\alpha \frac{\partial}{\partial y}(\ln n_\alpha). \tag{4.3}$$

The ion energy balance equation:

$$\begin{aligned}&\frac{\partial}{\partial t}\left(\frac{3}{2} n_i T_i + \sum_\alpha \frac{1}{2}\rho_\alpha u_{||\alpha}^2\right) + \frac{1}{\sqrt{g}}\frac{\partial}{\partial x}\left[\frac{\sqrt{g}}{h_x}\left(\sum_\alpha \frac{5}{2} n_\alpha u_\alpha T_i + \sum_\alpha \frac{1}{2} m_\alpha n_\alpha u_\alpha u_{||\alpha}^2\right) - \frac{\sqrt{g}}{h_x^2}\left(\kappa_x^i \frac{\partial T_i}{\partial x} + \right.\right. \\ &\left.\left.\sum_\alpha \frac{1}{2}\eta_x^\alpha \frac{\partial u_{||\alpha}^2}{\partial x}\right)\right] + \frac{1}{\sqrt{g}}\frac{\partial}{\partial y}\left[\frac{\sqrt{g}}{h_y}\left(\sum_\alpha \frac{5}{2} n_\alpha v_\alpha T_i + \sum_\alpha \frac{1}{2} m_\alpha n_\alpha v_\alpha u_{||\alpha}^2\right) - \frac{\sqrt{g}}{h_y^2}\left(\kappa_y^i \frac{\partial T_i}{\partial y} + \sum_\alpha \frac{1}{2}\eta_y^\alpha \frac{\partial u_{||\alpha}^2}{\partial y}\right)\right] = \\ &-\frac{u_e}{h_x}\frac{\partial p_e}{\partial x} - \frac{v_e}{h_y}\frac{\partial p_e}{\partial y} + k(T_e - T_i) + S_E^i + \sum_{\alpha\beta} F_{\alpha\beta}\left(u_{||b} - u_{||a}\right).\end{aligned} \tag{4.4}$$

The electron energy balance equation:

$$\frac{\partial}{\partial t}\left(\frac{3}{2}n_eT_e\right)+\frac{1}{\sqrt{g}}\frac{\partial}{\partial x}\left(\frac{\sqrt{g}}{h_x}\frac{5}{2}n_eu_eT_e-\kappa_x^e\frac{\sqrt{g}}{h_x^2}\frac{\partial T_e}{\partial x}\right)+\frac{1}{\sqrt{g}}\frac{\partial}{\partial y}\left(\frac{\sqrt{g}}{h_y}\frac{5}{2}n_ev_eT_e-\kappa_y^e\frac{\sqrt{g}}{h_y^2}\frac{\partial T_e}{\partial y}\right)=\frac{u_e}{h_x}\frac{\partial p_e}{\partial x}+$$
$$\frac{v_e}{h_y}\frac{\partial p_e}{\partial y}-k(T_e-T_i)+S_E^e+k_z(T_e-T_z). \tag{4.5}$$

On the right-hand side, the 1st and the 2nd term are the pressure gradient force. The 3rd and the 4th term correspond to the energy exchange between electron-ion, and electron-neutral, respectively. The last term represents source and sink terms for the electron.

The following notification are used in the above equations:

n_e and n_i represent the electron and ion density, g, h_x and h_y represent the metrics terms, v_e is the velocity of electron, m_α and Z_α are the mass and charge number of species α, T_e and T_i represent the temperature of electron and ion, P_e is the pressure of electron, u is the flow velocity, B and B_θ are the magnetic induction and the component of magnetic field, $F_{\alpha\beta}$ is the friction force between species α and β, Z_{eff} is the effective charge, η and κ represent the viscosity coefficient and thermal conductivity, c_e and c_i are the coefficients of thermal force, D_n^α is the Bohm diffusion constant.

S_n^α, $S_{mu||}^\alpha$, S_E^e , S_E^I represent the volume source of particles, parallel momentum, electron and ion energy due to interactions of plasma with the neutral particles. In the LINDA code, the interactions between charged and neutral particles for ions and electron are include in the source terms of the equations. The source and sink terms of the LINDA code are written below,

$$S_n = n_0n_e<\sigma v>_{ionz.}-n_en_i<\sigma v>_{rec.}+n_en_z<\sigma v>_{ioni-z.}-n_en_{imp}<\sigma v>_{z-rec.}, \tag{4.6}$$

$$S_{mu_\parallel}=-n_0n_i<\sigma v>_{CX}m_i(u_i-u_n)-n_en_i<\sigma v>_{rec.}m_iu_i\ , \tag{4.7}$$

$$S_E^i=n_0n_eE_n<\sigma v>_{ionz.}-n_nn_i<\sigma v>_{CX}\left(\frac{1}{2}m_iu^2+T_i-E_n\right)-n_en_i<\sigma v>_{rec}\left(T_i+\frac{1}{2}m_iu_i^2\right), \tag{4.8}$$

$$S_E^e=-n_0n_e<\sigma v>_{ionz}\ \delta_e-n_en_i<\sigma v>_{rec.}T_e-n_en_zL_z-n_en_{imp}<\sigma v>_{z-rec.}T_e, \tag{4.9}$$

where, δ_e (25 eV) represents the loss of electron energy during ionization, L_z is the radiative cooling rate, $E_n = \frac{1}{2}mu_n^2$ is the neutral energy, n_{imp} is the impurity ion density, n_0 and n_z are the hydrogen and impurity neutral density, respectively.

Electron velocities, density and pressure are defined as,

$$n_e=\sum_\alpha Z_\alpha n_\alpha\ ,\ \ u_e=\frac{1}{n_e}\sum_\alpha Z_\alpha n_\alpha u_\alpha\ ,\ \ v_e=\frac{1}{n_e}\sum_\alpha Z_\alpha n_\alpha v_\alpha,\ \ p_e=n_eT_e. \tag{4.10}$$

The definition of effective charge state is:

$$Z_{eff} = \frac{\sum_\alpha Z_\alpha^2 n_\alpha}{\sum_\alpha Z_\alpha n_\alpha}. \tag{4.11}$$

Table 4.1. Atomic processes are included in the code [51-53]

Gas	Ionization	Recombination	CX	Radiation loss
Hydrogen (H)	$H^+ + e \rightarrow H^+ + e + e$	$H^+ + e \rightarrow H$	$H^+ + H \rightarrow H + H^+$	
Impurities (Ar, Kr, Xe, Ne, N)	$Z^+ + e \rightarrow Z^+ + e + e$	$Z^+ + e \rightarrow Z$		$Z^* + e \rightarrow Z + e + h\nu$

4.1.3 Transport coefficient

The classical transport coefficients have been considered for the parallel direction [77] while the anomalous transport coefficients have been used in the radial direction.

Classical thermal conductivity coefficient of electron:

$$\kappa_{||}^e = 3.488 \times 10^{-4} \frac{n_e T_e}{m_e} \frac{T_e^{\frac{3}{2}}}{Z_{eff}\left(\frac{n_e}{10^{20}}\right) \ln\Lambda}. \tag{4.12}$$

Classical thermal conductivity coefficient of ion:

$$\kappa_{||}^i = 3.9 \frac{12\pi\sqrt{\pi}\epsilon_0^2}{e^4} \sum_\alpha \frac{Z_\alpha^{-2} n_\alpha}{\sum_\beta \left(Z_\beta^2 n_\beta \sqrt{\frac{2m_\alpha m_\beta}{m_\alpha + m_\beta}} \right)} \frac{T_i^{\frac{5}{2}}}{\ln \Lambda}. \tag{4.13}$$

The parallel viscosity coefficient:

$$\eta_{||} = 0.96 \frac{12\pi\sqrt{\pi}\epsilon_0^2}{e^4} \frac{Z_\alpha^{-2} n_\alpha}{\sum_\beta \left(n_\beta Z_\beta^2 \sqrt{\frac{2}{m_\alpha + m_\beta}} \right)} \frac{T_i^{\frac{5}{2}}}{\ln \Lambda}. \tag{4.14}$$

Energy equipartition coefficient between ion and electron:

$$k = \frac{3}{2} \frac{e^4 \sqrt{m_e}}{3\sqrt{2\pi}\pi\varepsilon_0^2} \left(\frac{Z_\alpha^2 n_\alpha}{m_\alpha} \right) \frac{n_e \ln\Lambda}{T_e^{\frac{3}{2}}}. \tag{4.15}$$

Energy relaxation coefficient between impurity and electron:

$$k_z = \frac{3}{2} \frac{e^4 \sqrt{m_e}}{3\sqrt{2\pi}\pi\varepsilon_0^2} \left(\frac{n_{\text{imp}}}{m_{Ar}} \right) \frac{n_e \ln\Lambda}{T_e^{\frac{3}{2}}}. \tag{4.16}$$

The coulomb logarithm:

$$ln\,\Lambda = 15.2 - 0.5\,ln\frac{n_e}{10^{20}} + \ln\frac{T_e}{1000}. \tag{4.17}$$

The flux limit for the electron thermal conductivity and parallel viscosity coefficients:

$$\kappa^e_{||lim} = \kappa^e_{||SH}\left[1 + \left|\frac{q_{SH}}{q_{FL}}\right|\right]^{-1}, \quad \eta^\alpha_{||lim} = \eta^\alpha_{||}\left[1 + \left|\frac{\eta^\alpha_{||}\frac{\partial u_{||\alpha}}{\partial x}}{\mu p_\alpha}\right|\right]^{-1}, \tag{4.18}$$

where, $\kappa^e_{||SH}$ is the classical Spitzer-Harm coefficient. μ is a constant factor coefficient.
The diffusion coefficient in the radial direction:

$$D_\perp = \frac{1}{16}\frac{T_e}{eB}. \tag{4.19}$$

These radial transport coefficients:

$$\kappa^i_\perp = 0.2 \times n_i, \quad \kappa^e_\perp = 4.0 \times n_e, \quad \eta_\perp = 0.2 \times m_i \times n_i. \tag{4.20}$$

4.1.4 Boundary Conditions

The fixed boundary (Dirichlet condition) condition have been applied at the upstream region.
Upstream boundary:

Ion density
$$n_i = n_{i0}\left\{\frac{r_0(0)}{r_0(z)}\right\}^2 e^{-\frac{1}{2}\left\{\frac{r(z)}{r_0(z)}\right\}^2}, \tag{4.21}$$

Ion temperature
$$T_i = T_{i0} \times e^{-\frac{1}{2}\left\{\frac{r(z)}{r_0(z)}\right\}^2}, \tag{4.22}$$

Electron temperate
$$T_e = T_{e0} \times e^{-\frac{1}{2}\left\{\frac{r(z)}{r_0(z)}\right\}^2}, \tag{4.23}$$

Ion parallel velocity
$$u_{i\|} = \sqrt{\frac{n_eT_e + n_iT_i + n_zT_z + n_{imp}T_z}{m_in_i + m_zn_{imp}}}. \tag{4.24}$$

where r_0 indicates half maximum full-width of physical quantities, *r*(z) is spatial position of physical quantities and *z* is z axial position.

The divertor boundary conditions (for the ion and electron) have been applied on the target plate.

Divertor boundary conditions for the electron and ion energy equations:

$$Q_i = \alpha_i n_i u_i T_i \; and \; Q_e = \alpha_e n_e u_e T_e. \tag{4.25}$$

$$u_{||\alpha} \geq \sqrt{\frac{T_{i\alpha} + T_e}{m_\alpha}}. \tag{4.26}$$

The ion heat transfer coefficient:

$$\alpha_i = \frac{2T_i}{T_e}. \tag{4.27}$$

The electron heat transfer coefficient:

$$\alpha_e = \frac{2}{1-\gamma_e} - \frac{1}{2} ln\left\{\left(2\pi \frac{m_e}{m_i}\right)\left(1 + \frac{T_i}{T_e}\right)(1-\gamma_e)^{-2}\right\}. \quad (4.28)$$

At the z-axial direction, the boundary condition is defined as symmetry boundary.

z-axial boundary:

$$\frac{\partial n_\alpha}{\partial x} = \frac{\partial T_e}{\partial x} = \frac{\partial T_i}{\partial x} = \frac{\partial u_{||\alpha}}{\partial x} = 0. \quad (4.29)$$

Here, the Neuman condition is applied on the periphery region.

The periphery boundary condition:

$$\frac{\partial T_{i\alpha}}{\partial x} = \frac{\partial T_e}{\partial x} = \frac{\partial n_{i\alpha}}{\partial x} = const. \quad (4.30)$$

4.1.5 Neutral Model

The definition of neutral particles is given by solving a 1D continuity equation.

The recycling hydrogen neutral flux on the target plate is written as follows:

$$n_{0,target} \cdot u_n = R_N \cdot \Gamma_{i,target}. \quad (4.31)$$

The recycling hydrogen neutral velocity (u_n) is written as follows:

$$u_n = \sqrt{\frac{\frac{R_E}{R_N} \times T_{i,target}}{m}}, \quad (4.32)$$

where, R_E and R_N correspond to the energy and particle reflection coefficient, respectively [14, 54], $\Gamma_{i,target}$ represents the hydrogen ion flux on the target plate, u_n is the recycling hydrogen neutral velocity, $n_{0,target}$ is the recycling hydrogen neutral density on the target plate, m corresponds to the hydrogen atom mass and $T_{i,target}$ represents the ion temperature on the target plate.

The definition of hydrogen neutral particle is calculated by solving the 1-D continuity equation. Continuity equation of the hydrogen neutral particle is written as follows:

$$\frac{d(n_0 n_u)}{dz} = -n_0 n_e < \sigma v >. \quad (4.33)$$

The gas puffing hydrogen neutral density is assumed to be uniform in the end-cell and reduces exponentially in the plug/barrier region. The hydrogen neutral density profile in the plug/barrier region is adjusted according the GAMMA 10/PDX data. The following equations are used in the study to define hydrogen neutral profile along the z-axis:

$$n_0(z) = n_{0,target} \exp(-\int_{z_1}^{z_2} \left(\frac{1}{\lambda_1}\right) dz + n_{OH}, \quad (4.34)$$

$$n_0(z) = n_{0,target} \exp(-\int_{z_1}^{z_2} \left(\frac{1}{\lambda_1}\right) dz + n_{0H} \exp(-\int_{z_1}^{z_3} \left(\frac{1}{A \times \lambda_2}\right) dz). \quad (4.35)$$

Equations (4.34) and (4.35) represent hydrogen neutral density in the end-cell and the plug/barrier

region, respectively. The 1st part of the equations corresponds to the recycling hydrogen neutral while the 2nd term corresponds to the gas puffing hydrogen neutral atoms.

Continuity equation of the impurity neutral particle is represented by the following equation,

$$\frac{\mathrm{d}(n_z n_z)}{dz} = -n_z n_e < \sigma v >. \tag{4.36}$$

As for the impurity neutral, the following equations are used to describe impurity density distribution on the z-axis:

$$n_z(z) = n_{z-injection}, \tag{4.37}$$

$$n_z(z) = n_{z-injection} \exp(-\int_{z_1}^{z_3} \left(\frac{1}{B \times l_d}\right) dz. \tag{4.38}$$

Equations (4.37) and (4.38) represent impurity neutral density in the end-cell and the plug/barrier region, respectively.

The impurity and hydrogen neutral models neutral have been calculated iteratively together with the fluid equations in the self-consistence manner. The following notations are used in the above neutral equations: n_0 : hydrogen neutral density, n_z : impurity neutral density, $z_1 = 7.5$, $z_2 = 10.705$, $z_3 = 10.045$, u_z: impurity neutral velocity, $\lambda_1 = \frac{u_n}{n_e<\sigma v>_{ionz.} + n_e<\sigma v>_{CX:H+:H0}}$, $\lambda_2 = \frac{u_{n2}}{n_e<\sigma v>_{ionz.} + n_e<\sigma v>_{CX:H+:H0}}$, $l_d = \frac{u_z}{n_e<\sigma v>_{ioni-z.}}$, $<\sigma v>_{ionz.}$ corresponds to the ionization reaction rate coefficient of hydrogen, $< \sigma v >_{CX:H+:H0}$ represents the proton and hydrogen neutral charge exchange reaction rate coefficient, $< \sigma v >_{ioni.-z}$ corresponds to the impurity neutral ionization reaction rate coefficient, *i* and *j* is the number of mesh in the *x* and *y* axis, respectively, n_{0H} is the injected hydrogen neutral density, and $n_{z-injection}$ represents the impurity neutral density, $u_{n2} = \sqrt{\frac{3k}{m}}$ represents the hydrogen neutral velocity, $u_z = \sqrt{\frac{0.0259k}{m_z}}$ corresponds to the impurity neutral velocity, *m* is the mass of hydrogen, m_z is the mass of impurity, A and B are the multiplication factor to adjust the decay of the neutral particle to make it comparable with the GAMMA 10/PDX experimental data.

In GAMMA 10/PDX, the neutral particles (hydrogen and impurity) have been puffed into the D-module from the outside of GAMMA 10/PDX vacuum chamber and consequently, impurity neutrals and impurity ions temperature is assumed to be 0.0259 eV. In the LINDA code, it is considered that the puffed impurity neutral distributes uniformly in the end-region and reduces exponentially in the upstream region (7.5 m ≤ z ≤ 10.045 m). On the other hand, the definition of neutral particles in the radial direction is constant (uniform). The radial profile needs to be modified by solving the 2D neutral equations in the near future.

The distribution of the hydrogen neutral particles on the z-axis is shown in Fig.4.2 (a). Increase in the hydrogen neutral density near the target plate is observed in the figure because of the recycling hydrogen neutral flux. The recycling neutral density is high near the target plate and reduces

according to the mean free path. As for the impurity, the neutral density is almost uniform in the end-cell, which is consistence with the experimental results of GAMMA 10/PDX. In GAMMA 10/PDX, the D-module is located in the end-cell of GAMMA 10/PDX and the module is a closed rectangular box. Hence, uniform neutral density profile has been speculated in the D-module. Thus, a flat impurity neutral profile has been considered in the LINDA code. The impurities neutral density profile along the z axial direction is shown in Fig. 4.2 (b). There is no recycling neutral flux for the Ar neutral and consequently, the neutral density is shown to be uniform in the end-cell and reduces exponentially in the plug/barrier region. At present, there are no experimental data for the impurity neutral density in the plug/barrier region. However, it is speculated that the Ar neutral particles are ionized near the D-module and transport toward the upstream region as Ar ion or Ar neutral. The decay of Ar neutral towards the upstream region maybe around 3 orders of magnitude. However, it is our future plan to adjust the Ar neutral profile according to the typical experimental findings of GAMMA 10/PDX.

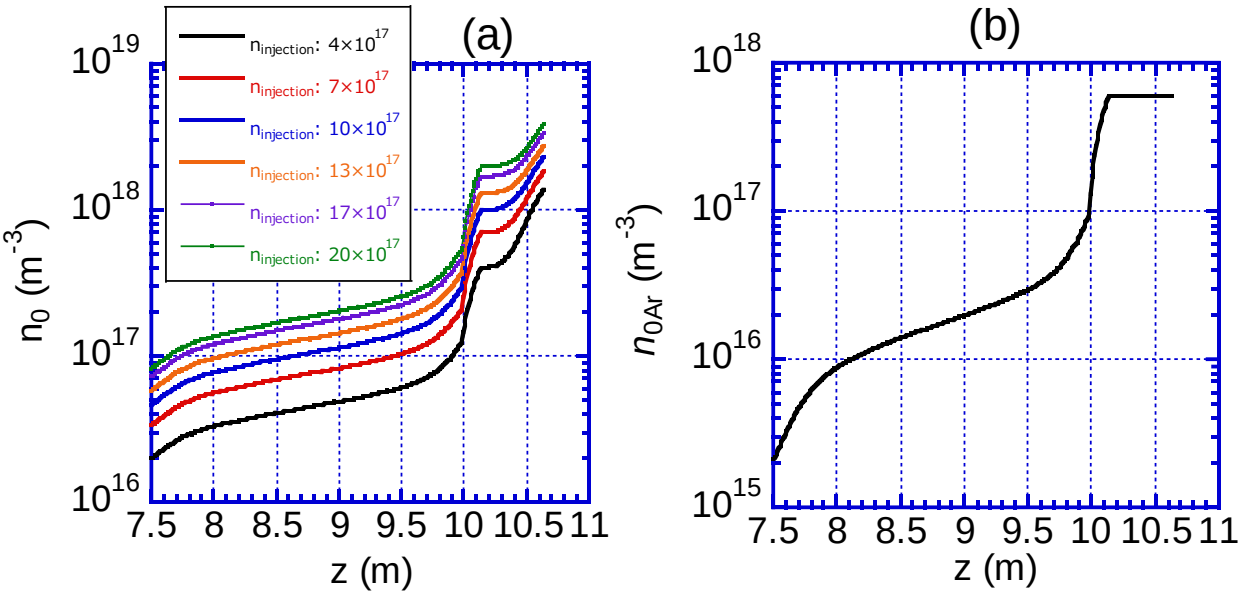

Fig. 4. 2. Distribution of neutral particles on z-axis (a) hydrogen (b) Ar

4.1.6 Calculation scheme to solve the equations and Residual error

The fluid equations have been discretized and numerically solved in similar fashion with the B2 code [35]. The finite-volume discretization technique is applied in the present code [36].

The conduction-convection equation has been written in conservation form as follows:

$$\nabla \cdot \mathrm{J} = \mathrm{S}. \qquad (4.39)$$

Where, $J = \rho \mathbf{u} \varphi - \Gamma \nabla \varphi$

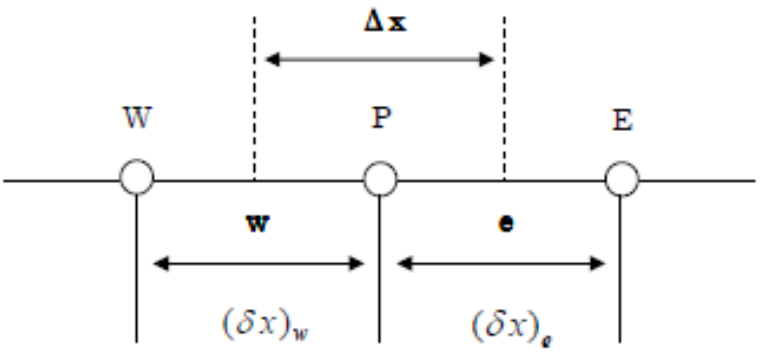

Fig. 4.3 Control volume scheme for the 1D calculation.

The calculation points are P and its right (E) and left (W) points. The value of physical quantity (φ) is taken at these three points. The region has been integrated by the finite volume method is highlighted by the dotted line in Fig 4.3. In the figure, e is the boundary on the right side and w is on the left side. The area between the two point's e and w is called the control volume.

Equation (4.39) can be integrated as follows:

$$\int_{\mathrm{v}} \nabla \cdot J = \int_{v} S\Delta V \, . \tag{4.40}$$

The equation can be written in Gaussian form as follows:

$$\int_{\mathrm{v}} J \cdot ds = J_e A_e - J_w A_w + \mathrm{J_n} A_n - J_s A_s. \tag{4.41}$$

Where, A is the mesh area.

For the 1D calculation,

$$(\rho u\phi)_{\mathrm{e}} A_e - (\rho u\phi)_{\mathrm{w}} A_w - \left\{ \left(\Gamma \frac{\delta\phi}{\delta x} \right)_e A_e - \left(\Gamma \frac{\delta\phi}{\delta x} \right)_w A_w \right\} = S\Delta V. \tag{4.42}$$

Where,

$$J_e = (\rho u\phi)_{\mathrm{e}} A_e - \left(\Gamma \frac{\delta\phi}{\delta x} \right)_e A_e \text{ and } J_w = (\rho u\phi)_{\mathrm{w}} A_w - \left(\Gamma \frac{\delta\phi}{\delta x} \right)_w A_w.$$

The J_e can be represented in terms of ϕ_p and ϕ_E by the following formula,

$$J_e = \alpha\phi_P - \beta\phi_E \, . \tag{4.43}$$

Here, the convection term F_{e} and the conduction term D_{e} can be written as follows:

$$F_{\mathrm{e}} = mn_e u_e \text{ and } D_{\mathrm{e}} = \frac{\Gamma_{\mathrm{e}}}{(\delta x)_e}. \tag{4.44}$$

The hybrid method has been used in the study to solve the fluid equations which is follows:

$$\alpha_e = \left[F_e, D_e + \frac{F_e}{2}, 0 \right], \beta = \left[-F_e, D_e - \frac{F_e}{2}, 0 \right]. \tag{4.45}$$

The more detailed explanation can be found in the references [35-36].

The discretization of the equation for each cells is written in the following matrix form:

$$Ax = b. \tag{4.46}$$

The following notifications are used:

A is the ($N_g \times N_g$) matrix, and x and b are the vector of N_g unknown values and the given N_g sources, respectively. In the 2D simulation, the number is $N_g = M \times N$, where M and N are the number of cells in each direction. More specifically, x is the unknown vector, whose elements correspond to the solution of the equation at each grid point in the control-volume. For instance, if we discretize the electron energy balance equation, each element of the vector x correspond to T_e at each spatial grid point.

The Stone's Strongly Implicit Procedure (SIP) has been used in the code to solve the fluid equations. The iterative processes are needed to obtain the solution of each equations, because the basic fluid equations are nonlinear equation for unknown variables.

The residual vector r in the i-th iteration process is defined as

$$\mathrm{r(i)} = \mathrm{A\,x(i)} - \mathrm{b}, \tag{4.47}$$

where x(i) is the numerical obtained in the i-th iteration process.

$$\mathrm{dr} = \mathrm{r(i+1)} - \mathrm{r(i)} = \mathrm{A}\big(\mathrm{x(i+1)} - \mathrm{x(i)}\big). \tag{4.48}$$

Therefore, the difference in the residual dr is getting smaller, when the solution of the equation is getting closer to the convergent solution, i.e.,

$$\mathrm{x(i+1)} \geq \mathrm{x(i)}. \tag{4.49}$$

The calculation results have been checked for validity and convergence. The residual error of plasma parameters has been used to check the convergence of the each equations. The definition of the residual error is written as follows:

$$\Delta\tilde{\varphi} = \frac{\sum_i \sqrt{(\varphi^1 - \varphi^0)^2}}{\sum_i \varphi}, \tag{4.50}$$

where,

φ	Physical amount	φ^0	Physical amount of previous calculation step
φ^1	New defined physical amount	$\sum_i$	The summation in all meshes

Figure 4.4.1 shows the variation of residual error for the fluid equations. The residual error for the parallel ion velocity is shown in Fig. 4.4.1. It is shown that the residual error reduces with the increasing number of iteration. The residual error for the velocity equation also shows a dependence on the H neutral density. However, the residual error reduces according to the increment of number

of iteration. The residual error has been measured nearly 10^{-6} for the velocity equation. As for the electron and ion energy equation, the residual error also reduces with the number of iteration. As the number of iteration is increased, the residual error is reduced. The residual error is measured about of 10^{-7} for the density, electron and ion energy equation. The lower value of residual error implies that the equation has been converged properly.

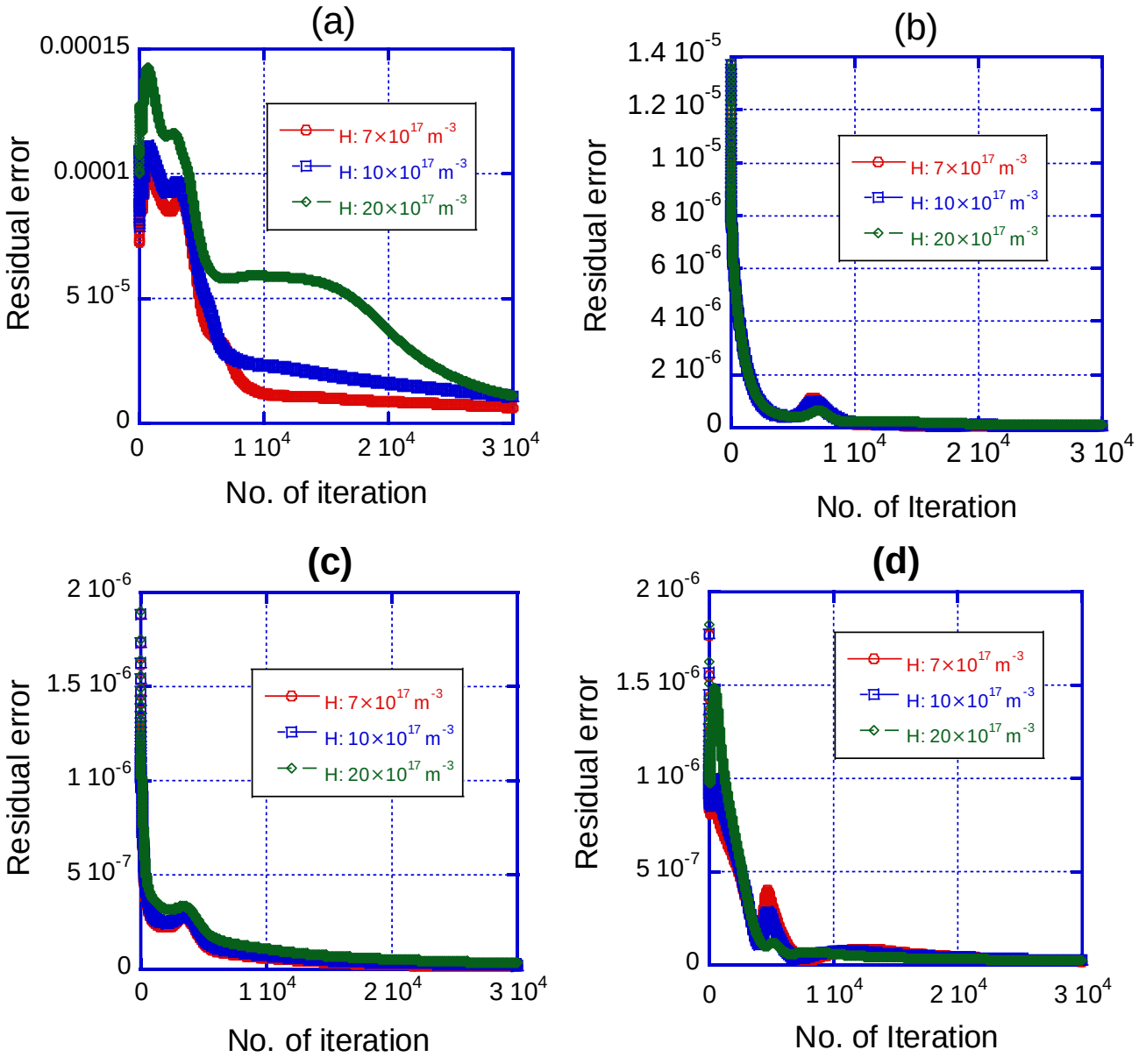

Fig. 4. 4.1 Residual error (a) velocity (b) density (c) electron temperature, and (d) ion temperature as a function of H neutral density.

The dependence of residual error against the Ar neutral density in the end-cell is plotted in Fig 4.4.2. It is shown that the residual error reduces with the increasing number of iteration. The residual error has been found nearly 10^{-6} for the velocity equation. As for the electron and ion energy equation, the residual error also reduces with the number of iteration. As the number of iteration is increased, the residual error is reduced. The residual error is found nearly of 10^{-7} for the density, electron and ion energy equation. The lower value of residual error implies that the equation has been converged properly.

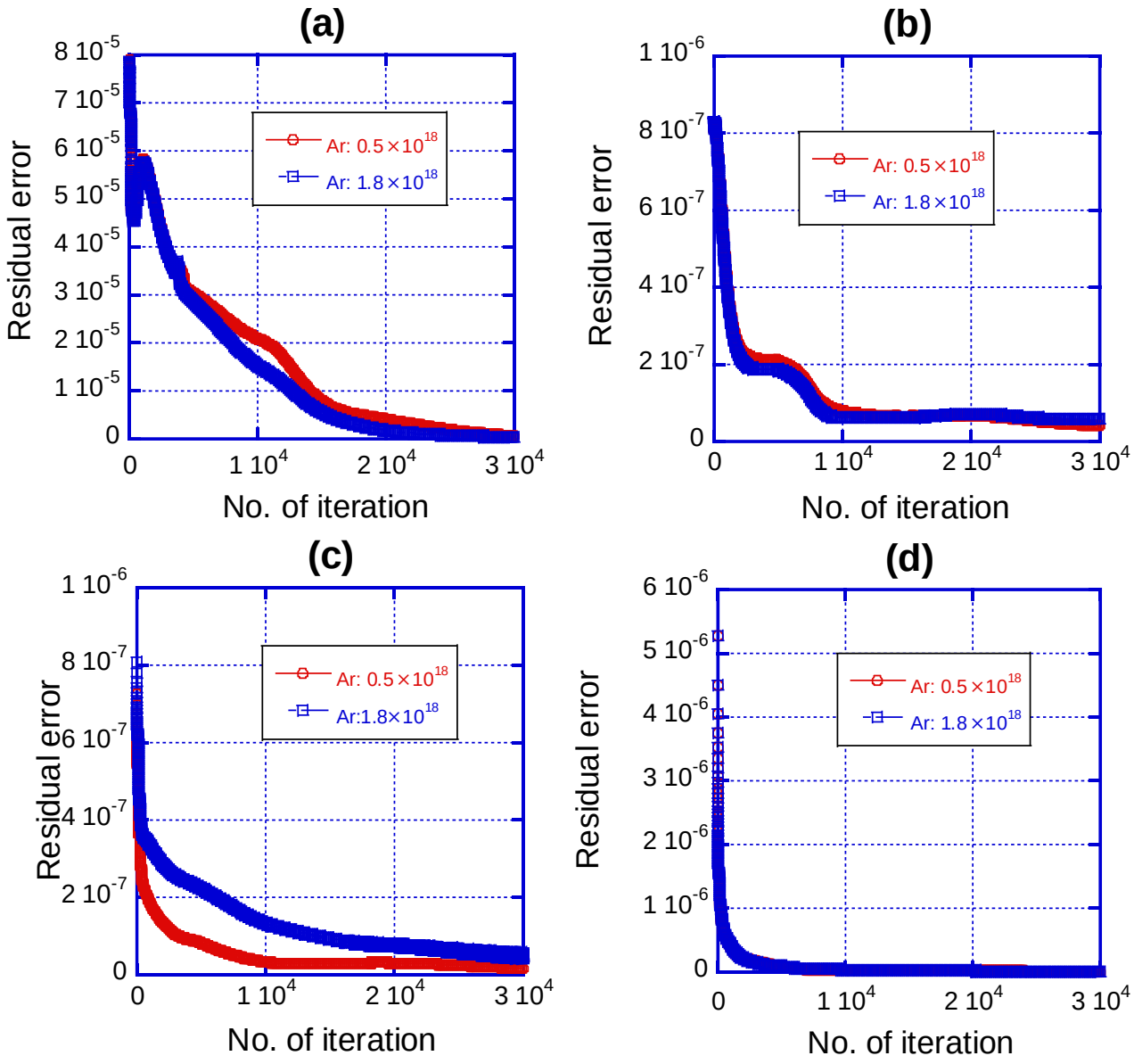

Fig. 4. 4.2 Residual error (a) velocity (b) density (c) electron temperature, and (d) ion temperature as a function of Ar neutral density.

4.2 Simulation results and discussion

4.2.1 Simulation results at the upstream density $n_{i0} = 5 \times 10^{18}\ \mathrm{m}^{-3}$

A. Simultaneous injection of Ar and H (Ar density is fixed while H density is varied.)

The radiator gas Ar has been injected into the background plasma in order to understand the radiation cooling effects of the Ar towards the formation of plasma detachment. In addition, the hydrogen neutral atom has also been injected to explore the atomic processes of H towards the plasma detachment. In the study, the injected Ar density has been fixed at $6 \times 10^{17}\mathrm{m}^{-3}$ while the injected hydrogen neutral atom density has been varied from 0.0 to $2.8 \times 10^{18}\mathrm{m}^{-3}$. The neutral models of the simulation condition are shown in Fig 4.2. The simulation results are summarized in Figs. 4.5 to 4.10. The 2-dimensional profiles of the electron temperature are plotted in Fig. 4.5. The z-axial profile of the electron temperature as a function of the injected hydrogen neutral density is shown in Fig 4.8 (a). It is shown that the electron temperature reduces near the target plate due to the Ar and H injection. Especially, the radiation cooling effects of the Ar neutral particles play a driving role in the electron temperature reduction. A slight reduction in the electron temperature is shown for without any gas puffing. The recycling hydrogen neutrals are included in the present study. Because of this, a slight reduction in the electron temperature is shown for without any gas injection condition. Furthermore, the reduction rate in the electron temperature has been enhanced when hydrogen gas is intentionally injected. For only H $4.0 \times 10^{17}\ \mathrm{m}^{-3}$ injection, the electron temperature near the target plate reduces to about 15 eV. On the other hand, a noticeable reduction in the electron temperature has been shown during Ar injection. For only Ar $6 \times 10^{17}\mathrm{m}^{-3}$ injection, the T_e on the target plate decreases to about 10 eV. Furthermore, the reduction rate has been increased in case of simultaneous injection of H and Ar. The electron temperature also reduces with the increasing H injection. Under the case of simultaneous seeding of Ar and H, the T_e on the target plate decreases to about 3 eV, which indicates the radiation cooling effects of Ar neutral particles and ionization effects of the hydrogen neutral particles. The dependence of the ion temperature on the hydrogen neutral density has also been investigated. The 2D profile and the z-axial profile of the ion temperature are shown in Fig 4.6 and Fig 4.8 (b), respectively. The ion temperature also reduces with the increasing H injection. For the strongest H injection case, the ion temperature reduces significantly. The parallel ion velocity has also been investigated in the study. The 2D profile of the ion velocity is shown in Fig 4.7. Hydrogen neutral seeding significantly reduces the hydrogen ion velocity, which indicates that the interaction between hydrogen neutral and hydrogen ion plays a key role to suppress the ion velocity. The dependence of hydrogen neutral density on the plasma parameters are shown in Fig 4.9.

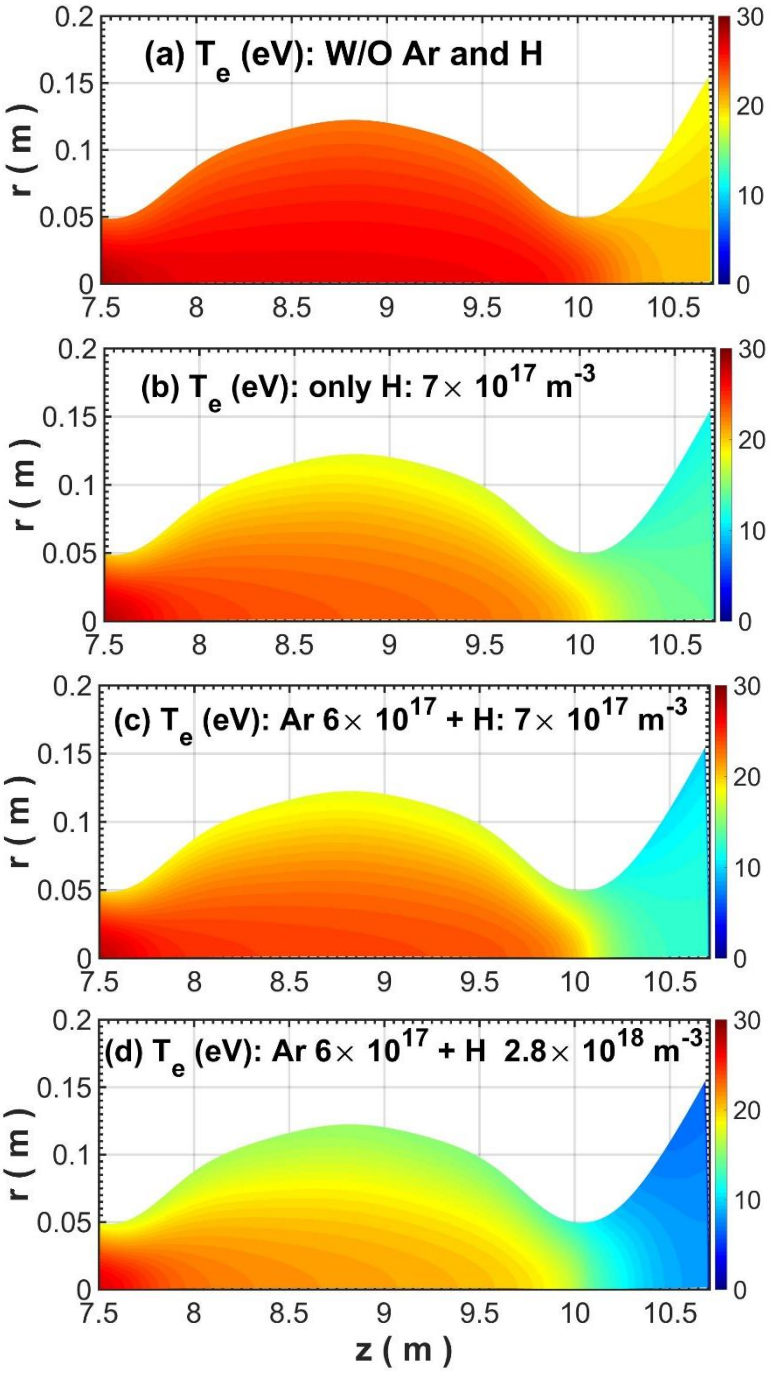

Fig. 4.5 2D profiles of the electron temperature for (a) W/O gas (b) H injection and (c) simultaneous injection of H $7 \times 10^{17}\mathrm{m}^{-3}$and Ar (d) simultaneous injection of H $2.8 \times 10^{18}\mathrm{m}^{-3}$and Ar.

The 2D profiles of the T_i are plotted in Fig. 4.6. The ion temperature reduces during H injection, which mainly comes from the CX loss between proton and hydrogen neutral. The ion temperature also reduces with the increasing H injection. Moreover, the ion temperature also reduces during simultaneous seeding of Ar and H. For the strongest H seeding, the ion temperature has reduced drastically. During the simultaneous injection of Ar and H, the T_i on the target plate decreases to

nearly 24 eV for the strongest H seeding.

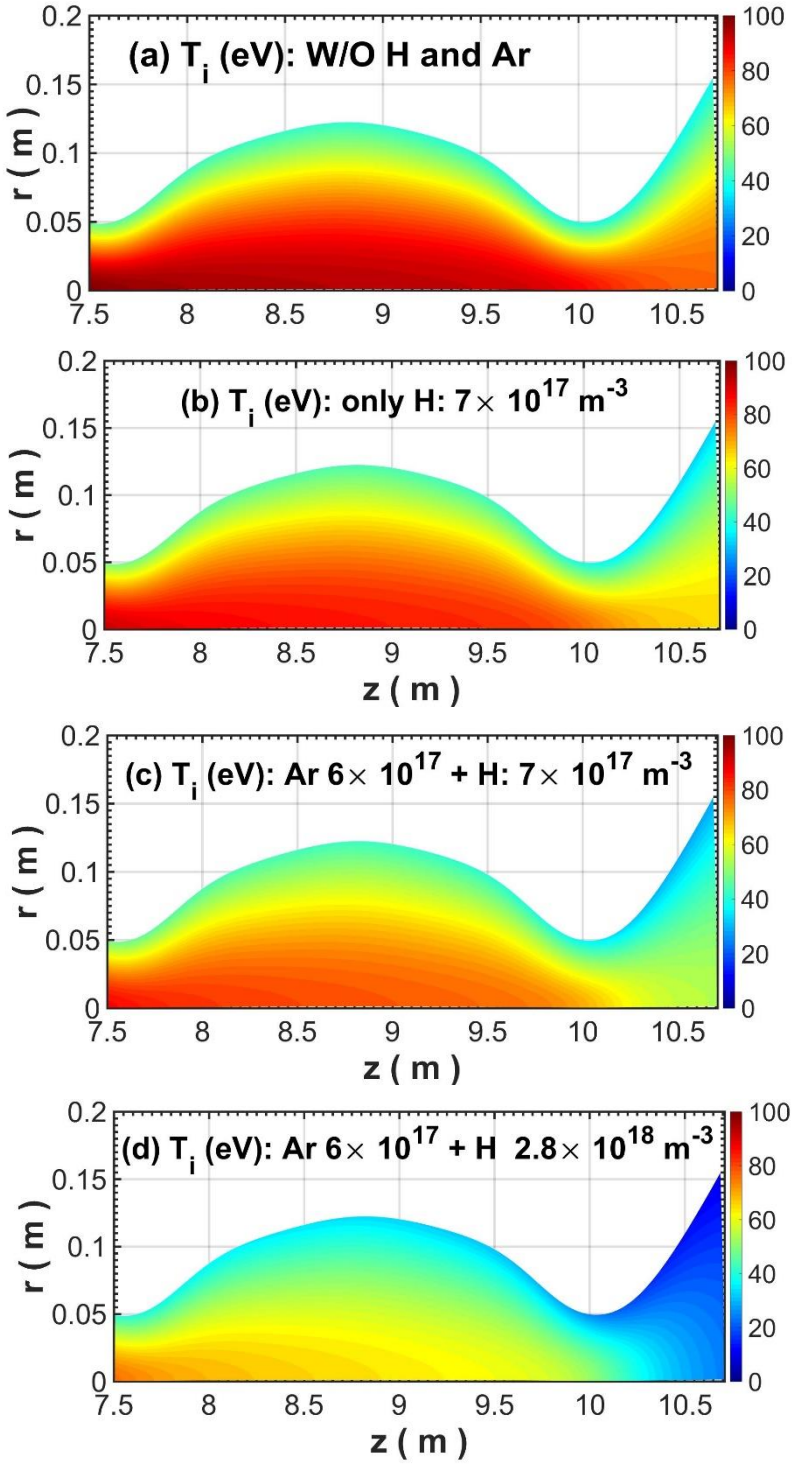

Fig. 4.6 2D profiles of the ion temperature for (a) W/O gas (b) only H injection and (c) simultaneous injection of H $7 \times 10^{17} \mathrm{m}^{-3}$ and Ar (d) simultaneous injection of H $2.8 \times 10^{18} \mathrm{m}^{-3}$ and Ar.

The 2D profiles of the parallel hydrogen ion velocity are shown in Fig 4.7. The ion velocity

increases toward the target plate for without any gas injection. In the present model, the Bohm condition on the target plate has been applied. Therefore, the velocity increases toward the target plate due to the boundary condition. Furthermore, the parallel ion velocity significantly reduces at the higher neutral H injection, which indicates that the interactions between the ion and the neutral particles significantly affects the parallel ion velocity.

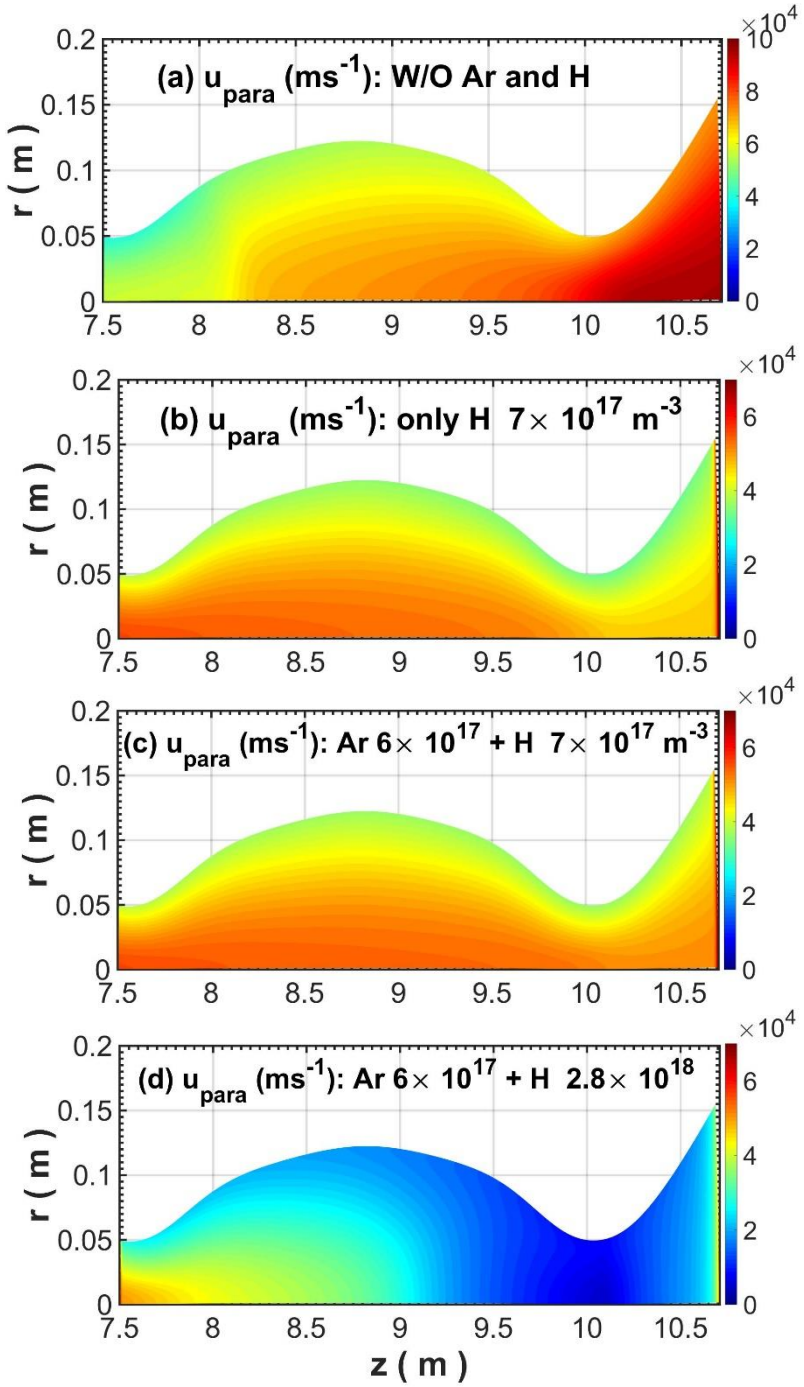

Fig. 4.7 2D profiles of the ion velocity for (a) W/O gas (b) only H injection and (c) simultaneous injection of H $7 \times 10^{17} \mathrm{m}^{-3}$and Ar (d) simultaneous injection of H $2.8 \times 10^{18} \mathrm{m}^{-3}$and Ar.

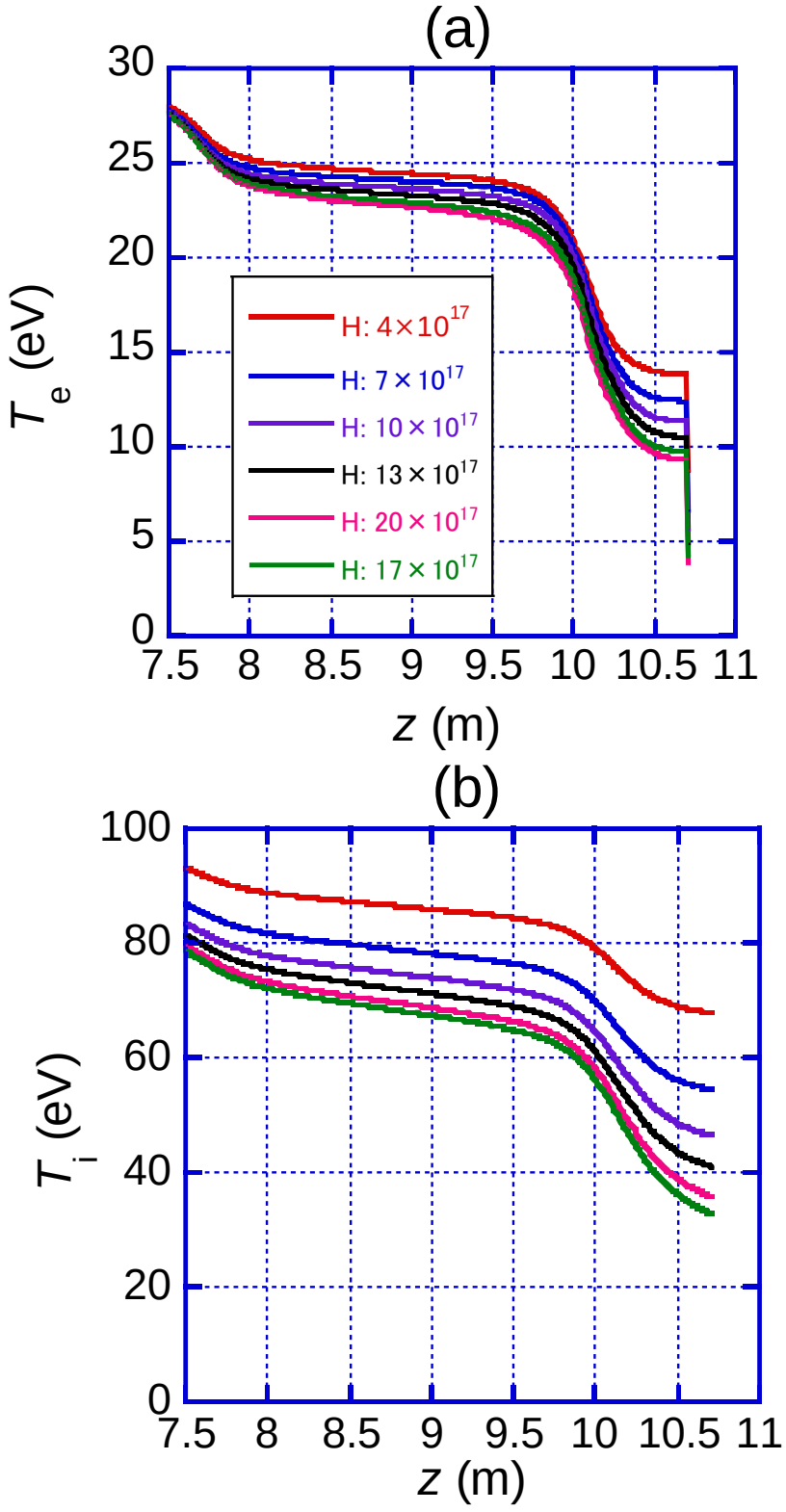

Fig. 4.8 z-axial profiles of the (a) electron and (b) ion temperature as a function of injected hydrogen neutral density.

The dependence of plasma parameters on the target plate (at r =0 cm) is plotted in Fig 4.9. The dependence of the electron temperature (T_e) on the target plate (at r =0 cm) as a function of the injected hydrogen neutral density is shown in Fig. 4.9 (a). The electron temperature on the target plate reduces as the increasing H injection. For the strongest H injection, the T_e on the target plate decreases to nearly 5 eV. A remarkable reduction in the T_e has been recognized for only Ar seeding. For only Ar $6 \times 10^{17} \mathrm{m}^{-3}$ seeding, the T_e reduces to nearly 10 eV. Furthermore, the T_e also reduces with the increasing H injection. It is shown that the reduction in the electron temperature for simultaneous seeding of H and Ar is higher than that of only H injection, which indicates the radiation cooling effects of Ar.

The dependence of ion temperature (T_i) on the target plate as a function of injected H neutral density is shown in Fig. 4.9 (b). The reduction rate of ion temperature is almost similar for only H injection and simultaneous injection of Ar and H. However, a slight influence of Ar seeding on the ion temperature has been observed, which comes from the energy exchange between electron and ions. Ar seeding reduces the electron temperature, which induces a reduction in the ion temperature. In the GAMMA 10/PDX, the density is low, therefore, the rate is small. As a result, a slight effect of Ar injection in the ion temperature has been shown in the lower H injection region.

The dependence of electron density (n_e) on the target plate on the injected H neutral density is shown in Fig. 4.9 (c). The electron density increases with the increasing H injection. It is shown that the electron density is high for simultaneous seeding of Ar and H comparing to the only H seeding, which indicates ionization effects of Ar neutral particles. During the simultaneous seeding of Ar and H, the electron density becomes saturated at the higher H injection. A tendency of so-called roll-over phenomena has been observed in the density at the higher H injection region. A clear roll-over phenomenon may be observed if the electron temperature is reduced below 1 eV. On the other hand, for only H injection, the electron density continues to increase with the increasing H injection.

Figure 4.9 (d) shows the dependence of particle flux (Γ_i) on the target plate as a function of the injected H neutral density. At the lower H gas injection region, the particle flux is slightly high for simultaneous injection of Ar and H compared with the only H seeding. However, the tendency has been changed according to the increasing H neutral density. During the simultaneous seeding of Ar and H, the particle flux becomes saturated at the higher H injection. On the other hand, for only H injection, the particle flux continues to increase with the increasing H injection.

Figure 4.9 (e) shows the variation of the heat flux as a function of the H neutral density. At the lower H injection region, the heat flux is slightly high during simultaneous injection Ar and H compared with the only H injection. Furthermore, a slight increase in the heat flux is shown at the lower neutral H injection. However, at the higher H injection, the heat flux starts to reduce. At the higher H neutral injection, the heat flux becomes low in case of simultaneous seeding Ar and H than that of only H injection. The heat flux strongly depends on the density, temperature and velocity. Although the temperature and velocity reduce with the increasing H neutral injection, but the electron density increases which affects the heat flux.

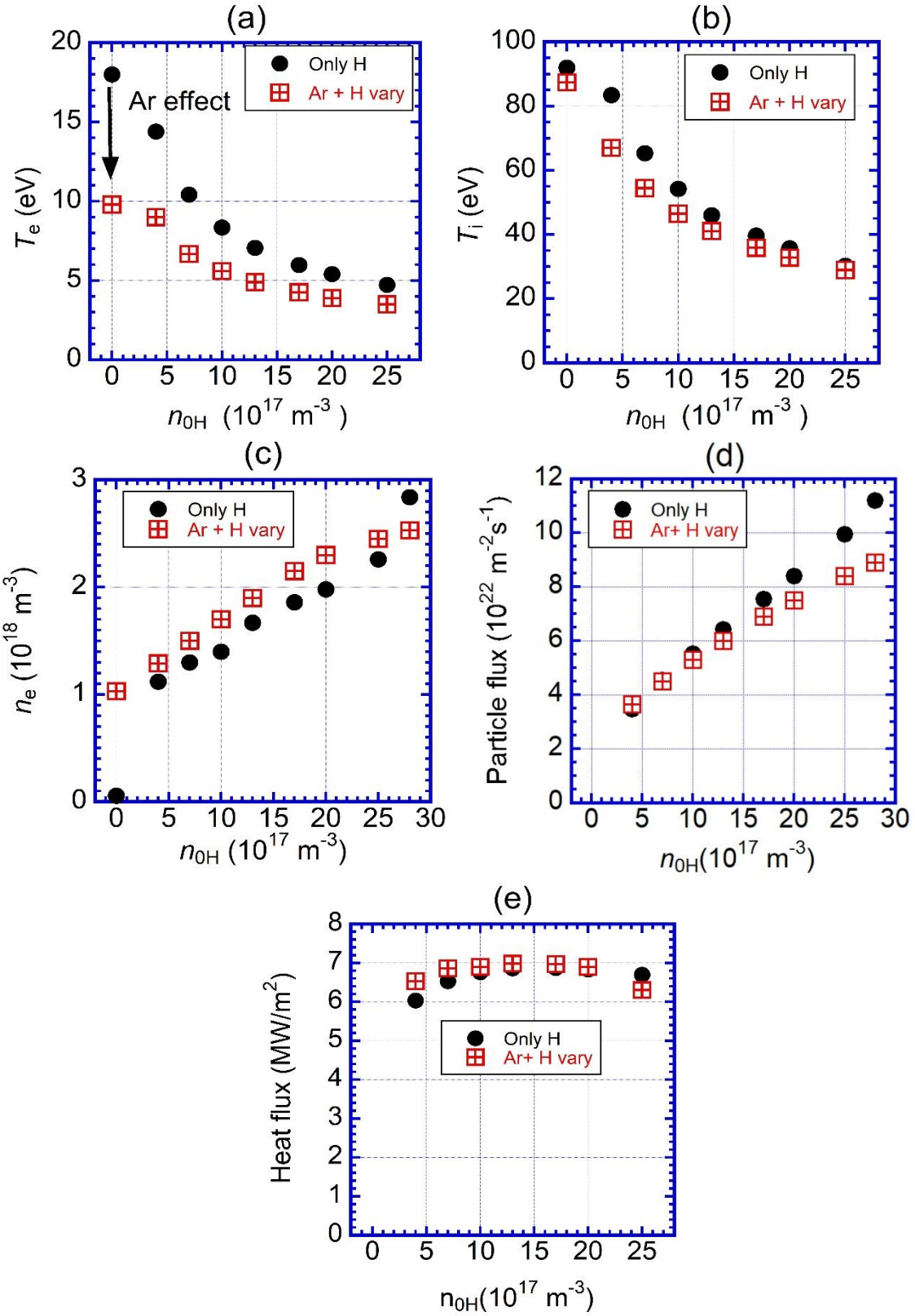

Fig. 4.9 Dependence of plasma parameters on the target plate (at r = 0 cm) (a) electron temperature (b) ion temperature (c) electron density and (d) particle flux (e) heat flux as a function of the injected H neutral density.

The energy loss processes have also been investigated to explore the physics of energy loss mechanism during neutral seeding. The dependence of the CX loss and recombination loss against the injected hydrogen neutral density is plotted in Fig. 4.10 (a). The CX loss increases significantly during H injection. As a result, the ion temperature significantly reduces via the CX loss. Furthermore, the CX loss increases with the increasing hydrogen injection. The CX reaction rate coefficient is an almost nearly flat profile in the temperature range from 10 eV to 100 eV. Therefore, the CX loss strongly depends on the ion temperature, proton, and hydrogen neutral density. Because of this, CX loss increases with the increasing neutral density, although the ion temperature is reduced with the increasing hydrogen neutral density.

The recombination loss is very small. However, the recombination loss increases as the electron temperature is decreased. The recombination processes become very active in the low temperature region ($T_e < 1$ eV). In this study, T_e reduces to about 3 eV. At such the high T_e range neutral ionization reaction rate is much higher than that of the recombination rate.

The power loss due to the ionization of hydrogen neutral particles increases with the increasing H neutral density. This power loss is slightly high for only H injection comparing to the simultaneous injection of Ar and H because the electron temperature is low during both the Ar and H seeding. As the electron temperature is reduced, the ionization rate coefficient is reduced, which affects the total ionization power loss.

The radiative power loss of Ar increases significantly during Ar injection. Since the electron density increases with the increasing H injection, the Ar radiation power loss slightly increases with the increasing H injection. However, a slight increase in the radiation power loss is shown.

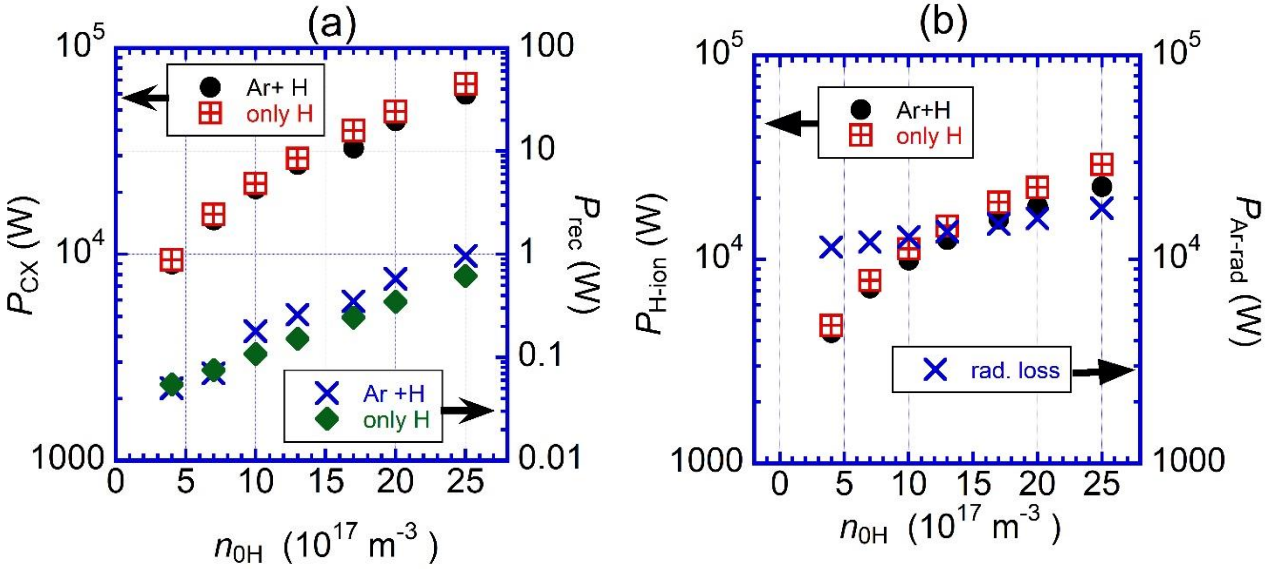

Fig. 4.10 Dependence of (a) CX loss and recombination loss, and (b) ionization loss and Ar radiative loss as a function of H neutral density.

B. Simultaneous injection of Ar and H (H density is fixed while Ar density is varied.)

The dependence of Ar neutral density on the plasma parameters has also been studied. Here, the injected hydrogen neutral density is fixed at $6 \times 10^{17} \mathrm{m}^{-3}$ while the injected Ar neutral density is varied from 4×10^{17} to $3.7 \times 10^{18} \mathrm{m}^{-3}$. The simulated results are shown in Figs. 4.11 to 4.16. The 2-D profiles of the electron temperature are shown in Fig 4.11. The electron temperature reduces near the target plate for only H injection. However, the electron temperature reduces significantly for Ar injection. For the strongest Ar injection, the electron temperature has been reduced drastically, which indicates radiation cooling effects of Ar particles. For the strongest Ar injection, the electron temperature has been remarkably reduced near the target plate. In this case, the electron temperature on the target plate reduces to about 3 eV.

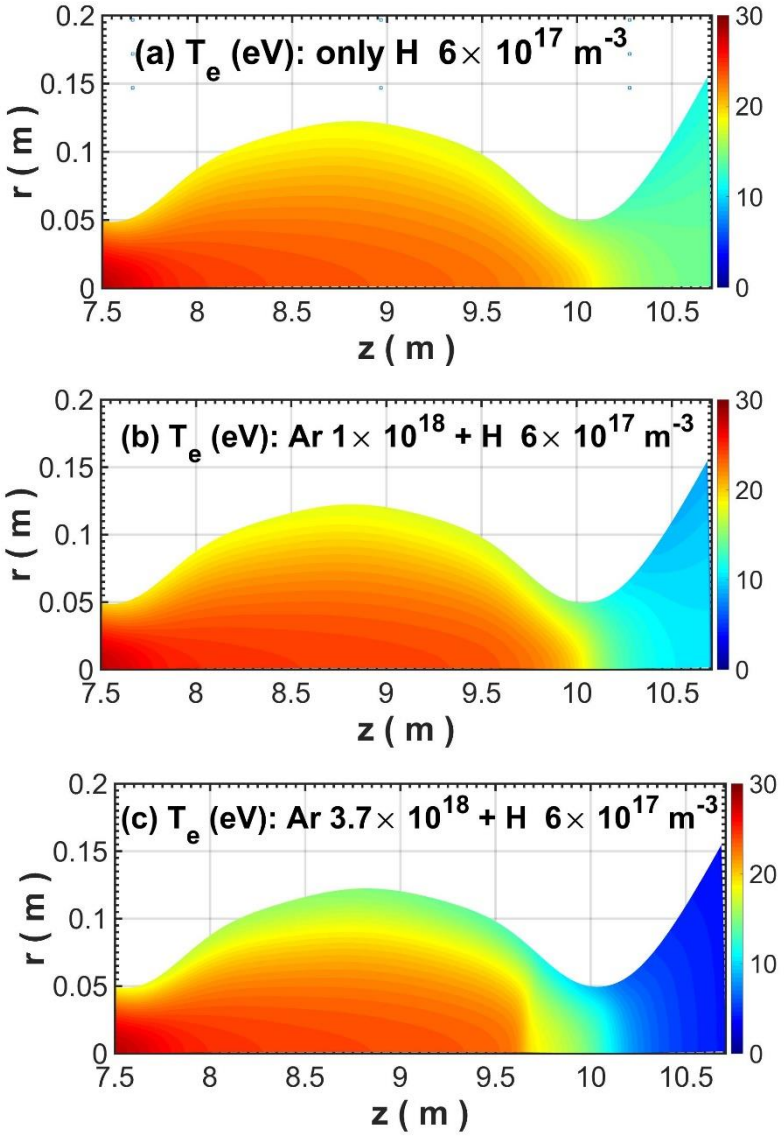

Fig. 4.11 2D profiles of the electron temperature for (a) only H injection and (b) simultaneous injection of H and Ar $6 \times 10^{17} \mathrm{m}^{-3}$ (c) simultaneous injection of H and Ar $3.7 \times 10^{18} \mathrm{m}^{-3}$.

The 2D profiles of ion temperature are shown in Fig 4.12. The ion temperature also reduces toward the target plate for only H injection. A slight reduction in the ion temperature is shown during Ar seeding. The dependence of the Ar density on the ion temperature has also been investigated. It is shown that Ar seeding into the plasma slightly affects the ion temperature. For the strongest Ar injection, the ion temperature near the target plate has been reduced. However, the reduction rate is much lower than that of the strongest H seeding.

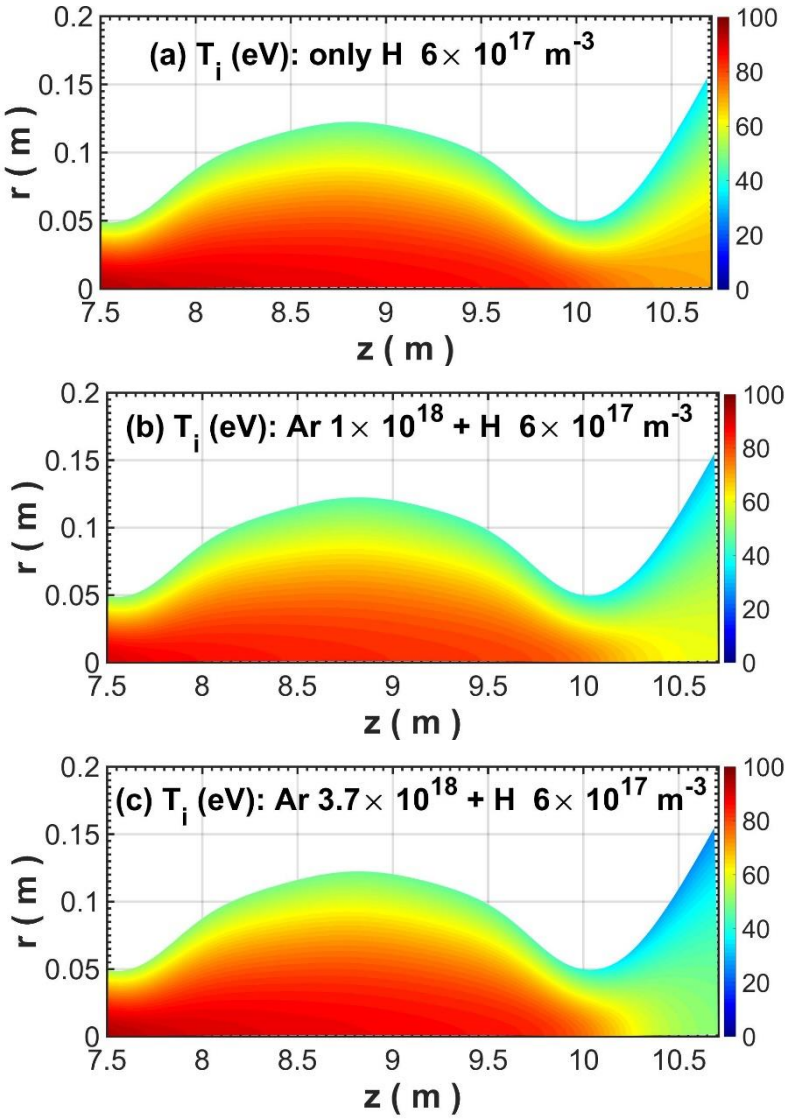

Fig. 4.12 2D profiles of the ion temperature for (a) only H injection and (b) simultaneous injection of H and Ar $6 \times 10^{17}\mathrm{m}^{-3}$ (c) simultaneous injection of H and Ar $3.7 \times 10^{18}\mathrm{m}^{-3}$.

The z-axial profiles of the electron and the ion temperature are shown in Fig 4.13. The electron temperature reduces significantly near the target plate with the increasing Ar injection, which indicates the radiation cooling effect of the Ar neutral particles. On the other hand, a clear dependence of the Ar neutral density on the ion temperature has not been observed. The ion temperature reduces slightly with the increasing Ar injection.

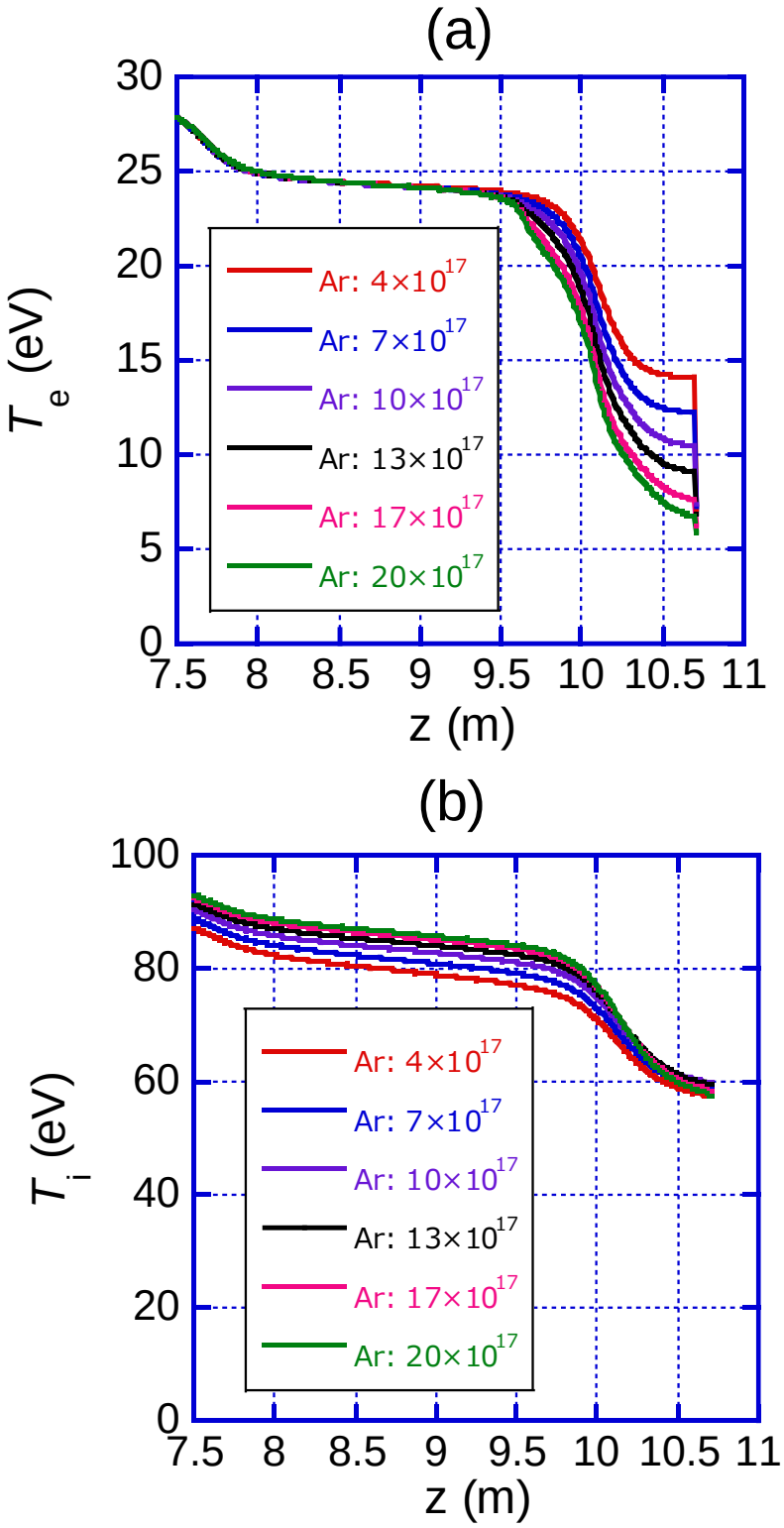

Fig. 4.13 z-axial profiles of the (a) electron and (b) ion temperature as a function of injected Ar neutral density.

The 2D profiles of the electron density are shown in Fig 4.14. Two peaks are shown in the density profile. These peaks are appeared in the profile due to the particle balance (flux tube conservation). The mesh area in these regions is smaller than that of the other region. As a result, the electron density increases in these regions due to the particle balance. In addition, a clear dependence of the injected Ar density on the density profile has been shown. The electron density increases according to the increasing Ar injection, which indicates ionization effects of the neutral particles. A clear roll-over phenomenon has not been observed yet in the density profile.

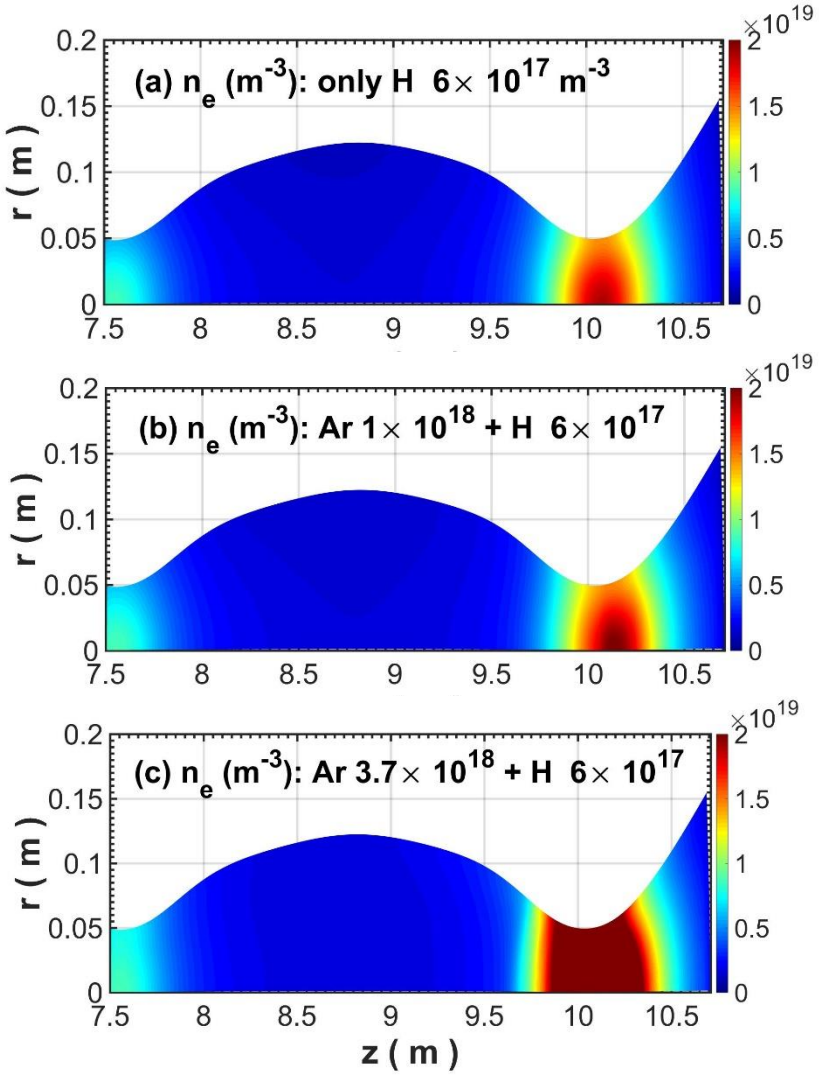

Fig. 4.14 2D profiles of the electron density for (a) only H injection and (b) simultaneous injection of H and Ar $6 \times 10^{17}\mathrm{m}^{-3}$ (c) simultaneous injection of H and Ar $3.7 \times 10^{18}\mathrm{m}^{-3}$.

The dependence of plasma parameters on the target plate (at r =0 cm) against the Ar neutral density is shown in Fig 4.15. The dependence of the T_e on the target plate (at r =0 cm) as a function of the injected Ar neutral density is plotted in Fig. 4.15 (a). The electron temperature on the target plate reduces as the injected Ar density is increased. For the strongest Ar injection case, the T_e on the target plate reduces to nearly 3.8 eV.

The dependence of ion temperature (T_i) on the target plate as a function of injected Ar neutral density is shown in Fig. 4.15 (b). A slight influence of Ar seeding on the ion temperature has been observed. The ion temperature reduces slightly with the increasing Ar injection.

The dependence of electron density (n_e) on the target plate on the injected Ar neutral density is shown in Fig. 4.15 (c). The electron density increases with the increasing Ar injection. A tendency of saturation in the electron density has been observed at the high Ar injection case.

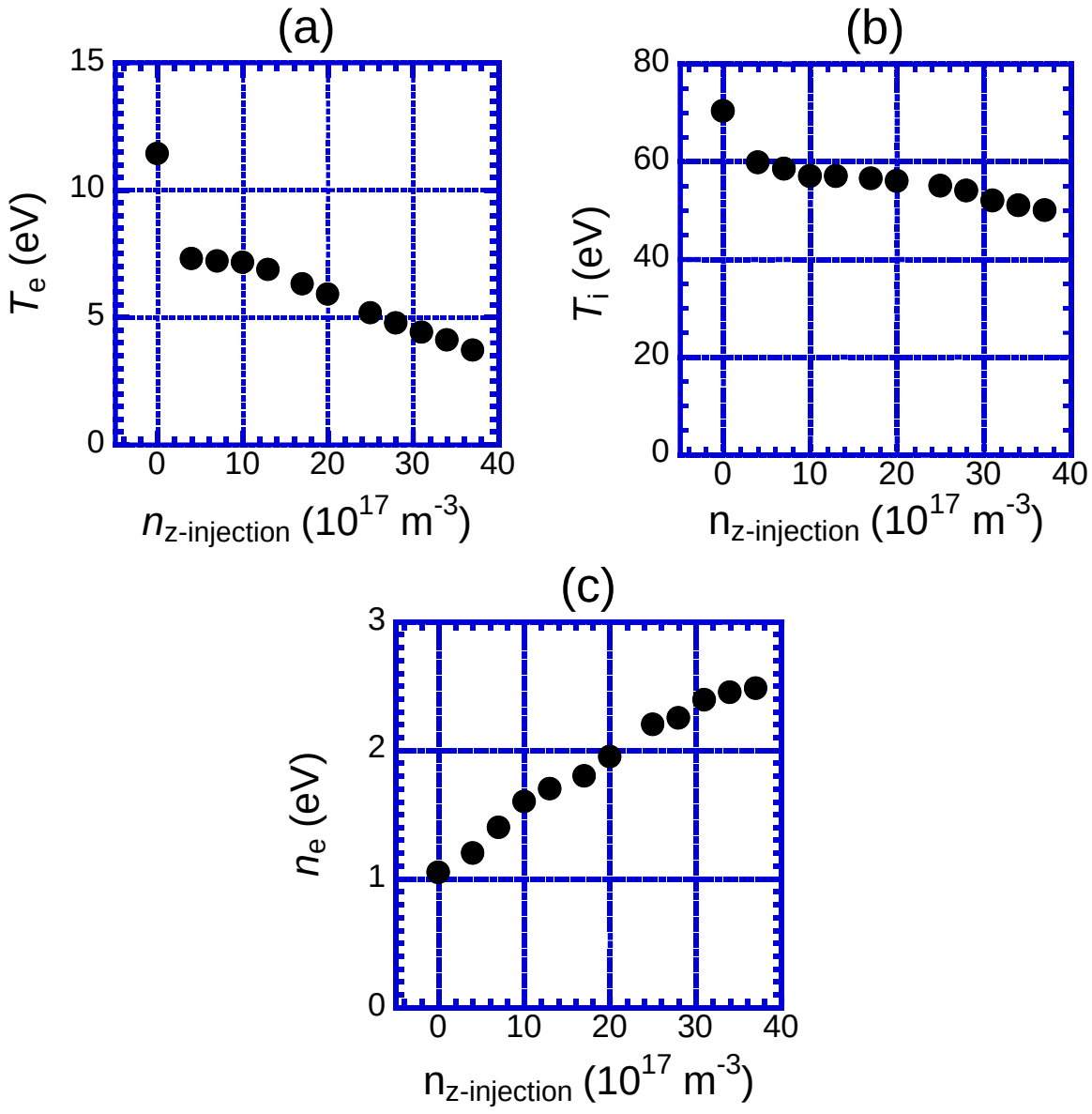

Fig. 4.15 Dependence of plasma parameters on the target plate (at r=0 cm) (a) electron temperature (b) ion temperature and (c) electron density as a function of the injected Ar neutral density.

The energy loss processes have also been investigated to explore the physical mechanism of energy loss processes during neutral Ar seeding. The dependence of the CX loss and recombination loss as a function of the injected Ar neutral density is shown in Fig. 4.16 (a). The CX loss slightly reduces with the increasing Ar injection. The ion temperature reduces slightly with the Ar injection, which induces a slight reduction in the CX loss. The radiative power loss of Ar increases significantly during Ar injection. The Ar radiation power loss increases significantly with the increasing Ar injection, which reduces the electron temperature.

The recombination loss is very small. However, the recombination loss increases as the electron temperature is reduced. The recombination processes play a driving role in the low temperature region ($T_e < 1$ eV). In this study, T_e reduces to about 3 eV. At such the temperature range hydrogen ionization reaction rate coefficient is much higher than that of the recombination rate.

The power loss due to the ionization of hydrogen neutral particles slightly reduces with the increasing Ar neutral density. As the electron temperature is reduced, the ionization rate coefficient reduces, which affects the total ionization power loss.

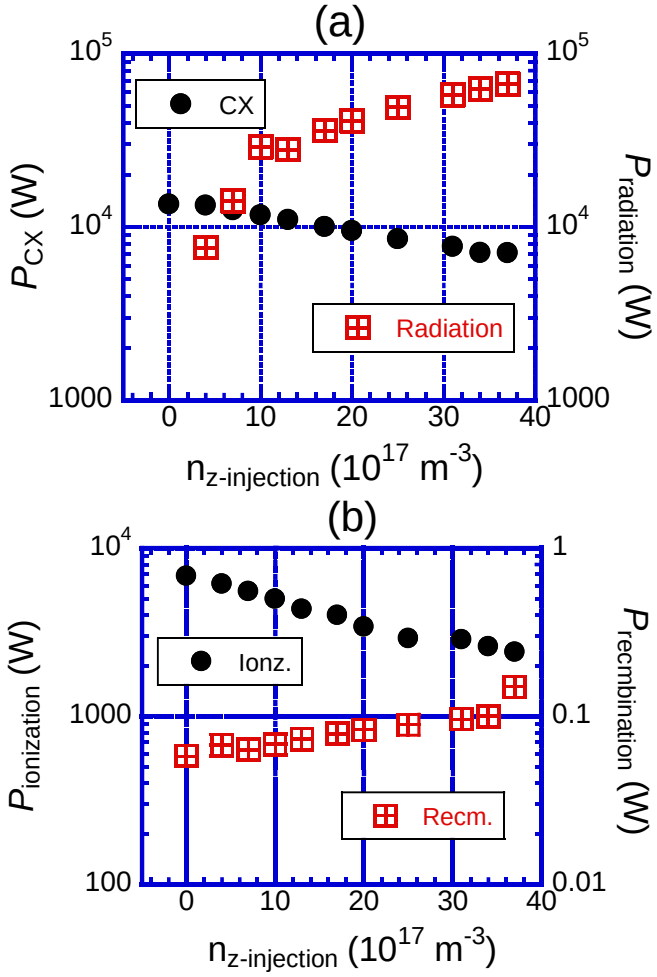

Fig. 4.16 Dependence of (a) CX loss and recombination loss, and (b) ionization loss and Ar radiative loss as a function of Ar neutral density.

C. Comparison among Ar, Kr and Xe.

In the study, radiator gases Ar, Kr and Xe were injected with a viewing to investigate the radiation cooling effects of the radiator gases toward the generation of plasma detachment. A comparison among the three radiator gases is done by using the LINDA code. The simulation outcomes are shown in Figs. 4.17-4.23. The 2D hydrogen neutral density profiles are shown in Fig. 4.17. The hydrogen neutral density increases near the target plate. Increasing region in the density profile near the target plate represents the contribution of recycling hydrogen neutrals on the hydrogen density. The hydrogen neutral density exhibits a dependency on the impurity neutral species. It is shown that the hydrogen neutral density is higher during Xe seeding than that of Ar and Kr seeding. Xe seeding in the end-cell reduces the electron temperature significantly. The ionization reaction rate coefficient for the hydrogen neutral depends on the electron temperature. The ionization reaction rate reduces according to the reduction in the electron temperature and consequently, affects the hydrogen neutral particles decay toward the upstream region. It is speculated that the ionization rate of the hydrogen neutral particles significantly reduces near the target plate during Xe injection comparing to the Ar and Kr injection. Xe seeding also increases the upstream plasma density. As a result, the recycling hydrogen neutral density has been found to be high for Xe seeding than that of Ar and Kr seeding.

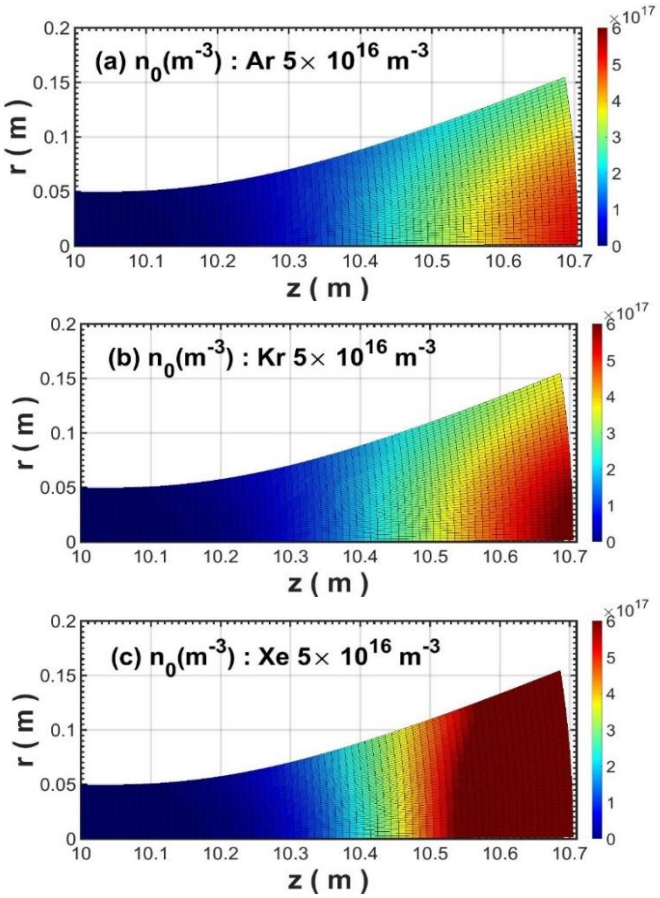

Fig. 4.17. The 2D profiles of the recycling hydrogen neutral density for (a) Ar (b) Kr and (c) Xe injection.

Figure 4.18 represents the 2D data of electron temperature in the case of impurity neutral density of 5×10^{16} m^{-3}. Xe seeding shows the most promising effects on the reduction of electron and ion temperature. The electron temperature decreases near the target plate during neutral impurity seeding, especially for the Xe injection, a noticeable reduction in the electron temperature has been shown, which implies stronger radiation cooling effects of Xe. On the other hand, Ar seeding is the least effective among the three impurity gases on the reduction of electron temperature.

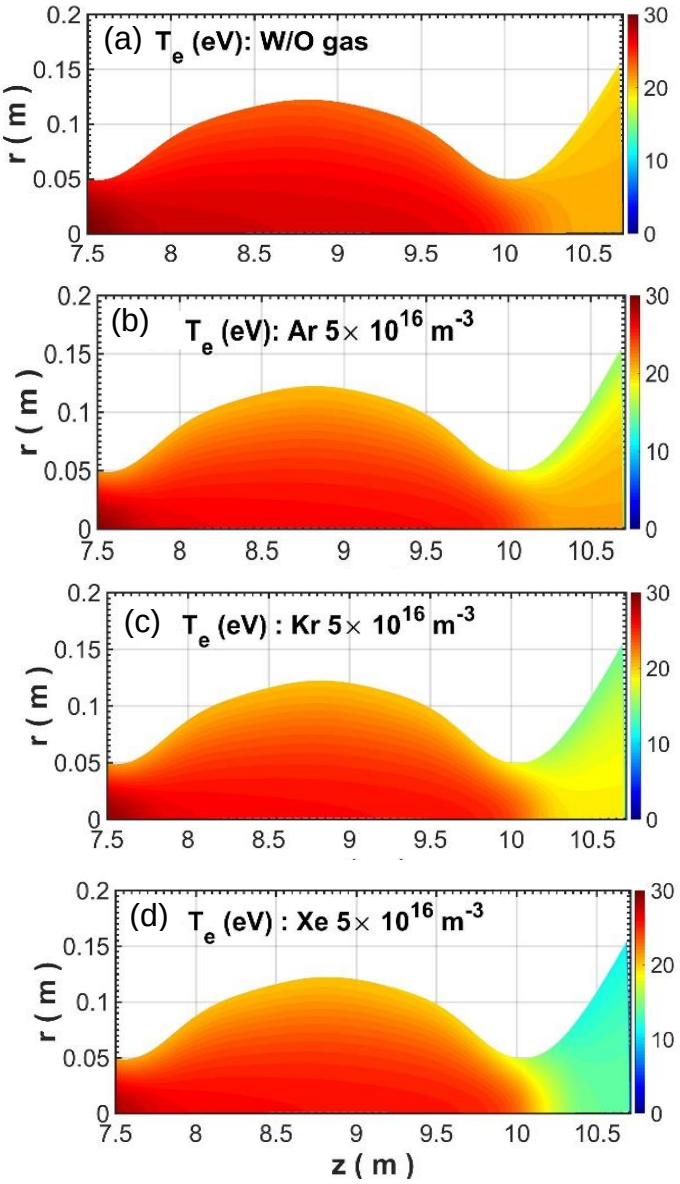

Fig. 4.18. 2D profiles of the electron temperature for (a) W/O any gas (b) Ar (c) Kr and (d) Xe injection.

Figure 4.19 shows the 2-D profiles of ion temperature during Ar, Kr and Xe seeding. The hydrogen ion temperature also reduces near the target plate due to impurity gas seeding. In the ion temperature reduction, Xe also shows the most promising results than that of Ar and Kr.

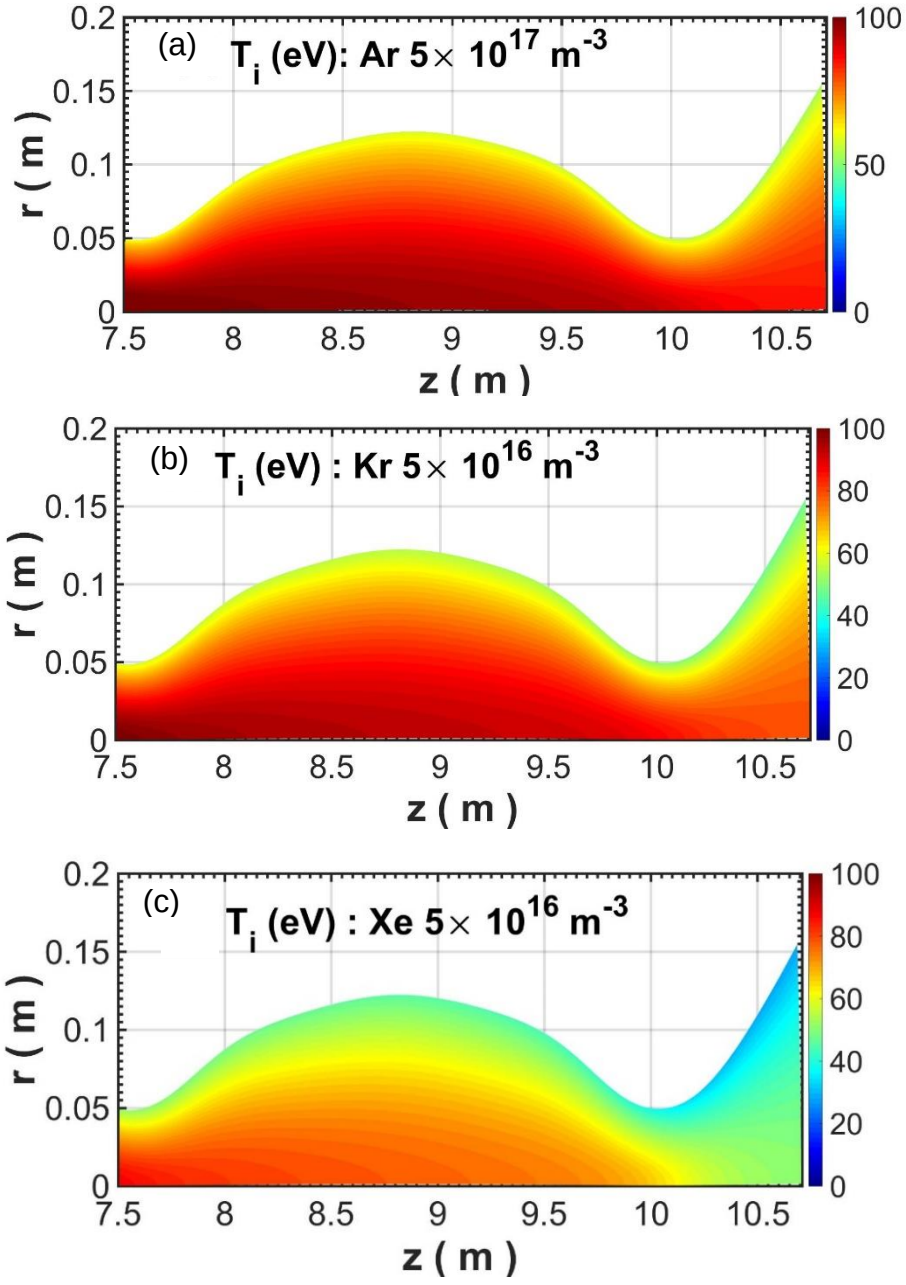

Fig. 4.19. 2D profiles of the ion temperature for (a) Ar (b) Kr and (c) Xe injection.

The 2-D profiles for the electron density are shown in Fig.4. 20. In the figure, two peaks are shown. The 2nd peak- position (z ~ 10 m) in the density profile is due to the flux tube conservation. Since the mesh areas in these regions are smaller than that of other areas, the electron density enhances due to the flux conservation. Furthermore, a clear dependence of electron density on the impurity neutral species has been observed from the Fig. 4.20. The highest increment in the density profile is shown for Xe seeding, which implies ionization effects of Xe neutral particles.

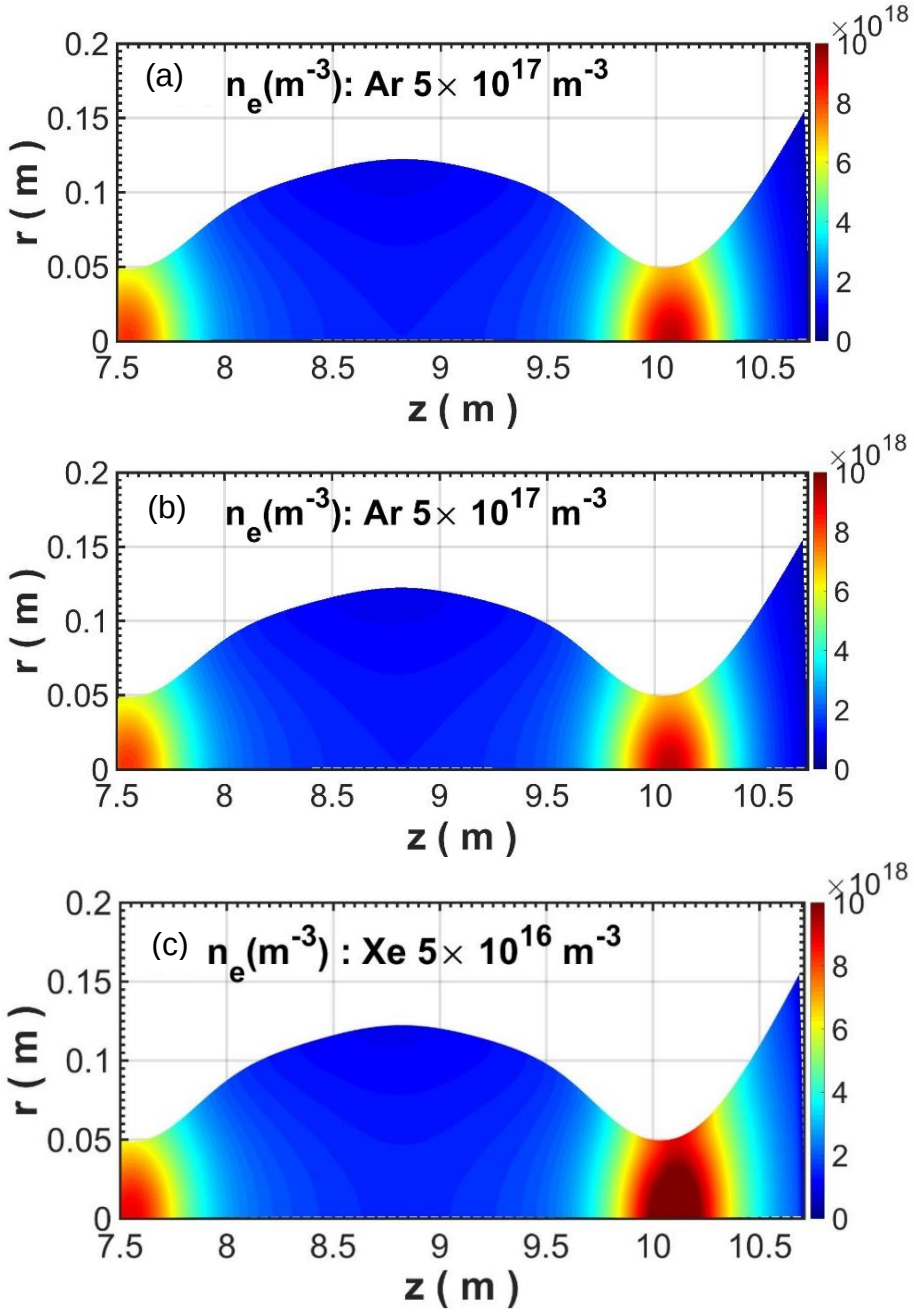

Fig. 4.20. 2D profiles of the electron temperature for (a) Ar (b) Kr and (c) Xe injection.

Figure 4.21 shows a dependence of the plasma parameters on the target plate (at r=0 m) against the seeded impurity neutral density. It is shown that the temperature of electron and ion reduce with the increasing impurity neutral density. The plasma parameters also show a clear dependence on the neutral species Ar, Kr, and Xe. For Ar seeding at the density of 1×10^{17} m^{-3}, T_e and T_i on the target plate reduce from nearly 19 eV to 10 eV and 90 eV to 84 eV, respectively. On the contrary, for Kr 1×10^{17} m^{-3} and Xe 1×10^{17} m^{-3} seeding, the electron temperature (T_e) reduces to nearly 8.4 eV and 3.9 eV, respectively. Furthermore, the hydrogen ion temperature (T_i) on the target plate also decreases to nearly 67 eV and 33 eV in case of Kr and Xe seeding at the density of 1×10^{17} m^{-3}, respectively. As for the electron density, an increase has been recognized with the increment of impurity neutral density. An effect of neutral species on the electron density has also been shown in the figure. It is shown that Xe seeding leads to a strong increase in density, which indicates stronger ionization effects of Xe neutral particles. On the other hand, Kr shows intermediate effects between Ar and Xe, which is consistence with the atomic database of the gases.

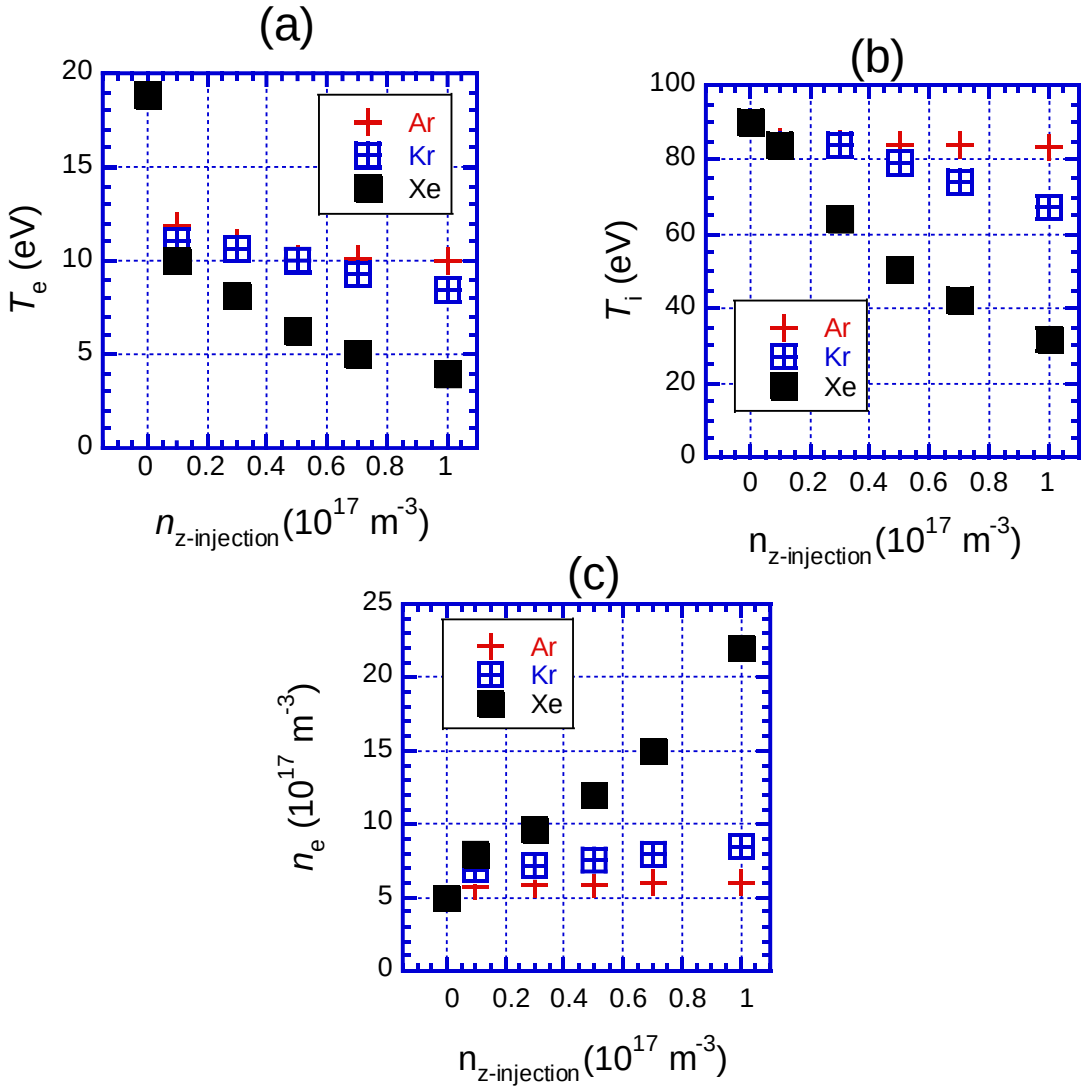

Fig. 4.21 Dependence of (a) electron temperature, and (b) ion temperature (c) electron temperature as a function of impurity neutral density.

Figure 4.22 shows the source and sink terms of the energy equations (S_E^e and S_E^i). The power loss during Kr, Ar and Xe seeding are plotted in the figure. It is shown that both the ion and electron energy loss enhance remarkably during Xe seeding than that of Ar and Kr. Xe can be easily ionized comparing to Ar and Kr because of low ionization potential. Xe seeding increases electron density significantly, which enhances total loss channels. The radiation cooling rate of Xe is higher than that of Ar and Kr. As T_e is reduced, the energy exchange between electrons and ions is also increased, which induces a slight reduction in the ion temperature (T_i). However, this rate strongly depends on the plasma density. The plasma density increases during Xe seeding compared with the Ar and Kr seeding. As a result, this rate is also increased according to the increment of the electron density. Hence, reduction in the ion temperature is also high for Xe injection. The atomic and molecular processes of hydrogen play a very important role in the divertor plasma. The ionization reaction rate of neutral particles reduces according to the decreasing of electron temperature. On the contrary, the charge exchange reaction rate coefficient ($<\sigma v>_{cx}$) between hydrogen ion and neutral has a poor dependency on the plasma ion temperature. The CX reaction rate coefficient is almost constant in the temperature range from 30 eV to 70 eV. The CX loss strongly depends on the proton and neutral density.

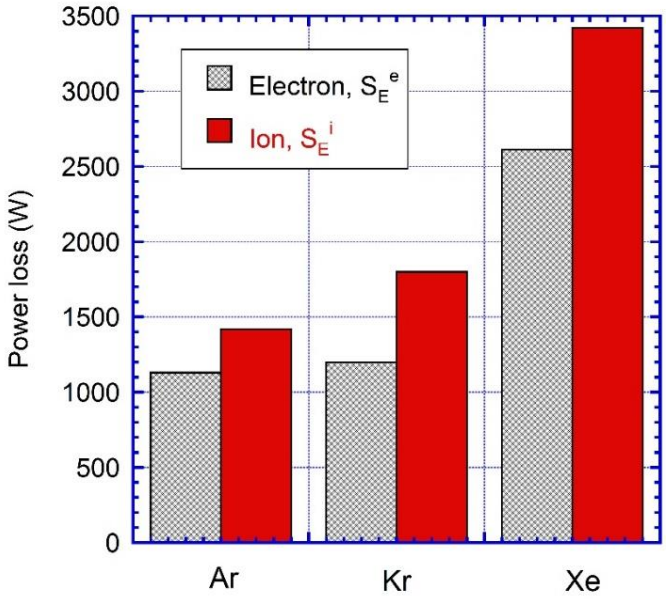

Fig. 4.22 Volume integrated power loss terms for electron and ion in case of injected density 5×10^{16} m^{-3}.

Figure 4.23 shows the 2-D profiles of power loss for the charge-exchange (CX) between proton and hydrogen neutral. The CX loss is expressed by the following formula,

$$P_{CX} = n_0 \times n_i \times < \sigma v >_{CX} \times T_i.$$

It is shown that the CX loss strongly enhances toward the target plate (hydrogen neutrals density is high due to the recycling). Moreover, the CX loss also high for Xe seeding than that of Ar and Kr

seeding. Influence of Xe seeding in the plasma parameters (density, temperature, neutral) significantly contributes to the CX loss profile.

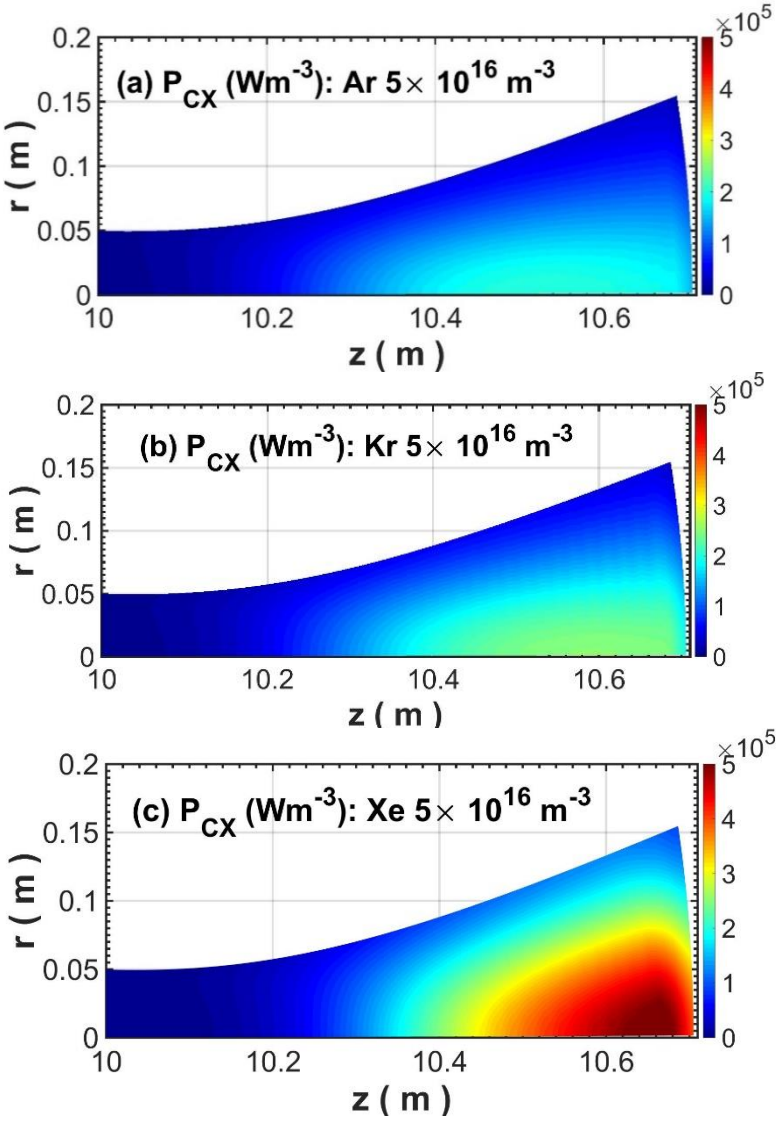

Fig. 4.23 CX loss (a) Ar (b) Kr and (c) Xe injection.

The hydrogen ionization power loss during Ar, Kr and Xe seeding is shown in Fig.4.24. The ionization power loss has been concentrated toward the target plate due to the recycling hydrogen neutral. A similar loss profile has been observed for Ar and Kr seeding. However, the loss is high for Xe seeding than that of Ar and Kr.

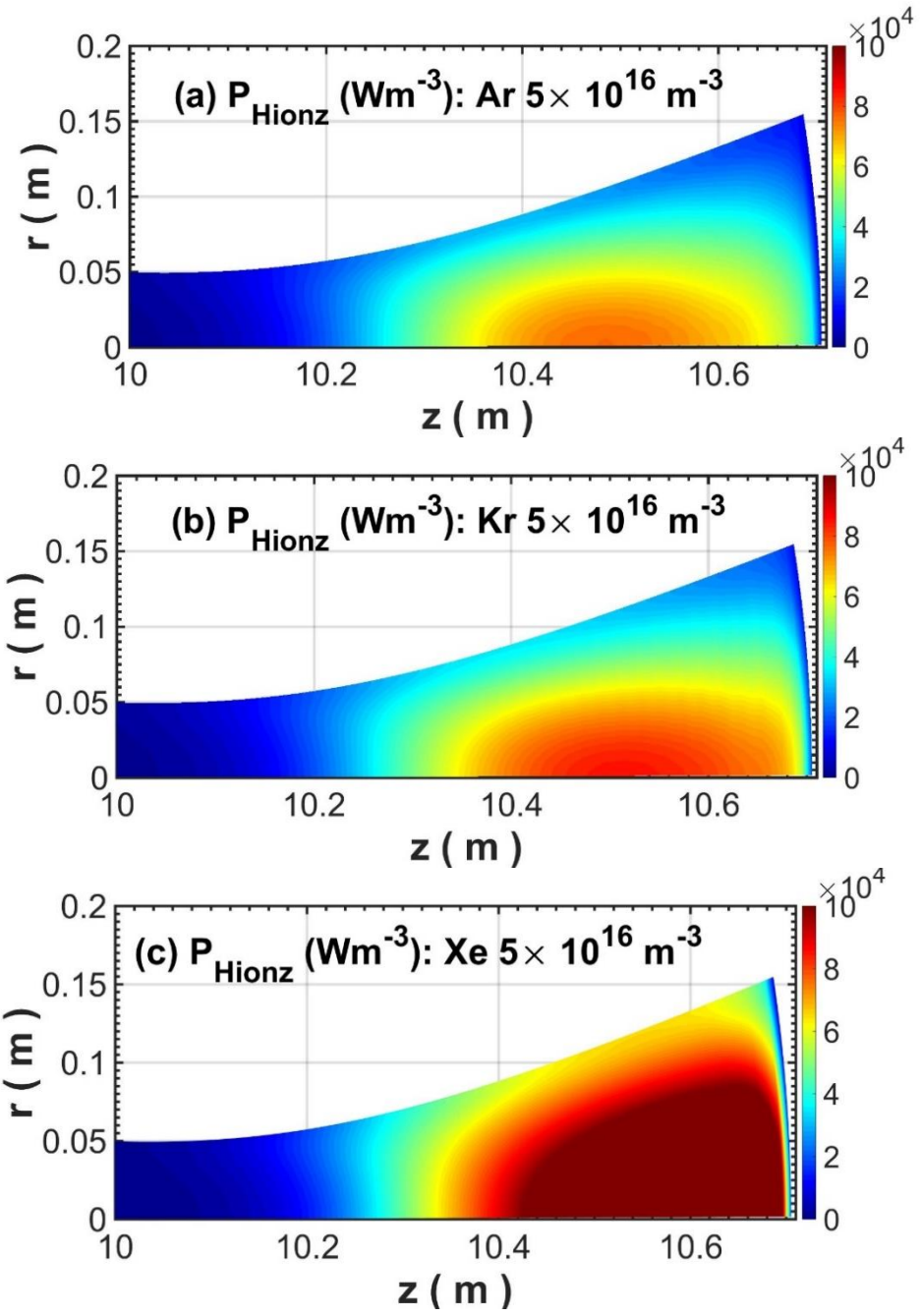

Fig. 4.24. 2-D profile of power loss due to ionization of H_0 (P_{Hioniz}) in the case of (a) Ar injection (b) Kr injection (c) Xe injection.

Figure 4.25 shows the 2D profile of the source terms of the momentum balance equation. The source terms of the equation are the pressure dropped per unit length (Pa/m). It is shown that the plasma pressure drops near the target plate because of the interactions of plasmas with the neutral particles. A noticeable effect of Xe seeding has been observed in the pressure drop profile.

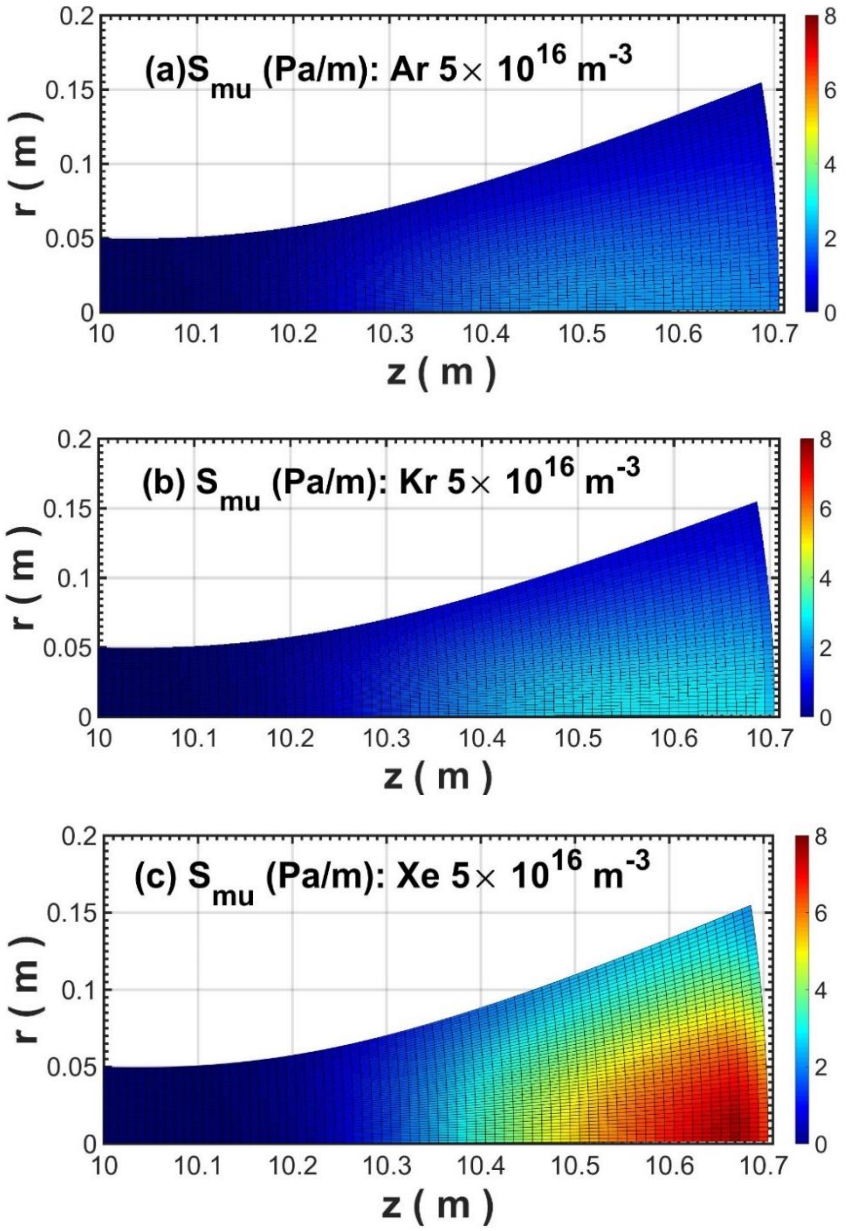

Fig. 4.25. 2-D profile of source terms of the momentum balance equation (S_{mu}) in the case of (a) Ar injection (b) Kr injection (c) Xe injection.

Figure 4.26 shows the radiation power loss during Ar, Kr and Xe seeding under the condition of neutral density 5×10^{16} m^{-3}. It is shown that the radiation power loss is much higher during Xe seeding than that of Ar and Xe seeding.

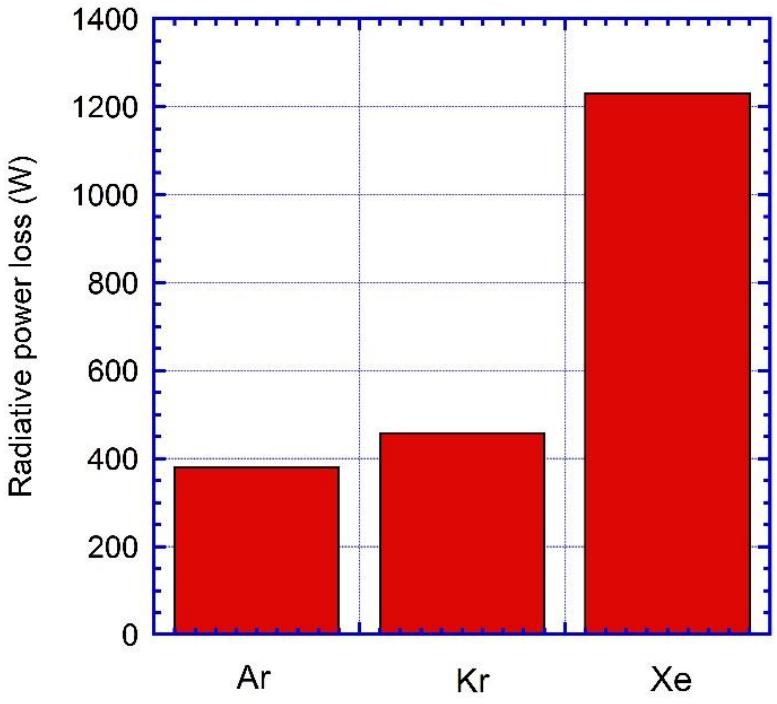

Fig. 4.26. Volume integrated radiation power loss for Ar, Kr and Xe in case of injected density 5×10^{16} m^{-3}.

From the above discussion, it can be summarized that impurity injection in the divertor region is effective on the reduction plasma energy. A comparison among the three radiator gases shows that Xe seeding in the divertor region is the most effective radiator gas towards the generation of detached plasma. Xe seeding into the end-cell of GAMMA 10/PDX significantly increases the electron and ion energy loss channels.

4.2.2 Simulation results at the upstream density: $n_{i0} = 1 \times 10^{19} \mathrm{m}^{-3}$.

In the study, the injected hydrogen neutral density at the end-cell is fixed at $5 \times 10^{17}\ \mathrm{m}^{-3}$ while the Ar neutral density is varied. The 2D profiles of the electron temperature for the simultaneous injection of Ar and H are shown in Fig. 4. 27. It is shown that the electron temperature reduces near the target plate as the injected Ar neutral density is increased. Figure 4.27 shows a comparison of the electron temperature for the injected Ar neutral density of Ar $1 \times 10^{18}\ \mathrm{m}^{-3}$ and Ar $3 \times 10^{18}\ \mathrm{m}^{-3}$. For the strongest Ar injection, the electron temperature near the target plate is reduced drastically, which indicates the radiation cooling effects of Ar neutral particles. On the other hand, a slight influence of Ar seeding on the ion temperature is observed as shown in Fig 4.28.

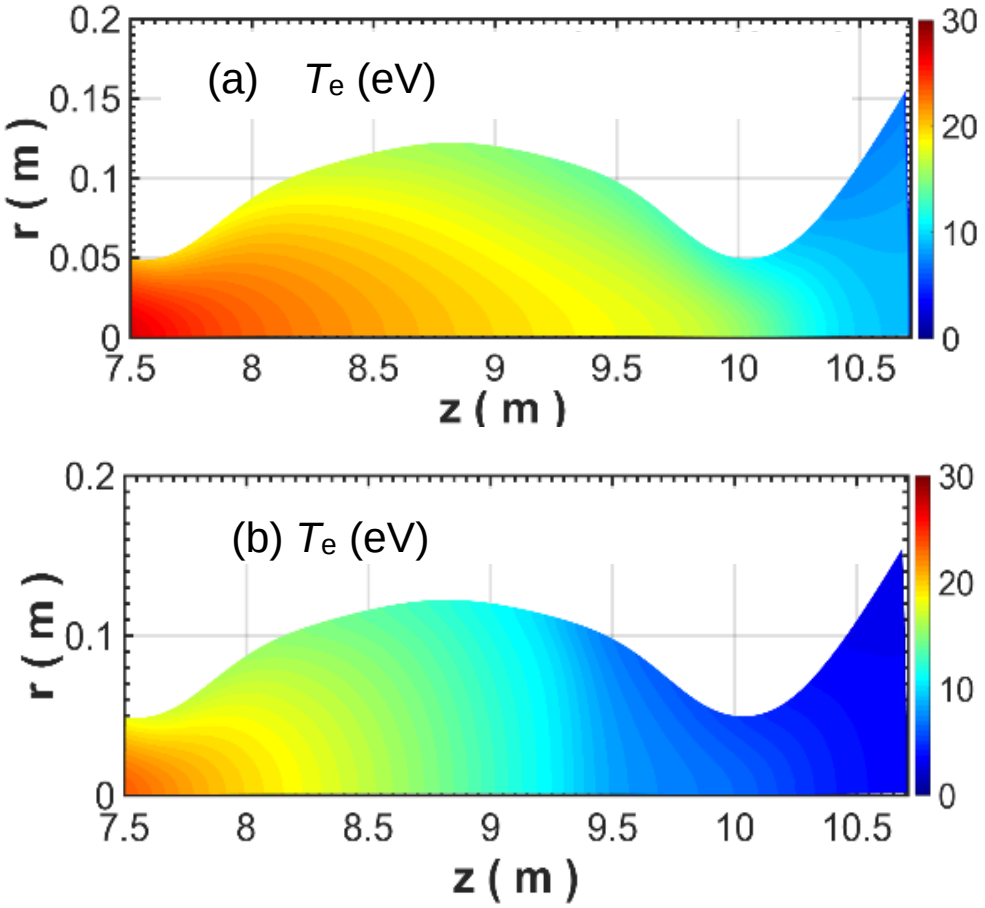

Fig. 4.27 2D profiles of the electron temperature (a) Ar $1 \times 10^{18}\ m^{-3}$(b) Ar $3 \times 10^{18}\ m^{-3}$.

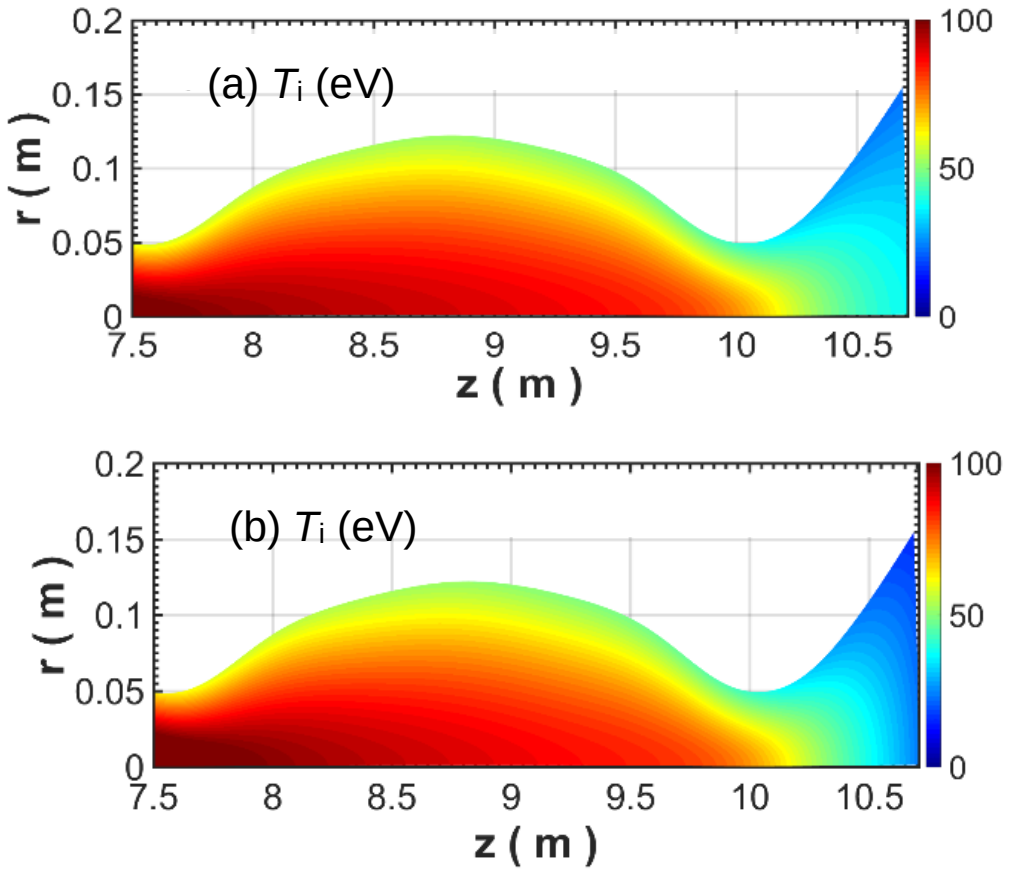

Fig. 4.28 2D profiles of the ion temperature (a) Ar $1 \times 10^{18}\ m^{-3}$ (b) Ar $3 \times 10^{18}\ m^{-3}$.

The dependence of the plasma parameters on the target plate is shown in Fig. 4.29. The electron temperature on the target plate is reduced as the injected Ar neutral density is increased. For the strongest Ar injection, the electron temperature on the target plate reduces to about 1 eV. The electron density increases at the lower Ar injection, On the other hand, at the higher Ar injection, electron density begins to reduce. The electron density shows a roll-over phenomenon. The ion temperature on the target plate reduces slightly as the injected Ar neutral density is increased. For the strongest Ar injection, the electron temperature on the target plate reduces to about 30 eV. A slight increase in the particle flux is observed at the lower Ar injection. On the contrary, at the higher Ar injection, the particle flux is started to reduce. The particle flux also shows a roll-over phenomenon.

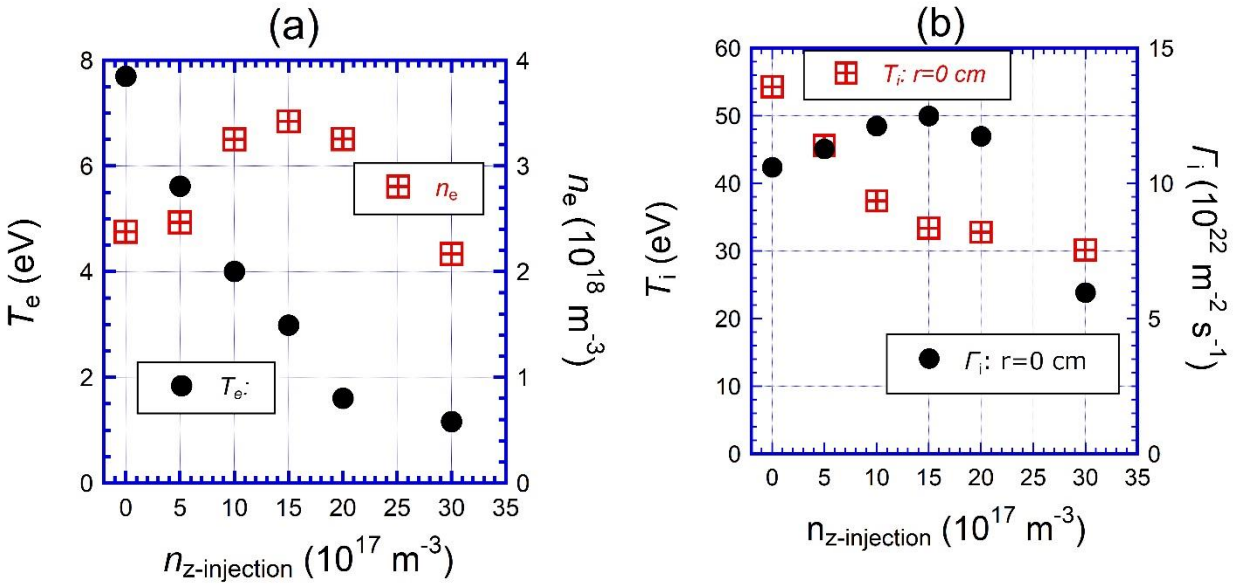

Fig. 4.29 Dependence of (a) electron temperature and density, (b) ion temperature and particle flux a function of Ar neutral density.

4.2.3 Comparison between Ar and Ne

The radiator gases Ar and Ne have been injected in order to understand the effects of Ar and Ne injection on the plasma parameters toward the generation of plasma detachment. As for the neutral models, the injected H neutral density is fixed at 5.0×10^{17} m^{-3}, while the injected Ar and Ne neutral density is changed from 0.0 to 2.1×10^{18} m^{-3}. Figure 4.30 shows the 2-dimensional profiles of the electrons temperature, ions temperature and electrons density when injected Ar and Ne impurity density was 1.0×10^{18} m^{-3}. The electron and ion temperatures reduce near the target plate due to the interactions of plasma with the neutrals particles. Particularly in the electron temperature (T_e) a remarkable reduction is shown for Ar injection, which indicates stronger radiation cooling effect of Ar. On the contrary, a slight reduction in the T_e is shown during Ne seeding. Two peaks are shown in the electron density profiles. The location of the peak (z~10 m) in the density profile corresponds to the magnetic field configuration (due to the flux conservation) of the GAMMA 10/PDX. The magnetic flux tube in these regions is thinner than that of the others. Therefore, electron density increases in this region. Moreover, a slight increase in the electron density has been observed for Ar injection, which indicates the ionizing effect of neutral particles.

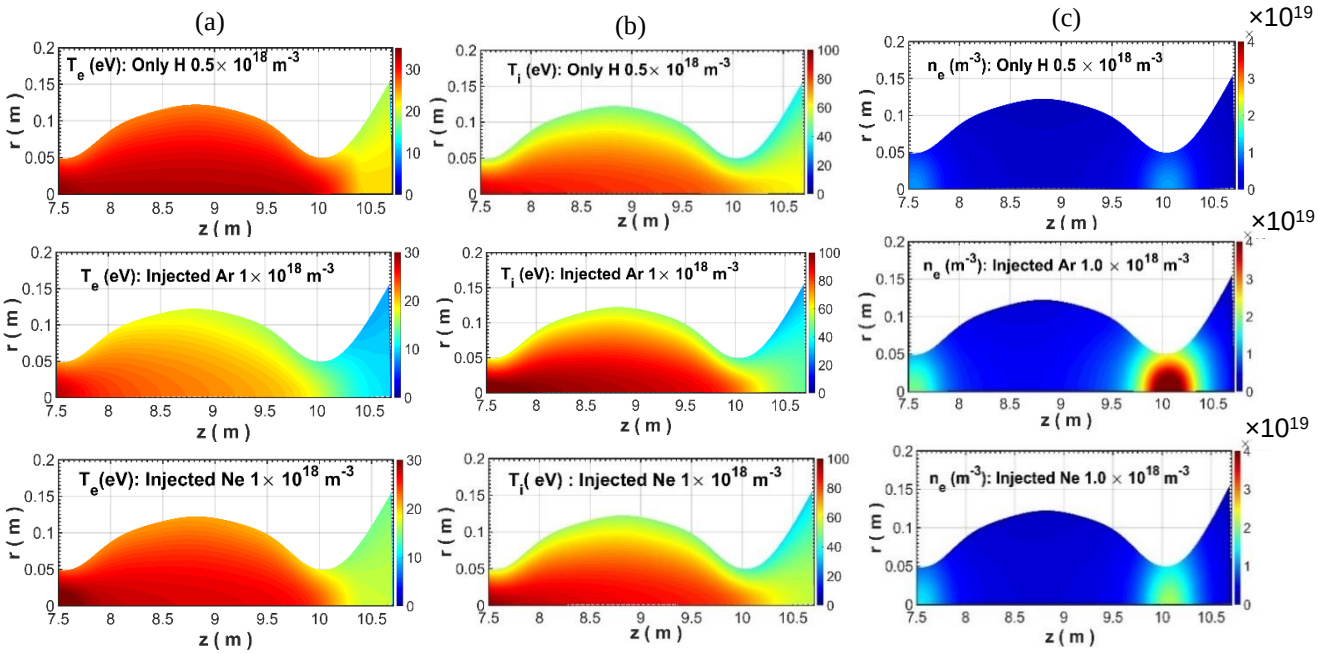

Fig. 4.30 2D profiles of the (a) electron temperature (b) ion temperature (c) electron density.

Figure 4.31 shows the dependence of plasma parameters on the Ar and Ne seeding density. As shown in Fig. 4.31 (a), the electron temperature on the target plate reduces with the increasing Ar seeding. On the other hand, for the Ne seeding, a slight reduction in the electron temperature has been observed. The radiation cooling effects of Ar particles is much higher than that of Ne particle, which induces a reduction in the electron temperature. For the strongest Ar injection, the electron temperature on the target plate reduces to about 2 eV. In contrast to this, for the strongest Ne injection, the electron temperature on the target plate reduces to about 6 eV. The ion temperature on the target plate also reduces with the increasing Ar seeding. A slight reduction in the ion temperature has also been shown for Ne injection. The ion temperature on the target plate reduces from about 52 eV to 32 eV by Ar injection. On the other hand, the ion temperature reduces from about 52 eV to about 45 eV by Ne seeding. At the lower Ar injection range, the electron density increases with the increment of Ar density. However, the electron density reduces at the higher Ar injection case. The electron density shows a so-called roll-over phenomenon for Ar injection. In contrast to this, for the Ne seeding, the electron density continues to increase with the increasing Ne seeding. The electron density is higher for Ar seeding that that of the Ne seeding, which indicates ionization effects of Ar neutral particles. The particle flux also shows a so-called a roll-over phenomenon for Ar injection. On the other hand, the particle flux continues to increase with the increasing Ne seeding. A roll-over phenomenon in the particle flux has not been observed yet for the Ne seeding.

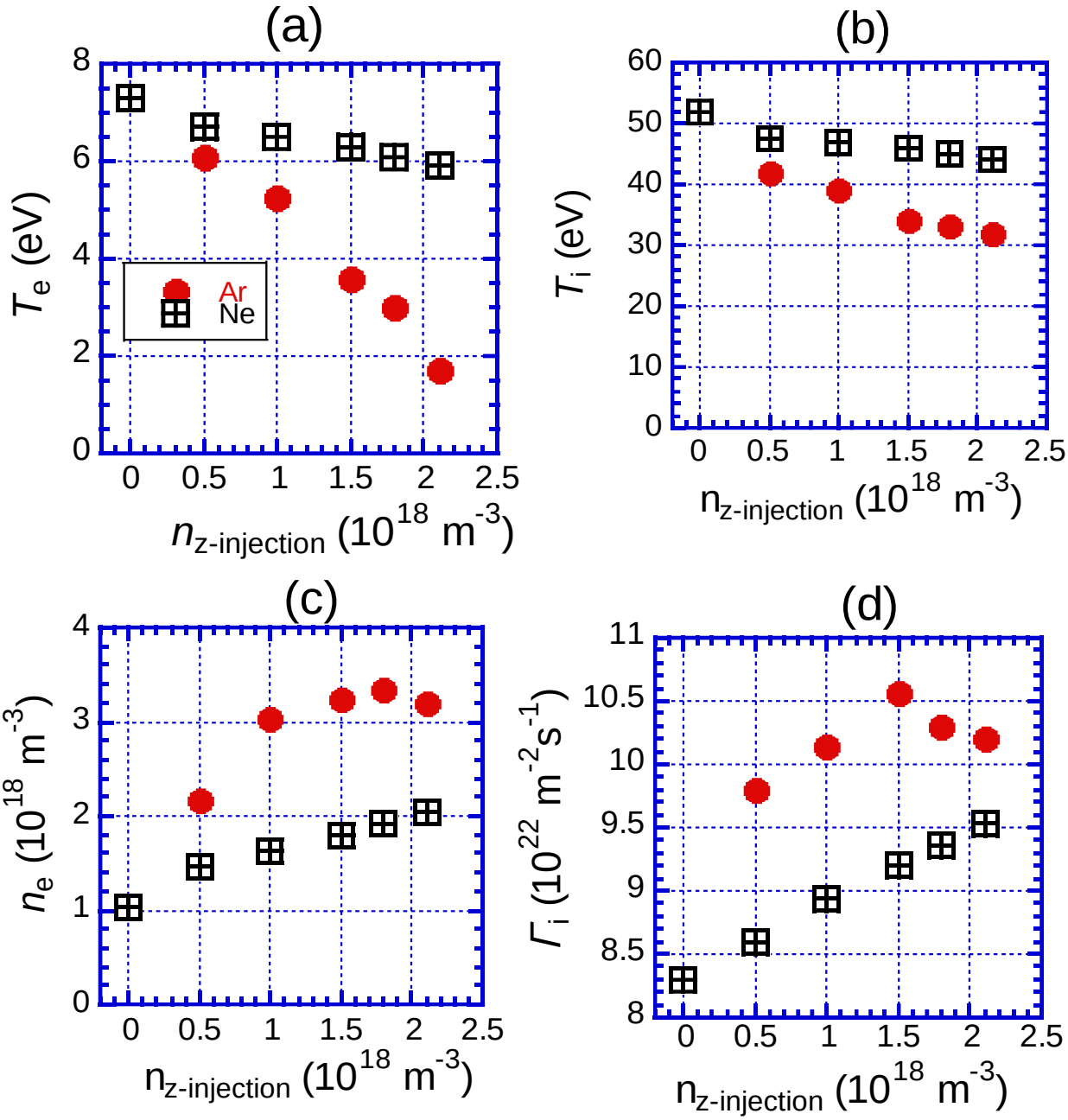

Fig. 4.31 Dependence of plasma parameters on the target plate (a) electron temperature (b) ion temperature (c) electron density (c) particle flux.

The radiative power loss for the Ar and Ne seeding on the target plate is shown in Fig. 4.32. It is shown that the radiative power loss significantly enhances during radiator gas injection. Especially, for the Ar seeding, the radiative power loss is significantly enhanced. The radiative power loss is comparatively high for Ar injection comparing to Ne injection. Therefore, the electron temperature on the target plate reduces remarkably during Ar injection than that of the Ne injection.

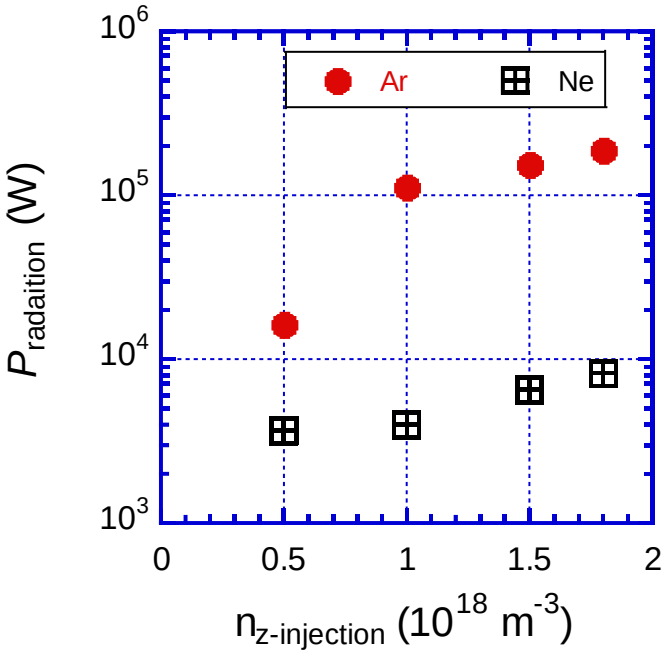

Fig. 4.32 Radiation power loss as a function of the injected Ar and Ne neutral density.

The energy loss terms for ions during Ar and Ne seeding are shown in Fig. 4.33. It is shown that the CX loss increases near the target plate. Since the recycling neutral density is high neat the target plate, the CX increases near the target plate. It is also shown that the CX loss for Ar seeding is higher than that of the Ne seeding. The electron temperature reduces significantly for Ar injection, which reduces the ionization of neutral particles and consequently the hydrogen neutral density is high for Ar seeding than that of Ne seeding. Therefore, the CX loss is high for Ar seeding than that of Ne.

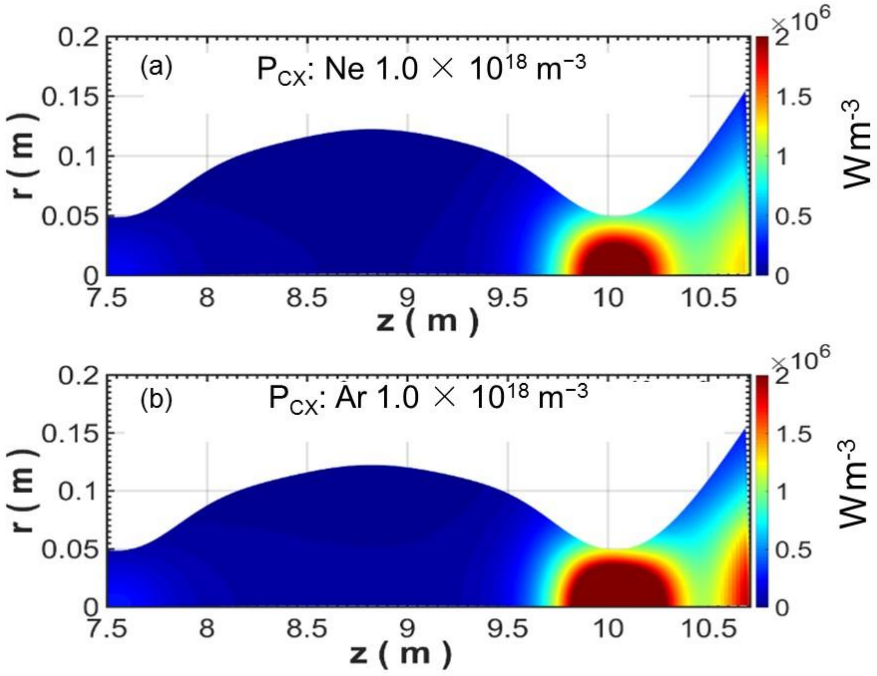

Fig. 4.33 CX loss between H^+ and H^0 for (a) Ne and (b) Ar seeding.

Chapter 5 Coupling between the Fluid and the Kinetic Neutral Code

In this chapter, transport of hydrogen molecules and atom towards the upstream region is studied in the end-cell of GAMMA 10/PDX by developing a kinetic neutral code [92]. In the LINDA code, the neutral models for both the impurity and H are given by solving the fluid equations. A fluid neutral model is computationally faster comparing to the kinetic neutral model. However, the accuracy and validity of the kinetic neutral model are better than that of the fluid neutral model. Furthermore, it is also difficult to include the detailed hydrogen molecular processes in the fluid code. On the other hand, a kinetic neutral code is a robust technique to investigate the detailed molecular dynamics. The hydrogen molecular processes are included in the present code. As an initial step, a series of test calculations has been successfully done by injecting hydrogen molecules from the target plate with fixed plasma background. In addition, the recycling neutral is considered as hydrogen atoms. In the current model, the neutral profile of hydrogen atoms and molecules have been calculated by solving the Boltzmann equation. The aim of this chapter is to investigate the transport of hydrogen atoms and molecules toward the upstream region. In the future, the kinetic neutral code will give us a robust basis to study the MAR effects [67-69] on the plasma detachment that has been recently observed in the GAMMA 10/PDX [66].

5.1 Simulation model

The mesh structure of the simulation region is designed based on the GAMMA 10/PDX magnetic field configuration. The mesh structure of the simulation area is shown in Fig. 5.1. In the present code, the curvilinear orthogonal coordinates system has been considered instead of the cylindrical coordinates system. The x and y directions in the numerical grid correspond to the parallel and radial direction to the magnetic field line. As shown in Fig 5.1, a tungsten target plate is designed at the end of the simulation space. The plasmas flow out from the upstream region to the downstream region while the neutral particles are transported to the upstream region.

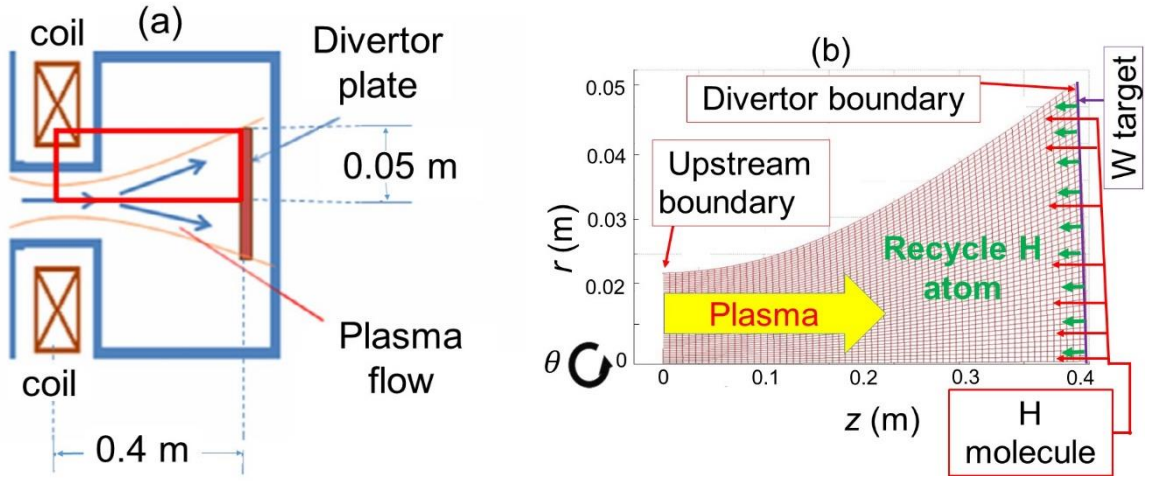

Fig. 5.1. Schematic view of (a) the mesh creation area and (b) mesh structure in the simulation area.

In the coupled fluid-neutral code, the plasma parameters have been calculated by solving the fluid equations (Continuity equation, diffusion equation, momentum balance equation, ion and electron energy balance equation) while the source terms and the neutral particles distribution have been calculated by the kinetic neutral code. The hydrogen neutral particles are defined by solving the Boltzmann equation, which has been calculated based on the Monte Carlo method [55]. The hydrogen molecules are injected into the background plasma at z= 0.4 m and transport toward the plasma upstream direction. The recycling hydrogen neutral particles near the target plate are treated as hydrogen atoms while the gas puffing neutral particles are treated as hydrogen molecules. The hydrogen neutral particles have been injected with the cosine distribution into the bulk plasma. The distribution of the hydrogen gas puffing molecules in the radial direction along the target plate has been written as follows:

$$n_{\mathrm{mol}} = \frac{n_{injected}}{1+2\pi r^2}, \tag{5.1}$$

The recycling hydrogen neutral particles have been written as follows:

$$n_{\mathrm{n}} = R_N \frac{n_i \cdot u_i}{u_n}. \tag{5.2}$$

Where,

n_{n} : recycling hydrogen neutral atoms density,

u_{n} : recycling neutral velocity,

R_{N}: particle reflection coefficient [54],

R_{E}: energy reflection coefficient [54],

n_{i}: hydrogen ion density,

u_{i}: ion velocity,

n_{injected}: injected molecules density.

The atomic and molecular processes of hydrogen have been considered in the kinetic neutral code. The hydrogen atomic and molecular processes are listed in Table 5.1.

Table 5.1. Atomic and molecular processes in the code [53,56-58]

Processes	Reactions
H_2 elastic collision:	$H_2(0) + e \rightarrow H_2(0) + e$
H_2 vibrational excitation:	$H_2(0) + e \rightarrow H_2(1) + e$
H_2 vibrational excitation:	$H_2(0) + e \rightarrow H_2(2) + e$
H_2 ionization:	$H_2(0) + e \rightarrow H_2^+ + e$
H_2 dissociation:	$H_2(0) + e \rightarrow H(1S) + H(1S) + e$
H_2 dissociation:	$H_2(0) + e \rightarrow H(1S) + H(2S) + e$
H_2 dissociation:	$H_2(0) + e \rightarrow H(2S) + H(2P) + e$
H_2 dissociation:	$H_2(0) + e \rightarrow H(1S) + H(n=3) + e$
H ionization:	$H(1S) + e \rightarrow H^+ + e$
H charge exchange:	$H(1S) + H^+ \rightarrow H^+ + H(1S)$
H energy relaxation:	$H(1S) + \mathrm{wall} \rightarrow H(1S)$
H annihilation reaction:	$H(1S) + \mathrm{wall} \rightarrow \mathrm{wall}$

5.2 Distribution of hydrogen neutral

With fixed background plasma parameters, the transport of hydrogen neutral particles has been investigated in the study. The background plasma parameters have been given based on the typical plasma parameters of GAMMA 10/PDX. The 2-D profile of electron density is plotted in Fig.5.2 (a). The 2D profile of the ion and electron temperature are also shown in Figs. 5.2 (b) and (c), respectively.

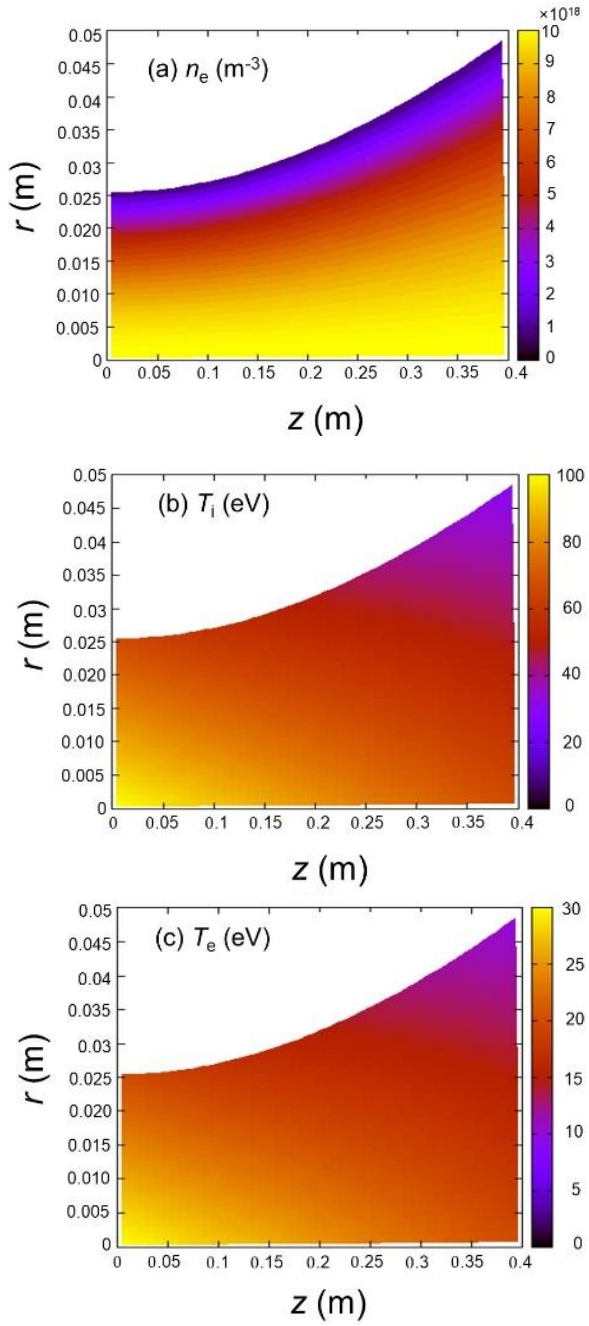

Figure 5.2 2-D profile of fixed plasma parameters during neutral transport study (a) electron density (b) ion temperature (c) electron temperature.

The 2D profiles of the hydrogen neutral atoms and molecules are shown in Figs. 5.3 - 5.5. The distribution of the recycling hydrogen neutral atoms and molecules is shown in Fig. 5.3. It is shown that the recycling hydrogen neutral particles are concentrated close to the target plate and decrease in the plasma upstream direction. In the present simulation condition, there is no source of recycling hydrogen molecules and consequently, the molecule density is 0.0. Figures 5.4 and 5.5 represent the

2-D profiles of hydrogen neutrals atoms and molecules in the case of the gas puffing molecules. The hydrogen neutral atoms are concentrated close to the target plate and decrease in the plasma upstream direction according to the ionization and CX mean free path. In the code, the ion and electron temperature near the target plate is about 60 eV and 20 eV, respectively. Therefore, the dissociation mean free path of the hydrogen neutral particles is too short, thus, hydrogen molecules are concentrated near the z-axis corner of the target and decreases in the plasma upstream direction. The hydrogen molecules have been dissociated into the hydrogen atoms. Hence, the hydrogen atoms density have been enhanced when molecules are injected into the background plasma. It is shown that the dissociated hydrogen atoms contribute remarkably to the hydrogen atoms density profile as shown in Figs 5.4-5.5. The contribution of the gas puffing molecules on the hydrogen atoms density is recognized by comparing the Fig. 3, Fig. 4 and Fig. 5. It is also observed that hydrogen atoms density increases according to the increment of hydrogen puffing molecules.

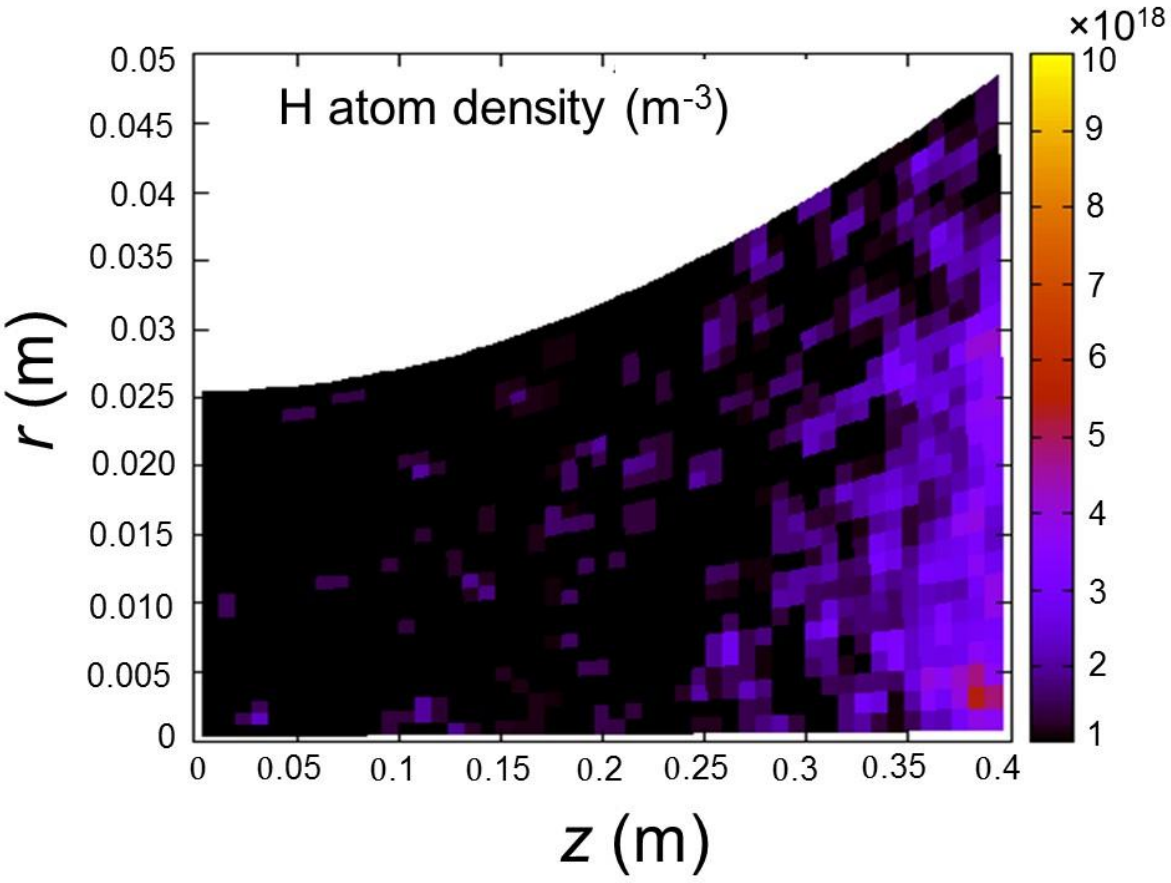

Figure 5.3 2-D profile of recycling hydrogen neutral atoms in the case of gas puffing molecules 0.0.

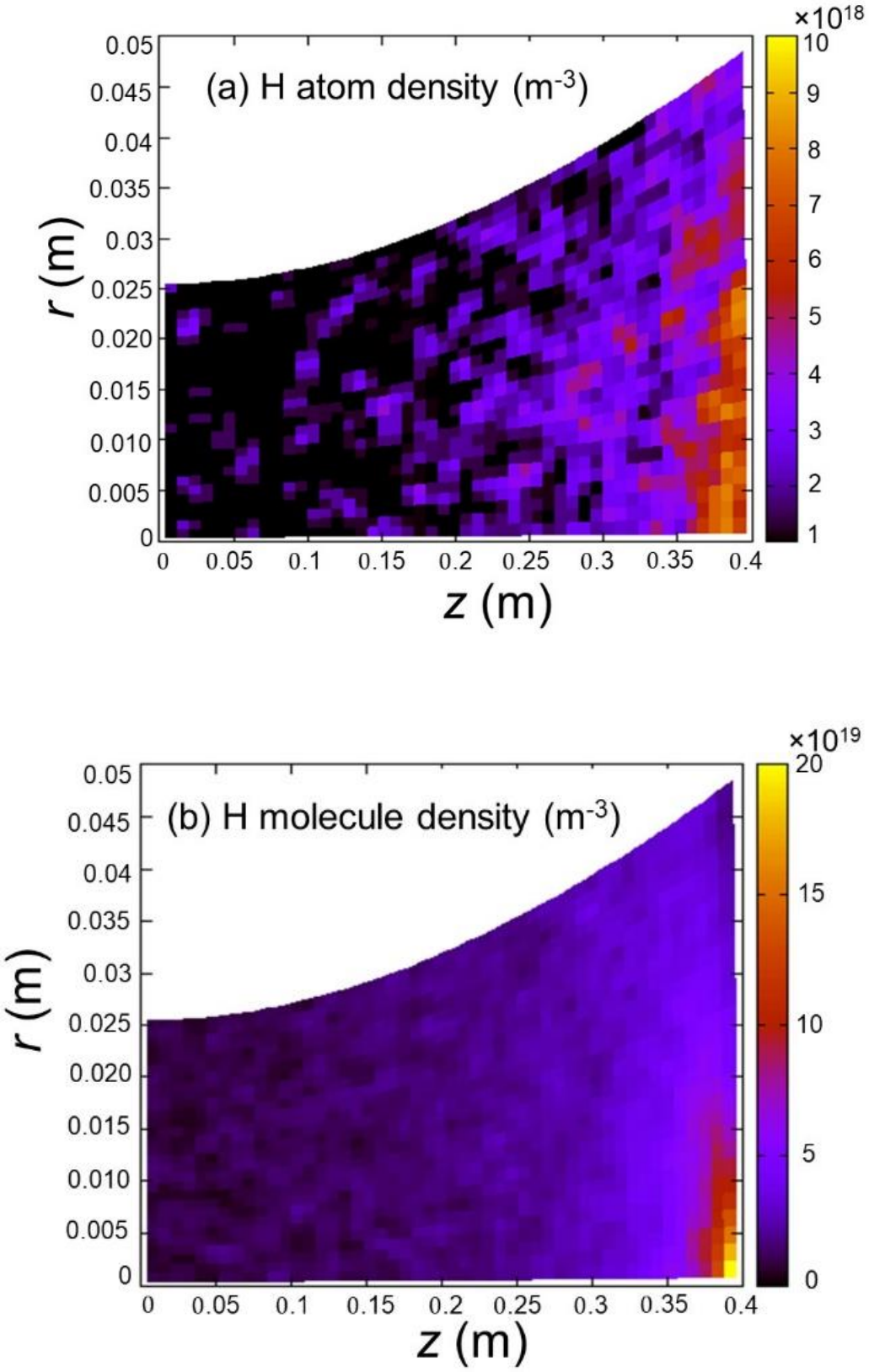

Figure 5.4 2-D profile of hydrogen neutral atoms (a) and molecules (b) under the condition of gas puffing molecules 2.5 $\times 10^{20}$ m^{-3} at z-axis on the target plate.

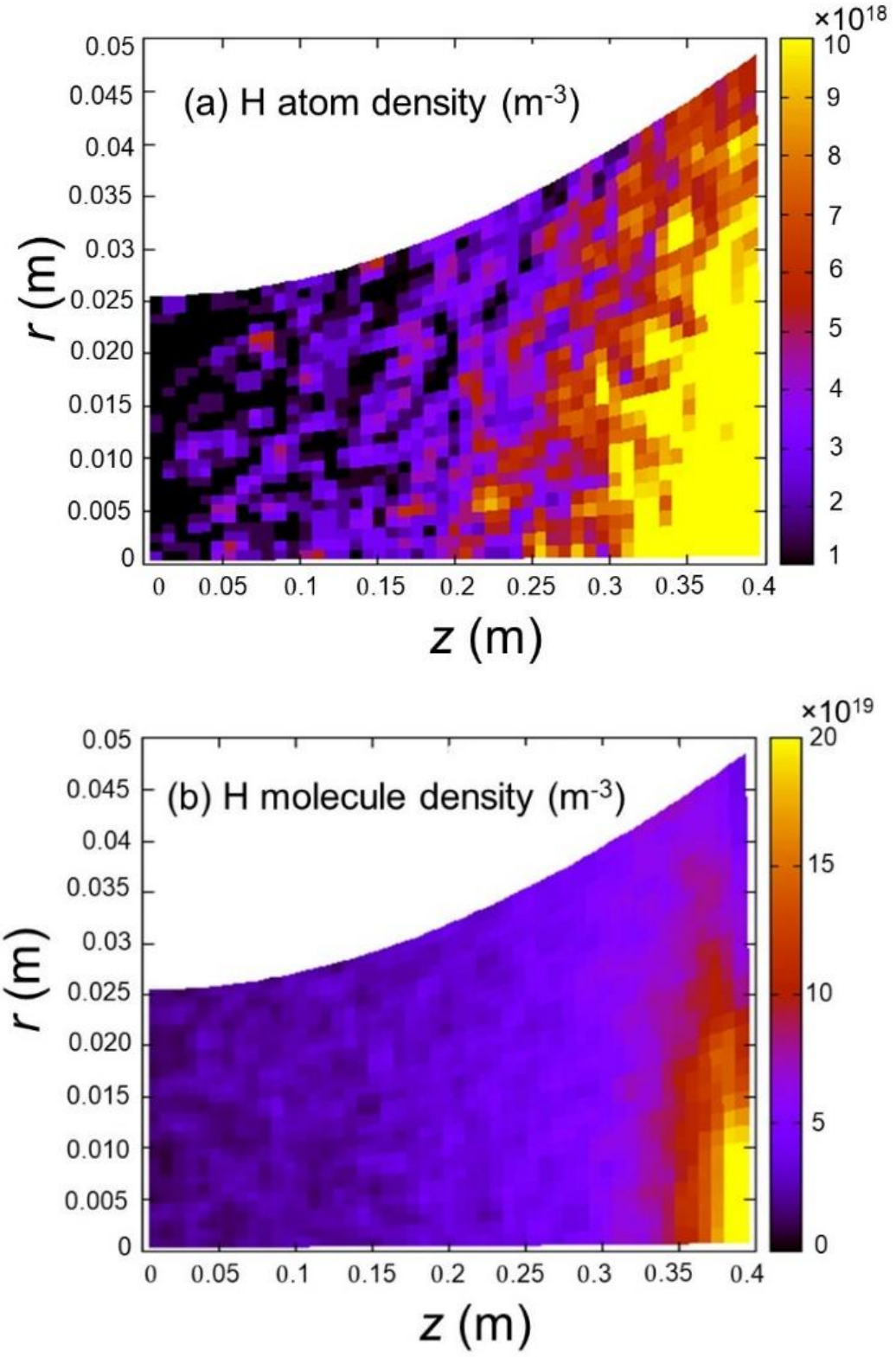

Figure 5.5 2-D profile of hydrogen neutral atoms (a) and molecules (b) under the condition of gas puffing molecules 5.0 $\times 10^{20}$ m^{-3} at z-axis on the target plate.

Chapter 6 Conclusions

6.1 Experimental summary

In the thesis, we have studied the behavior of plasma parameters during neutral gas injection in the D-module of GAMMA 10/PDX based on the calorimeter and Langmuir probe measurements. The obtained experimental results are summarized as follows. The plasma parameters in the D-module have shown a clear dependence on the gas density and gas species. It has been shown that impurity injection into the D-module reduces the electron temperature, heat flux and particle flux. As for the z-axis, the heat flux reduces toward the plasma downstream according to the increasing gas plenum pressure. The peak of the heat flux attains at the Y= 0 cm and reduces toward both the Y directions. The heat flux distribution becomes uniform at the higher gas injection. Xe seeding leads to a strong reduction in the heat flux. The heat flux reduction order is Xe > Kr > Ar. Xe shows the best performance on the reduction of heat flux.

The time behavior of the ion flux has also been measured during Ar, Kr and Xe injection. The ion flux remains almost constant with time in the case of without any gas injection. The ion flux decreases when impurity gas is injected into the D-module. A comparison among the three gases shows that Xe is the most effective radiator gas on the reduction of ion flux. The ion flux reduces drastically for Xe injection.

The electron density initially increases at the lower gas injection, but later the electron density is decreased at the higher gas injection. For impurity injection at the plenum pressure of 100 mbar, the electron density increases significantly during Xe injection comparing to Ar and Kr injection, which indicates the ionizing effect of Xe neutral particles. Reduction in the electron density has been observed at the higher gas injection. Hence, the electron density shows a roll-over phenomenon for impurity injection. The electron temperature also reduces due to impurity injection. The electron temperature reduces to about 2 eV for Xe injection. Xe injection into the D-module has shown the best result on the reduction of plasma parameters. These results strongly indicates that the plasmas in the D-module became detached due to the impurity injection.

From the above discussion, we can conclude that impurity injection into the divertor plasma is effective on the reduction of heat flux. Impurity seeding into the divertor plasma significantly reduces both the electron and ion energy. A comparison among the three radiator gasses shows that Xe seeding is the most effective on the reduction of electron and ion energy and generating the detached plasma.

The transition of detached to attached state has also been investigated by applying an ECH heating pulse at the east plug/barrier-cell. The ECH heating effects at the east plug/barrier-cell significantly increase the hot electron flow toward the central-cell and consequently towards the end-cell which

breaks the plasma detachment state in the D-module. It is observed that a short pulse of ECH significantly changes the plasma behavior in the D-module. The heat and ion fluxes enhance significantly during ECH injection. Especially, the ion flux increases remarkably during ECH injection period, which indicates the plasma detachment state has broken due to the ECH heating effect. For the ECH injection period, it is also observed that the ion flux increases with the increasing Xe plenum pressure. These results indicate the transition of an attached plasma from a detached state by applying ECH heating pulse.

6.2 Numerical simulation summary

The multi-fluid code “LINDA” has been developed and applied at the end-cell of GAMMA 10/PDX for understanding the detailed physical mechanism of energy loss processes during the interactions of plasma and neutral. The atomic processes of impurity (Ne, Ar, Kr and Xe) and hydrogen have been included in the LINDA code. It is shown that H injection leads to a strong reduction in the ion temperature. For the strongest H injection, the ion temperature on the target plate reduces to about 5 eV. The electron density and the particle flux increase with the increasing H injection. Simultaneous injection of Ar and H has also been investigated in the study. It is shown that Ar seeding leads a remarkable reduction in the electron temperature, which indicates radiation cooling effects of Ar. During the simultaneous injection of Ar and H, a tendency of saturation in the electron density and particle flux has been observed at the higher neutral H injection. On the other hand, for only H injection, the electron density and the particle flux continue to increase with the H injection. It is observed that the electron temperature reduces remarkably with the increasing Ar density. However, a slight influence of Ar seeding on the ion temperature has been observed. The CX loss has been detected as a major energy loss for the hydrogen ion while the radiation cooling and ionization of neutral particles has been detected as a major energy loss processes for the electrons. It is also observed that the ion energy loss terms increase significantly during H injection. On the other hand, the electron energy loss processes increase for impurity injection. A comparison among the three radiator gasses has also been performed numerically by using the LINDA code. It is found that Xe seeding significantly reduces the electron temperature. The energy loss term for both the electron and ion enhances significantly during Xe injection. The radiative power loss is also much higher for Xe seeding than that of Ar and Kr injection.

Transport of hydrogen neutral particles toward the upstream region has also been studied in the end-cell of GAMMA 10/PDX by developing a kinetic neutral transport code. As a first step, a series of initial test calculations have been performed by injecting hydrogen gas puffing molecules from the target plate with fixed plasma background. The hydrogen neutral particles are introduced into the background plasma with cosine distribution. In the present study, recycling hydrogen neutrals are considered as hydrogen atoms. On the other hand, gas puffing neutrals are considered as hydrogen molecules. It has been shown that neutral particles concentrate near the target plate and reduce toward

the upstream region. The hydrogen molecules are dissociated into atoms. As a result, the hydrogen atoms density is increased with the increasing gas puffing molecules. The hydrogen atoms also concentrate near the target plate and reduce toward the upstream region.

6.3 Concluding remarks

In the study, the radiation cooling effects of Ar, Kr and Xe has been clarified in the D-module based on the calorimeter and Langmuir probe measurements. From the study, we can conclude that Xe can be used as a radiator gas for generating detached plasma in the future and current tokamak devices.

During plasma detachment state by Xe seeding, the effects of ECH heat on the detached plasma has been studied. It is found that a short pulse of ECH can break the plasma detachment state. It is observed that additional plasma heating can be a useful tool to study the transition phenomena.

From the numerical simulation study by using a multi-fluid code "LINDA", the effects of neutral species injection into the end-cell has been clarified. The numerical results and its analyses in this paper may help to understand the energy loss processes in the divertor physics in Fusion devices (Tokamak and Linear). The kinetic neutral code will be a robust basis in the future to study the effects of molecular dynamic (especially MAR) on the plasma detachment.

The above results indicate the importance of neutral particles injection into the divertor region. The obtained knowledge from the study may contribute to understand the physical mechanism of plasma detachment operation in the divertor region by impurity seeding.

6.4 Future research tasks

The divertor simulation research is a very much important research topic to explore the physical mechanism of plasma detachment for sustainment of the future fusion devices such as ITER and DEMO. The divertor simulation research (E-divertor) has been effectively conducted in the west end-cell of GAMMA 10/PDX. Radiator gas injection into the divertor region significantly reduces the plasma energy by enhancing the radiation power loss and ionization loss. The energy loss processes (such as radiation loss, CX loss, ionization loss, etc.) in the D-module of GAMMA 10/PDX have not yet clarified. It is very much important to measure the power loss terms during impurity seeding. A bolometric measurement is necessary to measure the radiation power loss in the D-module. The effects of impurity injection on the ion temperature have not yet studied in the D-module. It is very much important to measure ion temperature during impurity injection. It is speculated that the ionization and recombination font depend on the neutral gas throughput and neutral species inside the D-module. The dependence of the ionization and recombination font on the neutral species and pressure need to be investigated in the future. In addition, the effects of the high heat flux on the plasma detachment state also need to be clarified in the future.

A numerical simulation study has been done in GAMMA 10/PDX by using the multi-fluid code LINDA. The atomic processes of hydrogen and impurities are included in the present model. The improvement of the LINDA code is also needed to explain the realistic behavior of the D-module. The physical model and the mesh structure of the LINDA code need to be improved in the future in order to explain the detailed physical mechanism of plasma detachment.

In the LINDA code, the neutral models for both the impurity and the hydrogen have been solved based on the 1D fluid equations. Fluid neutral model is computationally faster but less accurate in physics. Therefore, a kinetic neutral treatment is necessary to analyze the neutral profile precisely. In addition, the detailed hydrogen atomic and molecular processes need to be included in the kinetic neutral code to examine the hydrogen processes on the plasma detachment especially the molecular processes so-called MAR effects on the plasma detachment. It is also important to consider a V-shape target in the simulation space to examine the realistic behavior of the D-module plasma. It is also necessary to include the magnetic mirror confinement effects in the code. After completing the above tasks, the impurity transport towards the upstream region will also be necessary by coupling the LINDA code with the IMPGYRO code.

Finally, the 3D modeling may explain the more detailed physical mechanism of plasma detachment in the D-module. The hydrogen recycling processes may be enhanced if we consider the D-module chamber in the simulation space.

References

[1] K. Ooi, Bulletin of the Society of Sea Water Science, Japan, **51**, 285 (1997).

[2] H. Nobukawa, Bulletin of the Society of Sea Water Science, Japan, **51**, 289 (1997).

[3] Y. Miyata, et al., Research Report, **28**, Mar. (1996).

[4] Lawson, J. D, Atomic Energy Research Establishment, Harwell, Berkshire, U. K.

[5] L. Spitzer Phys. Fluids **1,** 253 (1958).

[6] C R Burnet et al., Phys. Fluids **1,** 438 (1958).

[7] J. Roth, et al., J. Nucl. Mater. **390-391,** 1 (2009).

[8] R.A. Pitts, et al., J. Nucl. Mater. **415,** S957 (2011).

[9] D. Naujoks et al., Nucl. Fusion **36,** 671 (1996).

[10] A. Loarte et al., Nucl. Fusion **47**, S203 (2007).

[11] K. Hoshino et al., Plasma Fusion Res. **12**, 1405023 (2017).

[12] ITER Physics Expert Group on Divertor et al., Nucl. Fusion **39**, 2391 (1999).

[13] S. I. Krasheninnikov et al., J. Plasma Phys. **83**, 155830501 (2017).

[14] P. C. Stangeby, Plasma Phys. Control. Fusion **43**, 223, (2000).

[15] S. I. Krasheninnikov et al., Phys. Plasmas **23**, 055602 (2016).

[16] K. Mukai et al., Nucl. Fusion **55**, 083016 (2015).

[17] F. Reimold et al., Nucl. Fusion **55**, 033004 (2015).

[18] R. Zagrski et al., Nucl. Fusion **56**, 016018 (2016).

[19] K. Gazka et al., Plasma Phys. Control. Fusion **59**, 045011 (2017).

[20] N. Asakura et al., Nucl. Fusion **49**, 115010 (2009).

[21] M.A. Mahdavi et al., J. Nucl. Mater. **220-222**, 13 (1995).

[22] N. Ohno, Plasma Phys. Control. Fusion **59**, 034007 (2017).

[23] S. I. Krasheninkov, Phys. Plasmas **4**, 1638 (1997).

[24] S. I. Krasheninkov, Phys. Scr. **T96**, 7 (2002).

[25] Yukap Hahn, Rep. Prog. Phys. **60**, 691 (1997).

[26] T W Morgan et al., Plasma Phys. Control. Fusion **60** 014025 (2018).

[27] G.De Temmerman et al., Fusion Eng. Des. **88**, 483 (2013).

[28] Y. Nakashima et al., Nucl. Fusion **57,** 113066 (2017).

[29] Y. Nakashima et al., Fusion Eng. Des. **85**, 956 (2010).

[30] Y. Nakashima et al., Fusion Sci. Technol. **63**, 100 (2013).

[31] Y. Nakashima et al., J. Nucl. Mater **438**, S738 (2013).

[32] Y. Nakashima et al., J, Nucl. Mater **463**, 537 (2015).

[33] Y. Nakashima et al., Fusion Sci. Technol. **68**, 28 (2015).

[34] M.S. Islam et al., Plasma Fusion Res. **11**, 2402042 (2016).

[35] B.J. Braams, "A Multi-Fluid Code for Simulation of the Edge Plasma in Tokamaks," vol. NET

Rep. 68, no. EURFU/XII-80/87/87/68, CEC, Brussels, (1987).
[36] S. V. Patankar, Numerical Heat Transfer and Fluid Flow, New York, Hemisphere, (1980).
[37] T. Furuta et al., Trans. Fusion Sci. Technol. **63**, 411 (2013).
[38] H. Takeda et al., Contrib. Plasma Phys. **56**, 784 (2016).
[39] M.S. Islam et al., Fusion Eng. Des. **125**, 216 (2017).
[40] M.S. Islam et al., Plasma Phys. Control. Fusion **59,** 125010 (2017).
[41] R. Schneider et al., Contrib. Plasma Phys. **46**, 3 (2006).
[42] T. D. Ronglien et al., J. Nucl. Mater. **196**, 347 (1992).
[43] H. Kawashima et al, Plasma Fusion Res. **1**, 031 (2006).
[44] R. Schneider et al., Contrib. Plasma Phys. **40**, 328 (2000).
[45] G. Kawamura et al., Contrib. Plasma Phys. **54**, 437 (2014).
[46] R. Zagorski et al., Nucl. Fusion **53**, 07030 (2013).
[47] M. Fichtmuller et al., Contrib. Plasma Phys. **38**, 284 (1998)
[48] D. Reiter et al., Fusion Sci. Technol., **47**, 172 (2005).
[49] D. B. Heifetz, J. Comp. Phys. **46**, 309 (1991).
[50] K. Shimizu et al., Nucl. Fusion **49**, 065028 (2009).
[51] D. E. Post., J. Nucl. Mater. **220**, 143 (1995).
[52] OPEN ADAS DATABASE (http://open.adas.ac.uk) and IAEA DATABASE (https://www-amdis.iaea.org/FLYCHK).
[53] R.K. Janev, Atomic and Molecular Processes in Fusion Edge Plasmas, Springer US (1995).
[54] K. B. Fournier, Nucl. Fusion **40**, 847 (2000).
[55] K. Nanbu, IEEE Trans. Plasma Sci**. 28**, 971 (2000).
[56] R. Behrisch et al., NATO ASI Series Ser. B Physics **131**, 413 (1986).
[57] M. Burnger et al., Interactions of Photons and Electrons with Molecules, Springer-Verlag, Berlin (2003).
[58] R. Rasser et al., Surf. Sci. **118**, 697 (1982).
[59] A. Loarte et al., Nucl. Fusion **38**, 331 (1998).
[60] H. Kubo et al., J. Nucl. Mater **313**, 1197 (2003).
[61] A. Kallenbeach et al., Plasma Phys. Control. Fusion **55**, 124041 (2013).
[62] Y. Hayashi et al, Phys. Plasmas **23**, 012511 (2016).
[63] Y. Hayashi et al, Nucl. Fusion **56**, 126006 (2016).
[64] K. Hoshino et al., Plasma Fusion Res. **9**, 3403070 (2014).
[65] X. Bonnin et al., Nucl. Mater. Energy **12**, 1100 (2017).
[66] M. Sakamoto et al., Nucl. Mater. Energy **12**, 1004 (2017).
[67] K. Miyamoto et al., J. Nucl. Mater. **313**, 1036 (2003).
[68] K. Miyamoto et al., J. Phys. Soc. Jpn. **76**, 034501 (2007).
[69] K. Miyamoto et al., J. Appl. Phys. **93**, 845 (2003).
[70] https://en.wikipedia.org/wiki/Nuclear_fusion.

[71] B.J. Braams, Contrib. Plasma Phys. **36**, 276 (1996).
[72] M. Inutake et al., J. Plasma Fusion Res. **78** (12), 1352 (2002).
[73] K. Yatsu et al.,Nucl. Fusion, **39**, 1707 (1999).
[74] Y. Nakashima et al., J. Nucl. Mater., **313-316**, 553 (2003).
[75] T. Tamano, Phys. Plasmas **2**, 2321 (1995).
[76] M. Ichimura et al., Fusion Eng. Design, **26**, 251 (1995).
[77] S. I. Braginskii, Rev. Plasma Phys. **1**, 205 (1965).
[78] K. Ichimura et al., Rev. Sci. Inst. **87** (11), 11D424 (2016).
[79] K. Ichimura et al., Plasma Fusion Res. **7**, 2405147 (2012).
[80] K. Kurihara et al., J. Phys. Soc. Jpn. **58,** 3453 (1989).
[81] M.S. Islam et al., AIP Conf. Proc. **1771**, 060015 (2016).
[82] G. Federici et al., Nucl. Fusion, **41**, 1967–2137 (2001).
[83] http://www.iter.org (2017).
[84] M. A. Heald et al., Plasma Diagnostics with Microwaves, John Wiley & Sons Inc., (1965).
[85] R. Katsumata et al., Jpn. J. App. Phys. **31,** 2249-2254 (1992).
[86] M. Yoshikawa et al., AIP Conference Proceedings **1771**, 050004 (2016).
[87] J. Kohagura et al., JINST **10**, C12024 (2015).
[88] M. Yoshikawa et al.,
[89] T. Yokodo et al., AIP Conference Proceedings **1771**, 040007 (2016).
[90] A. Loarte et al., Phys. Plasmas **18**, 056105 (2011).
[91] 星野一生,「トカマクにおける境界層プラズマ流の構造と重金属不純物輸送に関する研究」慶應義塾大学大学院 博士論文 (2008).
[92] M.S. Islam et al., “Numerical Simulation Study towards Plasma Detachment in the End-Cell of GAMMA 10/PDX by a Coupled Fluid-Neutral Code”, Contrib. Plasma Phys.
DOI: 10.1002/ctpp.201700122.
[93] G. Hass. Vacuum **51**, 39 (1998).

Acknowledgments

First of all, the author would like to express his sincere gratitude and thank Prof. Dr. Yousuke Nakashima at the University of Tsukuba for his supervision, continuous guidance, encouragement, kindness, and support during the research. His helpful advice, support, suggestions, guidelines, and deep discussions were very much helpful for the author to complete the present study. Without his guidelines and dedicated involvement in every step throughout the process, this paper would have never been accomplished. Those valuable lessons he taught the author during the Ph.D. program will be very much helpful for the author to conduct research in the future. Moreover, he has introduced various kinds of conferences, workshops, meetings, and seminars with me and encouraged me to join them and writing journal papers, which were valuable experiences in the Ph.D. program. It was a great experience to work with him. I am deeply grateful to him.

The author is deeply grateful to Prof. Dr. Akiyoshi Hatayama at Keio University for his helpful guidelines, advice, suggestions and encouragement to improve the numerical simulation code. He gave me a lot of valuable and helpful comments regarding the improvement of the numerical simulation code and writing journal papers.

The author also would like to show sincere gratitude and thank Prof. Dr. Mizuki Sakamoto, Assoc. Prof. Dr. Naomichi Ezumi, and Assoc. Prof. Dr. Masayuki Yoshikawa (at the University of Tsukuba) for giving me a lot of helpful comments and advice to improve the research. The author also thankful to Prof. Dr. Hiroto Matsuura at Osaka Prefecture University for his helpful comments and advice on the heat flux measurements.

The author wishes to thank the members of NBI group for their discussion, help, support, and encouragement.

The author is also grateful to Dr. Kazuya Ichimura (Kobe University), Dr. Hisato Takeda, Dr. Satoshi Togo (University of Tsukuba), Mr. Kunpei Nojiri (University of Tsukuba), Mr. Akihiro Terakado (University of Tsukuba), and Ms. Ryoko Tatsumi (Keio University).

The author gratefully acknowledges financial support from the Ministry of Education, Culture, Sports, Science and Technology (MEXT), Japan.

Finally, the author is deeply indebted to the members of GAMMA 10/PDX for their support and help during the experiments. It is my great pleasure to thank my spouse and parents who have helped and supported me a lot during the Ph.D. study.

This study was supported by the bidirectional collaboration research program (NIFS12KUGM066, NIFS14KUGM086).